OAK RIDGE
NATIONAL LABORATORY

MANAGED BY UT-BATTELLE
FOR THE DEPARTMENT OF ENERGY

Evaluation of HFIR LEU Fuel Using the COMSOL Multiphysics Platform

March 2009

Prepared by
Lee Tschaepe
Arthur E. Ruggles
James D. Freels
R. T. Primm, III

UT-BATTELLE
ORNL-27 (4-00)

Global Threat Reduction Initiative
Reduced Enrichment for Research and Test Reactors Program

EVALUATION OF HFIR LEU FUEL USING THE COMSOL MULTIPHYSICS PLATFORM

Lee Tschaepe[1]
Arthur E. Ruggles[1]
James D. Freels[2]
R. T. Primm, III[2]

Date Published. March 2009

Prepared by
OAK RIDGE NATIONAL LABORATORY
Oak Ridge, Tennessee 37831-6283
managed by
UT-BATTELLE, LLC
for the
U.S. DEPARTMENT OF ENERGY
under contract DE-AC05-00OR22725

[1] University of Tennessee, Knoxville
[2] ORNL Research Reactors Division

This page blank.

LIST OF FIGURES

LIST OF FIGURES

This page blank.

LIST OF TABLES

This page blank

NOMENCLATURE

A_{wet}	Wetted area of the cladding
A_{xs}	Coolant channel cross-sectional area
c_p	Specific heat
Cp	Heat capacity
C^+	Constant 5.5
$C_{\varepsilon 1}$	Constant 1.44
$C_{\varepsilon 2}$	Constant 1.92
C_μ	Constant 0.09
$\dot{E}_{generated}$	Rate of change of the energy generation within a control volume
$\dot{E}_{in}$	Rate of change of the flow of energy into the control volume
$\dot{E}_{out}$	Rate of change of the flow of energy out of the control volume
$\dot{E}_{stored}$	Rate of change of the energy stored within a control volume
$e^N(\mathbf{x})$	Error
F	Volume force vector
f_o	Magnitude of stress vector
HEU	High enriched Uranium
h	Convection heat transfer coefficient
I	Moment of Inertia
	Unit matrix
I_T	Turbulent intensity
k	Thermal conductivity
k_{TKE}	Turbulent kinetic energy
k_{fuel}	Thermal conductivity of the fuel
k_{fluid}	Thermal conductivity of the fluid
k_{clad}	Thermal conductivity of the clad
k_T	Turbulent conductivity
L_T	Turbulent length scale
L( )	Differential place holder
LEU	Low enriched uranium
Nu_{db}	Nusselt Number as computed by Dittus-Boelter
Nu_{st}	Nusselt Number as computed by Seider Tate
Nu_{mh}	Nusselt Number as computed by Modified Hausen
$Nu_{revised\_mh}$	Nusselt Number as computed by Revised Modified Hausen
{N}	Finite element basis function
n	Normal vector
Pr	Prandlt Number
P(u)	Turbulence production term
P1	Inlet pressure
P2	Outlet pressure
Pr_t	Turbulent Prandlt Number
p	Pressure
p_0	Initial prescribed boundary pressure
Q	Average core power
Q_α	Expansion Coefficient

NOMENCLATURE

$\{Q_e\}$	Nodal expansion coefficient matrix
q''	Heat flux
q'''	Volumetric heat generation
$\dot{q}$	Rate of energy generation
q_w	Wall heat transfer rate per unit area
q_0	Inward heat flux
q($\mathbf{x}$)	Unknown quantity
$q^N(\mathbf{x})$	Approximation to q($\mathbf{x}$)
$\Re^N$	Euclidean space
Re	Reynolds number
T	Temperature
T_{inf}	Ambient bulk temperature
Tf	Fluid Temperature
Ts	Solid temperature
T_s	Surface temperature of the cladding
Ts_0	Boundary temperature
T_w	Wall temperature
T2	Temperature in the solid
$T2_0$	Boundary temperature
T_∞	Coolant temperature
T*	Wall-conduction temperature
T^+	Normalized thermal wall dimension
$\bar{T}$	Average temperature
$\mathbf{t}$	Tangential vector to the boundary
u^+	Dimensionless wall velocity
u, v, w	Cartesian velocity components
$\mathbf{u}$	Velocity field
$\mathbf{u}_0$	Boundary velocity field
V	Volume of the fuel in the core
v*	Wall friction velocity
WS	Weak Statement
x, y, z	Cartesian coordinates
y^+	Normalized wall dimension
y	Distance from clad surface to the first boundary layer mesh node
∇	Gradient operator
∇T_{fuel}	Temperature gradient in the fuel
∇T_{fluid}	Temperature gradient in the coolant
∇Tf	Temperature gradient in fluid
∇T_s	Temperature gradient in solid
$\nabla T2$	Temperature gradient in solid
δ_w^+	Wall offset in viscous units
δ_{sub}	Viscous sublayer thickness
ε	Turbulent dissipation
η	Dynamic viscosity
η_T	Turbulent viscosity
κ	Karman's constant ~ 0.42

NOMENCLATURE

κ_{dv}	Dilatational viscosity
λ	Turbulent thermal conductivity
μ_{bulk}	Dynamic viscosity of the bulk fluid
μ_{wall}	Dynamic viscosity of the near wall fluid
μ_t	Turbulent viscosity
ν	Kinematic viscosity
ρ	Density
$\sum_i h_i N_{d,i}$	Concerns species diffusion
σ_ε	Constant 1.3
σ_κ	Constant 0.9
τ	Wall shear stress
τ_{wall}	Wall shear stress
ϕ	Dissipation function
Ψ_α	Trial space function
Ω	Domain of the differential equation
$\cup_e$	Non-overlapping sum of elements

This page blank.

ABSTRACT

A finite element computational approach to simulation of the HFIR core thermal-fluid behavior is developed. These models were developed to facilitate design of a low enriched core for the HFIR, which will have different axial and radial flux profiles from the current HEU core and thus will require fuel and poison load optimization. This report outlines a stepwise implementation of this modeling approach using the commercial finite element code, COMSOL, with initial assessment of fuel, poison and clad conduction modeling capability, followed by assessment of mating of the fuel conduction models to a one dimensional fluid model typical of legacy simulation techniques for the HFIR core. The model is then extended to fully couple 2-dimensional conduction in the fuel to a 2-dimensional thermo-fluid model of the coolant for a HFIR core cooling sub-channel with additional assessment of simulation outcomes. Finally, 3-dimensional simulations of a fuel plate and cooling channel are presented.

This page blank.

FOREWORD

The study documented here represents a first attempt at modeling the High Flux Isotope Reactor with the COMSOL software package. As such, at the beginning of the study, it was difficult to estimate the resources required to complete the effort and, in fact, the level of resources was underestimated. Hence this report should be regarded as a progress report that documents efforts accomplished to date. Future work is planned and will be based on studies reported here. Where appropriate, comments are included in this report as to the direction of future studies.

This page blank.

1.0 INTRODUCTION AND BACKGROUND

The HFIR is a beryllium-reflected, light water cooled, high enriched uranium (HEU) fueled research reactor. Figure 1 is a dimensioned cut away view of the current HFIR HEU core. This figure is taken from McLain, 1967. The height of the core shown in Fig. 1 is 0.6096 m. The fueled height is 0.508 m, with the fueled region centered along the core height. The core is composed of two elements. The outer diameter of the outer element is 0.42 m. The inner element contains 171 fuel plates. The outer element contains 369 fuel plates. Fuel plate thickness and spacing are each 1.27 mm. The current operating power of the reactor is 85 MW and the heat load attributable to the fuel plate is 80.7 MW. The remaining heat is deposited in the target, control cylinders, and reflectors.
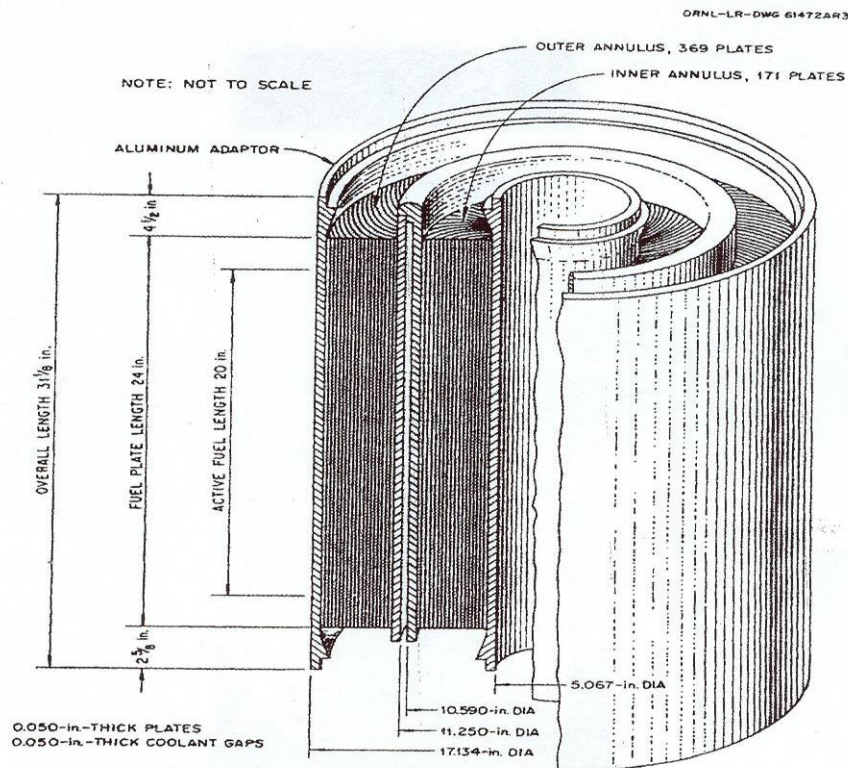
Fig. 1. HFIR core dimensions.

Figure 2 is an enhanced view of a radial slice of the current HFIR core. The cladding in the HFIR fuel plates remains predominately uniform through the fabrication process; while the poison-bearing region and the fuel are graded. The poison, B_4C, is only present in the inner element fuel plates. The fuel and poison grading is shown in Fig. 2. The fuel to poison ratio varies from near zero to greater than 0.9 based on the relative radial position within each fuel plate. The direction of the coolant flow in Fig. 2 is into the page. It is important to note that the thickness of the fuel plate and coolant channel is greatly enhanced in Fig. 2. The combined half-fuel plate and half-coolant channel thickness is 1.27 mm. This is roughly equivalent to 10 sheets of paper.

1
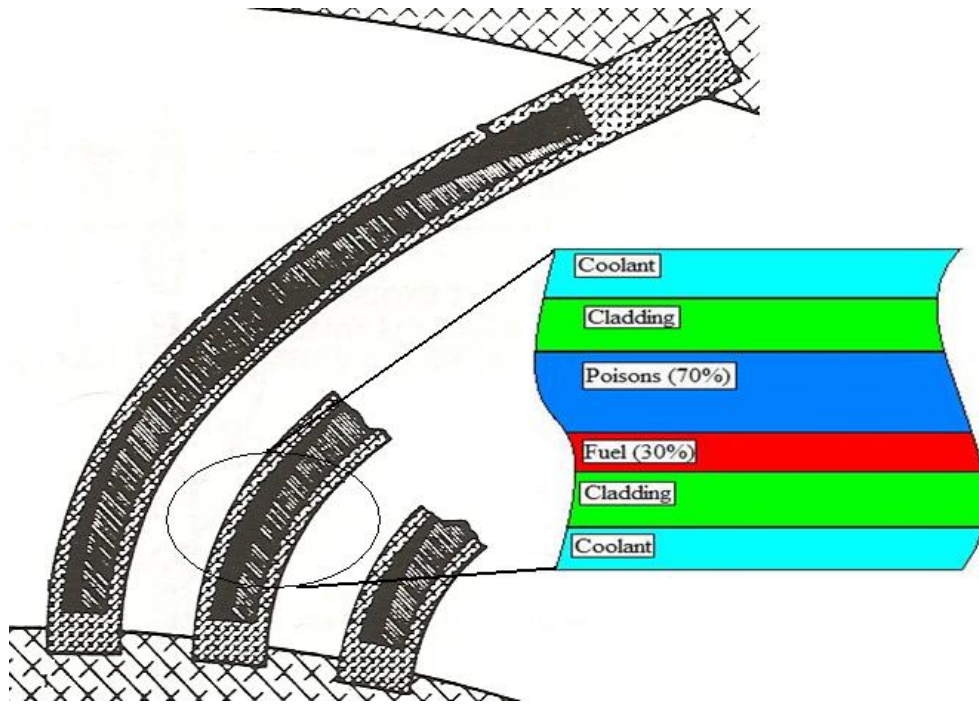
Fig. 2. Enlarged view of coolant channels, not to scale.

1.1 Current thermal hydraulic analysis methodology

The HFIR fuel performance evaluations are supported by three dimensional neutronics calculations, including simulation of the entire fuel life, that render, among other things, 3-dimensional topologies of the power developed in the fuel at any time during the fuel cycle. These core physics calculations take advantage of nuclear numerical simulation techniques that have been in continuous development since the HFIR was put in service in the 1960's.

The primary models for thermal performance of the fuel cooling system were developed by McLain, 1967, and subsequently updated by Cole et al, 1986. The updates involved conversion of the original code to VS-FORTRAN, and addition of D_2O properties. Some geometric parameters prescribed in the body of the original code were also moved to input locations. The basic analysis method from McLain otherwise remained unchanged. The modeling for the core cooling is of the classical sub-channel type, with a fluid element moving from core inlet to core outlet along a straight axial path. Nominal thermal flux to the fluid element is determined by fuel volumetric power generation from the neutronics calculations. One dimensional conduction through the plate thickness is modeled. No axial or spanwise conduction modeling is performed in the fuel plate. Consideration of uncertainties in channel dimensions and thermal flux that are specific to the HFIR core, including potential hot spot, cladding non-bond, and hot stripe conditions that may exist due to manufacturing imperfections are modeled using scalar multipliers derived from other analyses.

Prior evaluation of lateral turbulent coolant mixing between a sub-channel with a hot stripe and an adjacent sub-channel without a hot stripe indicated that the bulk coolant temperature is significantly over-predicted along the hot stripe path when the classical (McLain) sub-channel analysis techniques are employed (Ruggles, 1997). This lateral movement of thermal energy between sub-channels is not simulated in the current HFIR core thermal model but, when

modeled, would increase the margin to incipience of boiling. Addition of models representing lateral turbulent coolant mixing will improve the simulation fidelity of the HFIR core thermal performance.

Thermal boundary layer development over local flux perturbations such as hot spots leads to locally higher temperature gradients near the wall, and attendant higher heat transfer coefficient. These effects are also not modeled in the current McLain simulations.

1.2 Justification for a new methodology

The Global Threat Reduction Initiative (GTRI), Reduced Enrichment for Research and Test Reactors (RERTR) program, administered by the National Nuclear Security Administration (NNSA) of the United States Department of Energy (DOE), has as one of its goals to convert all United States research reactors from HEU fuel to low enriched uranium (LEU) fuel. This fuel will be a uranium/molybdenum alloy having substantially different thermal properties from the current HEU fuel; that fuel being a uranium oxide/aluminum mixture. Furthermore, to prevent degradation of reactor performance (i.e., flux at experimental positions), an LEU fuelled HFIR will operate at a higher power density than the current configuration. Neutronics calculations indicate that the power in an LEU core will have a different spatial distribution than that found in the current HEU core. For these reasons, qualifying an LEU fuel in HFIR requires revision of the thermal hydraulic analyses that form the bases for the safety analyses that are documented in the HFIR Safety Analysis Report. This work is an initial step towards development of a state-of-the-art thermal hydraulics and structural analyses capability.

Research Reactors Division, ORNL, has adopted the finite element, multiphysics, numerical analysis program, COMSOL, for modeling thermal and fluid flow behavior for the development of a new fuel for HFIR based on low enriched uranium (LEU). Based on RRD staff experience with designing a cold source for HFIR (vessel containing supercritical hydrogen), COMSOL is well suited to multi-physics evaluations and provides several solution options to accommodate large problems with dense meshs as in this application.

Modern computational fluid dynamic (CFD) simulation, in conjunction with conduction modeling in the fuel and cladding, allows direct utilization of the spatial power distribution in the fuel volume as predicted from the core nuclear physics models. It also allows detailed simulation of the impact of fuel manufacturing flaws, fuel cooling channel dimensional variations, and fuel loading uncertainties such that best estimate evaluations of these permutations can be available. This project includes development of geometric and material models for the fuel structure and the coolant in a computational format allowing coupled solution of the governing thermal-fluid multi-physics equations describing the movement of the nuclear energy from the fuel into the coolant.[††]

[††] In the titles to some of the figures in this report can be found parenthetical expressions, for example (2D_uniform_conduction.mph). These expressions are the names of the COMSOL datasets that were executed to produce the data depicted in the figures. These datasets have been retained by Research Reactors Division, ORNL, in the quality assurance records for the division and are identified as a group by the ORNL TM number assigned to this report.

2.0   BASES FOR ANALYSES USING COMSOL

Beginning with the High Flux Isotope Reactor System RELAP5 Input Model, by Morris and Wendel, an energy balance and the integral Reynolds Transport Theorem is investigated, on a sub-channel basis, so that an analytic comparison to COMSOL can be made for the temperature rise and pressure drop across a heated channel. In addition this analysis will also demonstrate the internal energy change in the sub-channel. The sub-channel of interest is displayed in Figure 3. The values used in the following analytic analysis are displayed in Table 1.

Table 1: Values of physical constants

Physical Constant	Value	Source
c_p	4180.76 J/(kg*K)	Incropera and Dewitt pg. 924
Q	80.7 MW	Morris and Wendel pg. 15
$\bar{\rho}$	982.91 kg/m^3	Incropera and Dewitt pg. 924
ρ_{out}	976.56 kg/m^3	Incropera and Dewitt pg. 924
ρ_{in}	988.37 kg/m^3	Incropera and Dewitt pg. 924
v_{in}	15.8 m/s	Morris and Wendel pg. 13
v_{out}	15.99 m/s	
$\bar{v}$	15.895 m/s	
g	9.81 m/s^2	
h	0.00127 m	Morris and Wendel pg. 5
L	.6096 m	Morris and Wendel pg. 5
D_H	.0025 m	
f	.02	
q''	2025602 W/m^2	
T_{in}	321.9 K	Morris and Wendel pg. 6
T_{out}	345 K	
$\dot{m}$	836.35 kg/s	
vA	0.8462 m^3/s	Morris and Wendel pg. 13
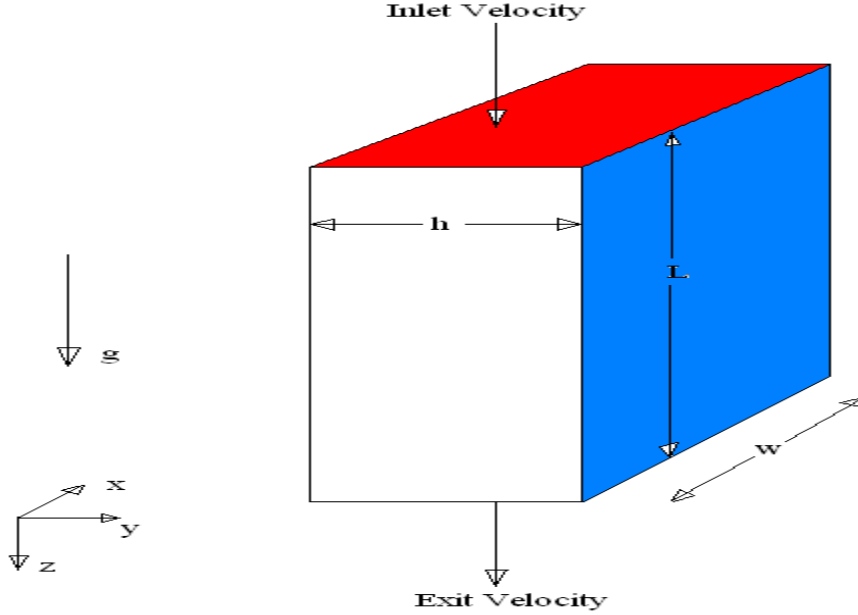
Fig. 3. Coolant channel control volume

Initially, a simple energy balance on a heated channel is used to determine the exit temperature,

$$Q = \dot{m} c_p (T_{out} - T_{in})$$

Eq. 1

where Q is the nominal core power, $\dot{m}$ is the nominal mass flow rate through the fuel region, c_p is the specific heat for water evaluated at the coolant inlet temperature, T_{out} is the coolant exit temperature, and T_{in} is the coolant inlet temperature. The coolant exit temperature is determined to be 345 K. The coolant exit temperature as reported by Morris and Wendel is 69.4 ˚C (342.4 K). The computed coolant exit temperature is used to determine material properties at the exit, and channel average properties.

Applying the conservation of mass to the control volume displayed in Figure 3, the exit velocity can be determined via Equation 2.

$$\rho_{in} v_{in} A_{xs} = \rho_{out} v_{out} A_{xs}$$

Eq. 2

where ρ is the density of the coolant at the inlet and exit of the coolant channel, v is the velocity at the inlet and exit, and A_{xs} is the flow cross-sectional area. The exit velocity is 15.99 m/s.

Next, the Reynolds Transport momentum and energy equations are used to determine the pressure drop across the heated sub-channel and the internal energy loss across the heated sub-channel. The general integral Reynolds Transport theorem is:

$$\iiint\limits_V \frac{\partial}{\partial t}(\rho c)dV + \oiint\limits_S (\rho c)\vec{v}\cdot\vec{n}dS = \iiint\limits_V \rho\phi dV + \oiint\limits_S \vec{J}\cdot\vec{n}dS \qquad \text{Eq. 2}$$

where c is the specific value of an extensive property per unit mass, ϕ is the rate of introduction of c per unit mass within the control volume, and $\vec{J}\cdot\vec{n}$ is the rate of loss of c per unit area due to surface effects (Todreas and Kazimi pg 94).

In the Reynolds Transport momentum equation c is equal to $\vec{v}$ (mass velocity at the boundary), $\vec{J}$ is equal to $\overline{\overline{\tau}} - p\overline{\overline{I}}$ (stress tensor minus pressure times a unity tensor), and ϕ is equal to $\vec{g}$ (gravitational acceleration). It is assumed that this is a steady state analysis. Therefore the first term in Equation 2 is zero.

Applying the appropriate bounds, based on Figure 3, the momentum equation is expanded to Equation 3.

$$\int_0^h \rho_{in}v_{in}v_{in}\cdot\hat{n}wdA + \int_0^h \rho_{out}v_{out}v_{out}\cdot\hat{n}wdA$$
$$= \int_0^L \overline{\rho}gwhdV + \int_0^L \overline{\overline{\tau}}\cdot\hat{n}wdA + \int_0^h -p_{in}\overline{\overline{I}}\cdot\hat{n}wdA + \int_0^h -p_{out}\overline{\overline{I}}\cdot\hat{n}wdA \qquad \text{Eq. 3}$$

Upon integration of Equation 3 the pressure drop across the core can be determined. The integrated form, with the pressure term isolated, is given in Equation 4.

$$\rho_{out}v_{out}^2 wh - \rho_{in}v_{in}^2 wh - \overline{\rho}gwhL + \overline{\overline{\tau}}wL = \Delta pwh \qquad \text{Eq. 4}$$

The $\overline{\overline{\tau}}wL$ term is represented as the pressure change due to friction in Equation 5.

$$\overline{\overline{\tau}}wL = 1/2\,\overline{\rho}v^2 f\left(L/D_H\right)wh \qquad \text{Eq. 5}$$

Substituting Equation 5 into Equation 4 and simplifying yields the pressure change across the core. The resulting equation is:

$$\Delta p = \rho_{out}v_{out}^2 - \rho_{in}v_{in}^2 - \overline{\rho}gL + 1/2\,\overline{\rho}v^2 f\left(L/D_H\right) \qquad \text{Eq. 6}$$

In order to obtain the total pressure change across the core, the inlet and exit form losses need to be taken into account. Equation 7 yields the total pressure change due to form losses.

$$\Delta p_{form\_losses} = C_{f_{in}}\rho_{out}v_{out}^2 + C_{f_{out}}\rho_{in}v_{in}^2 \qquad \text{Eq. 7}$$

where $C_{f_{in}}$ is 0.1 and $C_{f_{out}}$ is 0.75. Therefore the total pressure change across the core is the sum of Equation 6 and Equation 7. The resulting pressure change across the core is 708577.46 Pa (102.8 psi). The pressure drop through the core as reported by Morris and Wendel is approximately 105 psi (723949 Pa). The Reynolds Transport evaluation illustrates that the potential energy change in the core is minimal. The potential energy change across the core is less than 1 percent of the total pressure drop across the core.

In the Reynolds Transport energy equation c is equal to $u + v^2/2$, $\vec{J}$ is equal to $-\vec{q}'' + \left(\overline{\overline{\tau}} - p\overline{\overline{I}}\right) \cdot \vec{v}$, and ϕ is equal to $q'''/\rho + \vec{g} \cdot \vec{v}$. It is assumed that this is a steady state analysis and that there is no volumetric heating, q''', in the coolant. With these terms and the appropriate bounds, the Reynolds Transport energy equation is:

$$\int_0^h \rho_{in} c_{in} v_{in} \cdot \hat{n} w dA + \int_0^h \rho_{out} c_{out} v_{out} \cdot \hat{n} w dA =$$
$$\int_0^L \overline{\rho} g \overline{v} wh dV - \int_0^L q'' \cdot \hat{n} w dA + \int_0^L \overline{\overline{\tau}} \overline{v} \cdot \hat{n} w dA + \int_0^h - p_{in} \overline{\overline{I}} \overline{v} \cdot \hat{n} w dA + \int_0^h - p_{out} \overline{\overline{I}} \overline{v} \cdot \hat{n} w dA$$

Eq. 8

Integration of Equation 8, with the appropriate bounds, yields:

$$\rho_{out} v_{out} whc_{out} - \rho_{in} v_{in} whc_{in} = \overline{\rho} g \overline{v} whL + q'' wL - \overline{\overline{\tau}} wL\overline{v} + \Delta \overline{p} \overline{v} wh$$

Eq. 9

where

$$\rho_{out} v_{out} wh = \rho_{in} v_{in} wh = \dot{m}$$

Eq. 10

Upon substituting Equation 10 into Equation 9

$$\dot{m} \Delta c = \overline{\rho} g \overline{v} whL + q'' wL - \overline{\overline{\tau}} wL\overline{v} + \Delta \overline{p} \overline{v} wh$$

Eq. 11

As a consequence of Equation 10, Equation 11 becomes:

$$\Delta c = \frac{\left(\overline{\rho} g \overline{v} whL + q'' wL - \overline{\overline{\tau}} wL\overline{v} + \Delta \overline{p} \overline{v} wh\right)}{\rho_{in} v_{in} wh}$$

Eq. 12

Equation 5 is substituted into Equation 12 to yield.

$$\Delta c = \frac{\left(\overline{\rho} g \overline{v} whL + q'' wL - 1/2 \overline{\rho} \overline{v}^3 f(L/D_H) wh + \Delta \overline{p} \overline{v} wh\right)}{\rho_{in} v_{in} wh}$$

Eq. 13

The internal energy change within the coolant channel is given by Equation 14

$$\Delta u = \frac{\left(\overline{\rho} g \overline{v} L + q'' L/h - 1/2 \overline{\rho} \overline{v}^3 f(L/D_H) + \Delta \overline{p} \overline{v}\right)}{\rho_{in} v_{in}} + \left(\frac{v_{in}^2}{2} - \frac{v_{out}^2}{2}\right)$$

Eq. 14

where h is the gap-wise dimension of the coolant channel, 0.00127 m. The computed internal energy change within the coolant channel is 62369.23 m^2/s^2. The McLain code only includes energy terms due to wall to fluid heat transfer, consistent with Equation 1. The difference

between McLain outcomes and COMSOL outcomes for identical conditions should be represented by,

$$\Delta u' = \frac{\left(\overline{\rho g \bar{v}} L - 1/2 \, \overline{\rho \bar{v}}^3 f\left(L/D_H\right) + \Delta p \bar{v}\right)}{\rho_{in} v_{in}} + \left(\frac{v_{in}^2}{2} - \frac{v_{out}^2}{2}\right)$$
Eq. 15

The major source term for the $\Delta u'$ in Equation 15 is due to the pump energy dissipated in the core. The pumping power is the product of the volumetric flow rate and the pressure drop across the core. The volumetric flow rate is 0.84622 m^3/s and the pressure drop across the core is 708577.46 Pa. This yields a pump power of 599612 W. This is equivalent to 0.743 percent of the total core power dissipation. McLain code does not include pump energy in its evaluation. However, COMSOL incorporates pump energy into its calculations. As a result COMSOL should over predict the core temperature difference predicted by the McLain code, ΔT_{core_McLain} by 0.743 percent.

Figure 4 shows the COMSOL modeling domain relative to two fuel plates and one cooling channel. The physics governing the modeling of the coolant channel are described by the conservation of mass, the Navier-Stokes equations, and conservation of energy. The conservation of mass is shown in Equation 16.

$$\nabla \bullet \mathbf{u} = 0$$
Eq. 16

where, $\mathbf{u}$ is the velocity vector describing the coolant flow and u, v, and w are the velocities in the x, y, and z directions, respectively. In a rectilinear coordinate system this equation is equivalent to Equation 17.

$$\frac{\partial u}{\partial x} + \frac{\partial v}{\partial y} + \frac{\partial w}{\partial z} = 0$$
Eq. 17

The basic equation that describes the coolant flow is the incompressible Navier-Stokes equation, neglecting body forces,

$$\rho\left(\frac{\partial \mathbf{u}}{\partial t} + \mathbf{u} \bullet \nabla \mathbf{u}\right) = -\nabla p + \rho \upsilon \nabla^2 \mathbf{u}$$
Eq. 18

where, the left side of the equation is the terms relating to inertia, the right side of the equation describes the pressure gradient, and viscosity. This equation is expanded for 2-D rectilinear coordinates in Equations 19, and 20.

$$\frac{\partial u}{\partial t} + u\frac{\partial u}{\partial x} + v\frac{\partial u}{dy} + w\frac{\partial u}{\partial z} = -\frac{1}{\rho}\frac{\partial p}{\partial x} + \upsilon\left(\frac{\partial^2 u}{\partial x^2} + \frac{\partial^2 u}{\partial y^2} + \frac{\partial^2 u}{\partial z^2}\right)$$
Eq. 19

$$\frac{\partial v}{\partial t} + u\frac{\partial v}{\partial x} + v\frac{\partial v}{dy} + w\frac{\partial v}{\partial z} = -\frac{1}{\rho}\frac{\partial p}{\partial y} + \upsilon\left(\frac{\partial^2 v}{\partial x^2} + \frac{\partial^2 v}{\partial y^2} + \frac{\partial^2 v}{\partial z^2}\right)$$
Eq. 20

Once fully developed flow is established, Equations 19 and 20 are reduced to a single steady one dimensional Navier Stokes equation.

In simulations presented here, COMSOL employs a form of law of the wall to evaluate the temperature profiles and velocity profiles in the near wall regions. Figure 5 is an enhanced representation of the law of the wall approximation in the near wall region.

One scale parameter for mesh selection near the wall is the normalized wall dimension, y^+, defined as,

$$y^+ = \frac{y\sqrt{\tau/\rho}}{\upsilon}$$

Eq. 95

where τ is the wall shear stress, ρ is the fluid bulk density, y is the dimension normal to the cladding surface, extending into the coolant, in meters, and ν is the kinematic viscosity of the fluid. At $y^+ \leq 5$ the velocity profile is linear.

In the near wall region the boundary layer is dominated by viscous shear. This thin region near the wall is referred to as the viscous sublayer. The thickness of the viscous sublayer is determined via Equation 21.

$$\delta_{sub} = \frac{5\upsilon}{v^*}$$

Eq. 21

where v* is the wall friction velocity, and ν is the dynamic viscosity of the fluid.
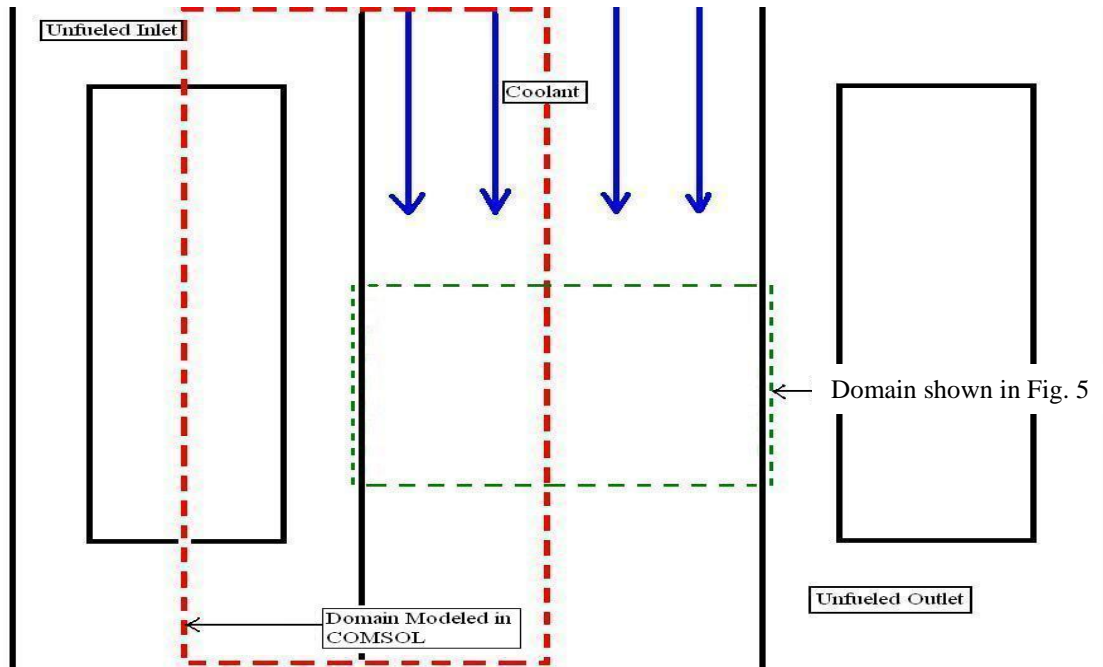
Fig. 4. Control volume of interest.
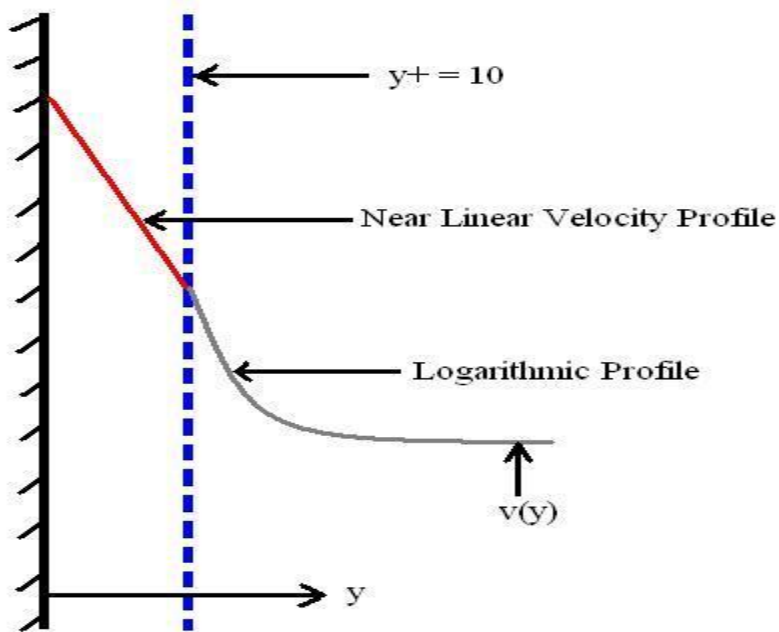
Fig. 5. COMSOL sub-channel model cross sectional view.
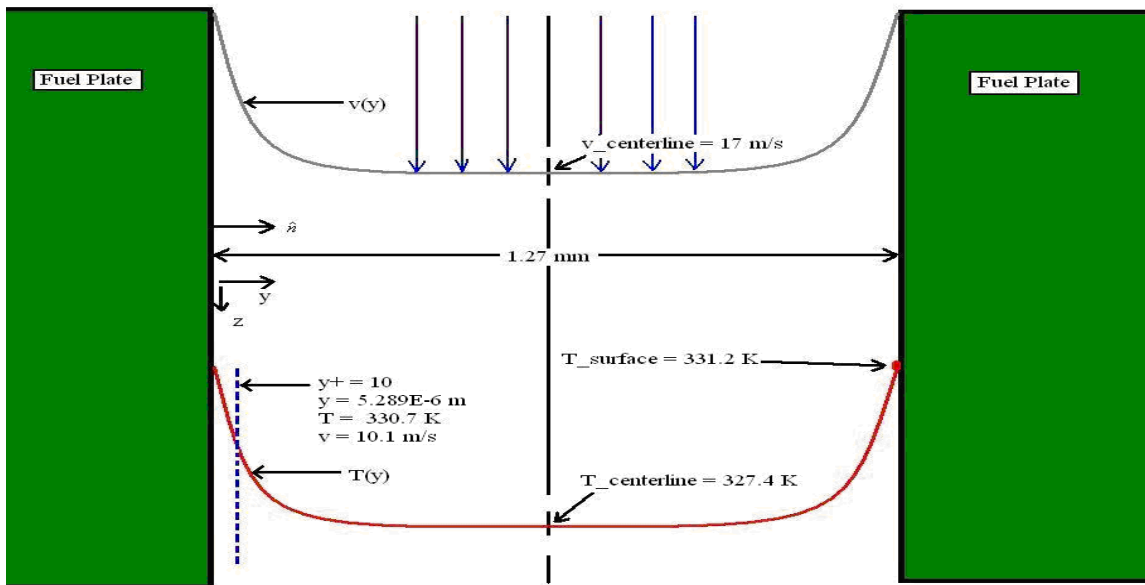
Fig. 6. Sub-channel physics.

The wall friction velocity, v* is determined as,

$$v^* = \left(\frac{\tau_w}{\rho} \right)^{0.5}$$

Eq. 22

10

where τ_w is the wall shear stress and ρ is the coolant density. Extending in the normal direction from $5 \le y^+ \le 30$ is a region termed the buffer layer (White 419). In this region, the velocity profile transitions smoothly between the linear profile found in the viscous sublayer to the logarithmic layer as shown in Fig. 5. (Spalding 1961) was able to deduce an equation that accurately described the near wall region for y^+ values from the surface of the wall to greater than 100. This composite formula is given by Equation 23.

$$y^+ = u^+ + e^{-\kappa B}\left[e^{\kappa u^+} - 1 - \kappa u^+ - \frac{\left(\kappa u^+\right)^2}{2} - \frac{\left(\kappa u^+\right)^3}{6} \right]$$

Eq. 23

The temperature law of the wall, as proposed by Kármán (1939) is given by Equation 24.

$$T^+ = \frac{T_w - \overline{T}}{T*} = \int_0^{y^+} \frac{dy^+}{1/\mathrm{Pr} + \mu_t / \mathrm{Pr}_t}$$

Eq. 24

where T* is the wall-conduction temperature. The wall-conduction temperature is given by Equation 25.

$$T* = \frac{q''_w}{\left(\rho c_p v*\right)}$$

Eq. 25

Very near the wall, the thermal sublayer has the form $T^+ = Pr*y^+$ where Pr is the Prandtl number. Further away from the wall, a logarithmic layer is obtained:

$$T^+ \approx \frac{\mathrm{Pr}_t}{\kappa} \ln\left(y^+\right) + A(\mathrm{Pr})$$

Eq. 26

The intercept A(Pr) varies strongly with Pr (White 487-488).

Figure 5 shows details of the velocity and temperature profile in the coolant channel for nominal conditions. COMSOL models the near wall region, where y^+ is less than 10, using a form of the law of the wall. The fluid velocity and temperature varies from zero to 10.1 m/s and from 331.2 K to 330.7 K in the near wall region, where the functional approximation is employed. These variations are for nominal conditions. In limiting cases the wall temperature ascends to near saturation, $T_{sat} = 523$ K. The functional representations for the temperature and velocity profile do not accommodate the significant thermo physical property variations that occur for these limiting cases. Also, the material data for water in the COMSOL libraries uses around 10 data points for temperature values between 273 K and 373 K. All values in-between these data points are determined by a piecewise cubic fit and all extrapolated values are assumed to be a constant equal to the largest value. In limiting cases values in the near wall region are outside the range currently represented. Nominal core conditions are considered in this report, so the current thermo physical property representations are adequate in COMSOL.

The conservation of energy equation describes the flow of energy through a control volume by Equation 27.

$$\dot{E}_{in} - \dot{E}_{out} + \dot{E}_{generated} = \dot{E}_{stored}$$

Eq. 27

where, $\dot{E}_{in}$ is the rate of energy transfer into the control volume, $\dot{E}_{out}$ is the rate of energy transfer out of the control volume, $\dot{E}_{generated}$ is the rate of change of energy generated within the control volume, and $\dot{E}_{stored}$ is the rate of change of stored energy within the control volume. This equation is expanded for rectilinear coordinates, neglecting the z-direction, as follows,

$$\frac{\partial}{\partial x}\left(k\frac{\partial T}{\partial x}\right)+\frac{\partial}{\partial y}\left(k\frac{\partial T}{\partial y}\right)+\dot{q}+\frac{Dp}{Dt}+\varphi=\rho\frac{Dh}{Dt}$$

Eq. 28

where $\dfrac{Dh}{Dt}$ is the material derivative and ϕ is the dissipation function.

The energy transfer within the fuel plate is by conduction. The governing equation for heat transfer by conduction is,

$$-k_{fuel}\nabla T_{fuel}=q''$$

Eq. 29

where, k is the thermal conductivity, q'' is the heat flux, and ∇T_{fuel} is the temperature gradient of the fuel. The rate of heat transfer between the fuel plate and the coolant can be found by correlating convection and conduction equations, where the convection equation is described by,

$$q''_{w}=h(T_{s}-T_{\infty})=-k_{fluid}\nabla T_{fluid}=-k_{fuel}\nabla T_{fuel}$$

Eq. 30

where, h is the convection heat transfer coefficient, T_{s} is the surface temperature of the cladding, and T_{∞} is the coolant temperature.

The COMSOL simulations simultaneously model the fluid mechanics and the energy transfer from the fuel into the coolant.

2.1 Mathematical basis for finite element solution

COMSOL is a commercial finite element based equation solver built on the MATLAB programming language. MATLAB is built on the C programming language. Thus, COMSOL is a rather high level programming environment, driven through a graphical user interface that is also accessible through MATLAB and internal scripting language and a batch-mode environment.. COMSOL uses partial differential equations (PDE) to describe physical systems, q(**x**).

$$q=q(\mathbf{x})$$

Eq. 31

$$L(q)=0 \text{ on } \Omega\subset\mathfrak{R}^{N}$$

Eq. 32

where L() is the notation for a set of PDE's, Ω is the domain in which the desired system is contained, and $\mathfrak{R}^{N}$ is Euclidean space.

The complexity of q(**x**) tends to prevent direct solutions from being made. As a result an approximation $q^{N}(\mathbf{x})$ is made. This approximation can be equated to the summation of a set of trial space functions $\Psi_{\alpha}(\mathbf{x})$ and corresponding expansion coefficients Q_{α}.

$$q(\mathbf{x}) \approx q^N(\mathbf{x}) = \sum_{\alpha=1}^{N} \Psi_\alpha(\mathbf{x}) Q_\alpha \qquad \text{Eq. 33}$$

This approach produces an inherent error. The error stems from differences between the approximation $q^N(\mathbf{x})$ and q(x).

$$e^N(\mathbf{x}) = q(\mathbf{x}) - q^N(\mathbf{x}) \qquad \text{Eq. 34}$$

This error, $e^N(\mathbf{x})$, is minimized via weak statement formulation. The weak statement (WS) requires that the error of the approximation is perpendicular to a set of functions ϕ_β.

$$WS^N \equiv \int_\Omega \phi_\beta L(q^N) d\tau \equiv 0 \qquad \text{Eq. 35}$$

Implementation of the WS over large irregular domains is difficult. By discretizing the domain Ω of interest into a sum of non-overlapping domains a solution can be found.

$$\Omega \approx \Omega^h = \cup_e \Omega_e \qquad \text{Eq. 36}$$

This allows the approximation to q(x) to be replaced by a sum of discretized approximations.

$$q(\mathbf{x}) \approx q^N(\mathbf{x}) \equiv q^h(\mathbf{x}) = \cup_e q_e(\mathbf{x}) \qquad \text{Eq. 37}$$

Next, the column matrix $\{N(\mathbf{x})\}$ is used to represent the descritized equivalent of $\Psi_\alpha(\mathbf{x})$. This now allows the function approximation to be written on a descritized basis.

$$q^N \equiv q^h = \cup_e \{N(\mathbf{x})\}^T \{Q\}_e \qquad \text{Eq. 38}$$

where $\{Q\}_e$ are the expansion coefficients evaluated at the mesh nodes. This can be substituted into the WS and rewritten as the following linear algebraic expression.

$$[Matix]\{Q\} = \{b\} \qquad \text{Eq. 39}$$

Expressions of this form can be solved by programs such as MATLAB (Baker 2006). As a result of the discretization of the domain Ω the accuracy of the solution is dependent on the level of detail in the mesh. As a result, regions where steep gradients are expected should contain a dense mesh to facilitate resolution in those regions.

2.2 Considerations in the construction of the finite element mesh

In the case of simulation of the coolant flow in HFIR, steep velocity and temperature gradients are expected in the fluid near the wall. If a basic thermal analysis is performed, the magnitude of these gradients can be vividly depicted via a generalized heat conduction analysis of the coolant channel. The basic heat conduction equation qualifies the temperature change per unit length as a function of the flux and thermal conductivity of the material. For the temperature range of interest, the thermal conductivity of water ranges between 0.6-0.7 W/(m*K). Assuming

the thermal conductivity of water is approximately 0.7 W/(m*K), then the scale of the temperature gradient near the fuel plate can be estimated. The surface heat flux of the fuel plate is near $1.0(10^6)$ W/m^2 which indicates a temperature gradient in the water coolant of $1.3(10^6)$ K/m. The temperature in the coolant changes at a rate of approximately 1 degree Kelvin per micron [$1(10^6)$ K/m] where the coolant meets the fuel cladding. In the worst case scenario T_{wall} is nearly equal to T_{sat} (core limiting case for the incipience of boiling). If this occurs the local heat flux would be approximately $16(10^6)$ W/m^2 and the temperature in the coolant would change at a rate of approximately 1.6 degree Kelvin per tenth of a micron [$1.6(10^7)$ K/m] where the coolant meets the fuel cladding. This analysis highlights the necessity for extremely high mesh resolution at the coolant channel/cladding interface for the HFIR fuel simulation. In the case of conduction simulations of non-bonds and fuel segregation defects, locally steep temperature gradients are again expected, and a mesh of smaller pieces must be used in those regions.

The breaking of the continuum into pieces, or into a mesh with mesh intersection points represented locally by scalar property values allows rendering of the governing differential equation system into a linear algebra equation system suited to solution using the digital computer. The size of the matrices being handled during solution is proportional to the number of pieces into which the continuum was partitioned. This can lead to large memory requirements. The initial configuration for the computer hardware for these simulations started with four processors and 32 GB RAM, and was upgraded during the course of these studies to eight processors and 64 GB RAM. Even with the upgrade, resource limitations exist for 3-dimensional simulations, and these are discussed in more detail when those simulation outcomes are presented.

The graphical user interface for COMSOL is elaborate, with many equation sets available to implement in each solution domain. Several types of boundary conditions, solver options and meshing options are also available. With so many degrees of freedom, all of which may influence the simulation outcome, a file management protocol was implemented to assure proper archiving and repeatability of simulations. Each simulation outcome in this report is referenced to an input file name.

Most graphs of COMSOL simulations presented subsequently have had the scale in the x-direction greatly magnified to aid visualization. However, this scaling of the axis causes some rendering issues in select cases and these are enumerated as they occur. The reason for changing the axis scaling is to make visualization of subject matter easier. This is especially helpful when there are two or more orders of magnitude difference between the scale of x and y axis, which is the case for these simulations.

3.0 TWO DIMENSIONAL FUEL MODEL WITH INSULATED BOUNDARIES

Initial 2-dimensional models homogenized the poison and fuel regions within the fuel plate (these termed non-stratified models), which is consistent with HFIR core physics approaches. Figure 7 shows the investigated volume of a HFIR homogenized fuel plate and coolant sub-channel and its correlation to the COMSOL models. The ratio of fuel to poison, shown in the right side of Fig. 7, corresponds to a region near the spanwise center of a fuel plate. It can be seen in the left side of Fig. 7 that the fuel plates are involutes. However, the 2 dimensional simulations use a flat fuel plate model consistent with the earlier approach used by McLain in 1967.
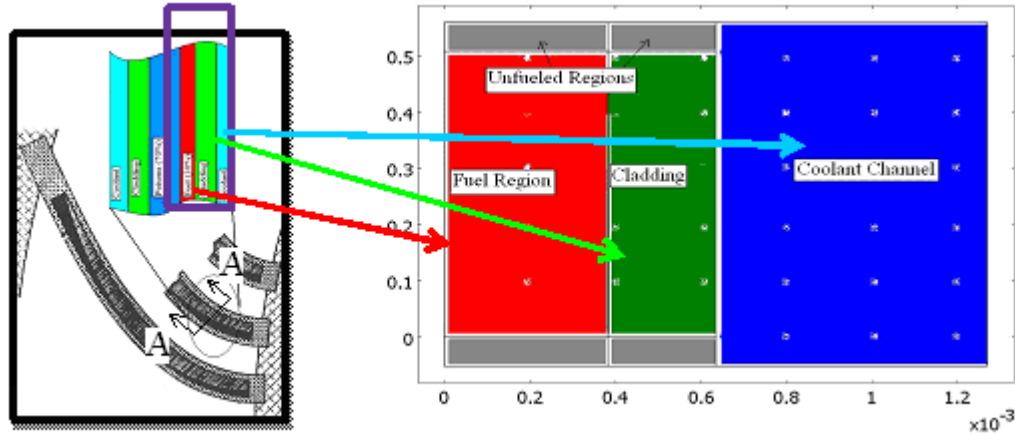
Fig. 7. COMSOL sub-channel model cross sectional view.

The first fuel conduction model homogenizes the fuel and poison, creating the non-stratified fuel plate model. This was done using the COMSOL General Heat Transfer (htgh) application mode. The non-stratified fuel plate through thickness cross-section is depicted with computational mesh in Fig. 8. This model parallels current core physics models which homogenize the fuel and poison layers into a single layer. The dimensions of this simulation are $4.50(10^{-4})$ by $1.27(10^{-3})$ meters.
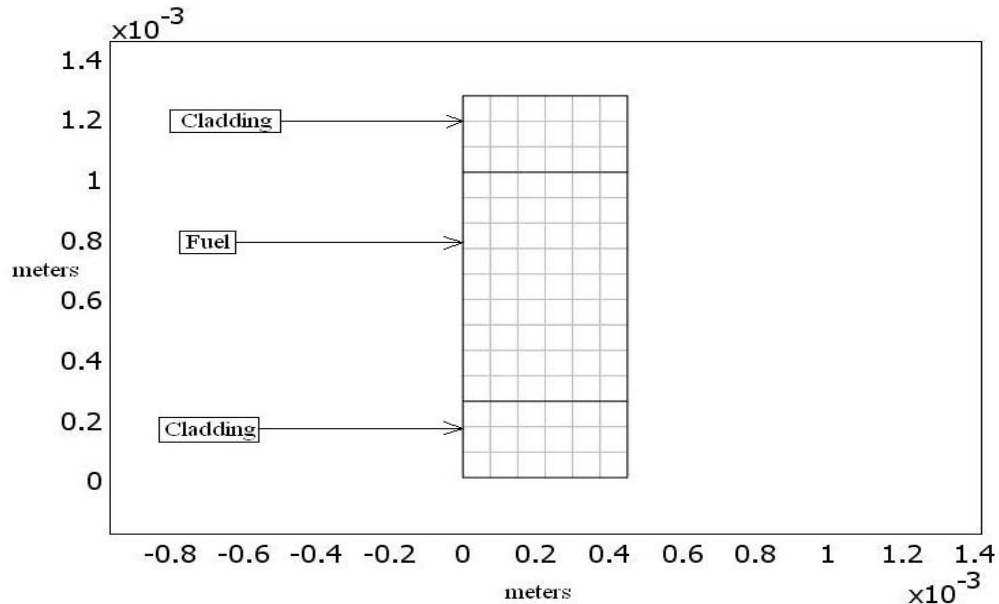
Fig. 8. Non-stratified fuel plate cross-section, 2-D conduction, dimensions in meters.

15

The quadrilateral mesh depicted in Fig. 8 is a COMSOL mapped mesh. The mapped mesh option in COMSOL allows the user to control whether the element distribution along a specified edge is linear or exponential, and in which direction the elements will be distributed. The mapped meshing option also allows the user to specify the ratio in size between the last and first element along the edge in the element ratio edit field (COMSOL Digital Guide).

The material properties used for the simulation of the non-stratified fuel plate are displayed in Table 2.

Table 2. Material thermal conductivities

Cladding	
181.3[1]	W/(m*K)
Fuel	
176.95[1]	W/(m*K)
Poison	
151.1	W/(m*K)

Morris and Wendel pg. 24-25[1]

The volumetric heating is given as,

$$q''' = \frac{Q}{V}$$
Eq. 40

where Q is the average core power, here taken as 80.7 MW, and V is the volume of fuel in the core, here taken as 0.03035808 m^3, giving volumetric heating of 2658270879 W/m^3. The boundary conditions used to simulate the non-stratified fuel plate are depicted in Fig. 9.
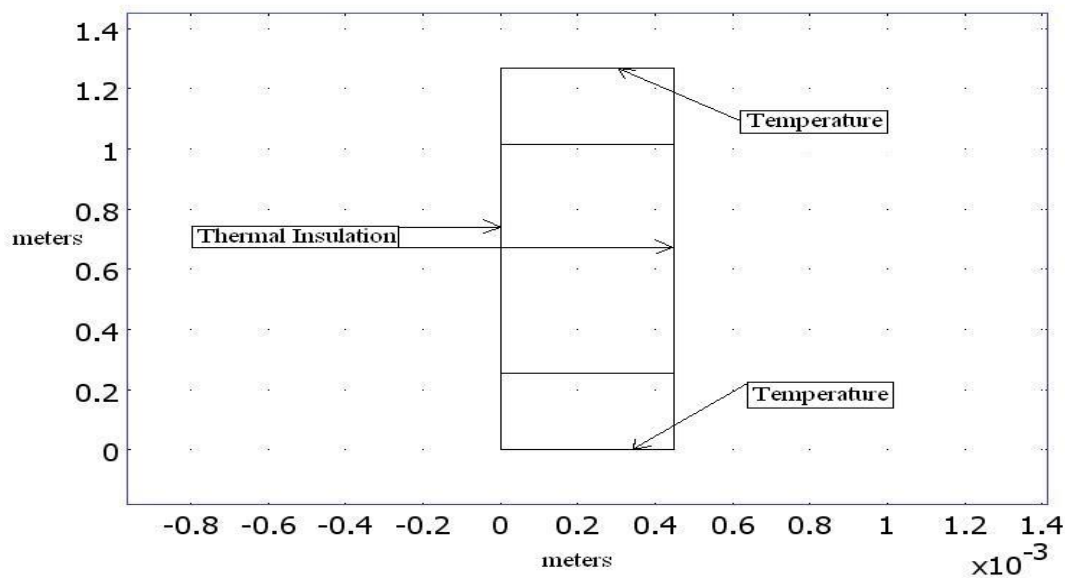
Fig. 9. Boundary conditions for non-stratified fuel plate, dimensions in meters.

All boundary/interface conditions not explicitly specified are, by default, COMSOL continuity boundaries. A continuity boundary condition is a way of insuring that there will be a continuous flux across the specified boundary. The temperature boundary condition is governed by,

$$T2 = T2_0 \qquad\qquad\qquad \text{Eq. 41}$$

The temperature that was specified for the cladding interface to coolant was $T2_0 = 321.9$ K. The thermal insulation boundary condition is described by,

$$-\mathbf{n}(-k\nabla T2) = 0 \qquad\qquad\qquad \text{Eq. 42}$$

For Equation 42 to be valid, the temperature gradient across the boundary must be zero. The equation governing the sub-domains in Fig. 8 is described by,

$$\nabla(-k\nabla T2) = Q \qquad\qquad\qquad \text{Eq. 43}$$

This simulation is shown in Fig. 10. The solver used in this simulation was the stationary direct (UMFPACK) linear system solver.
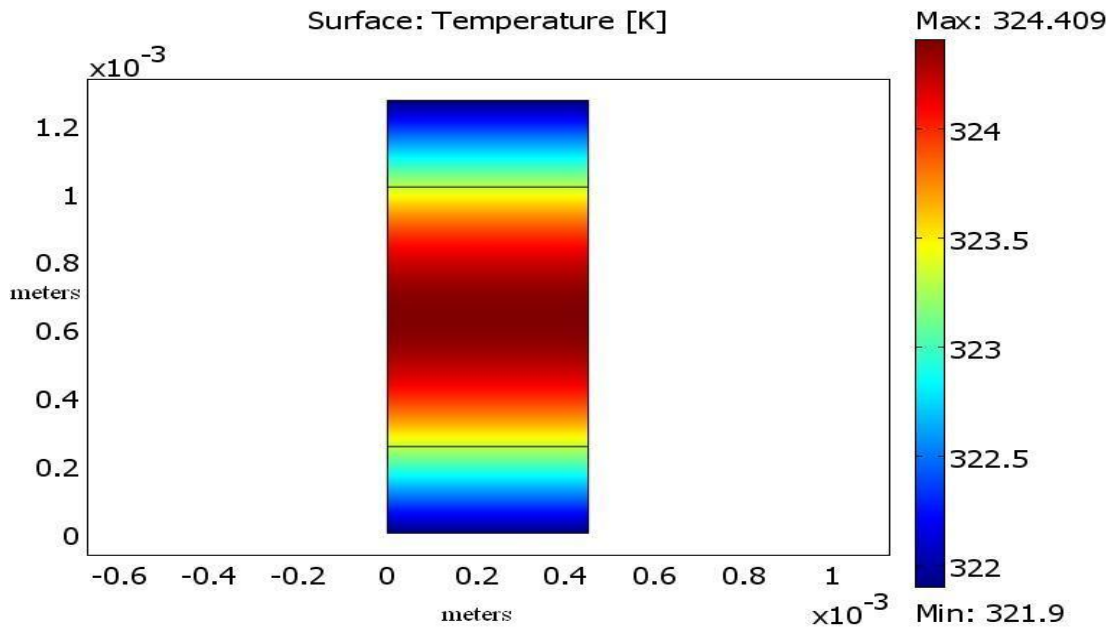
Fig. 10. Solution for a uniform power distribution of a non-stratified plate (2D_uniform_conductionv1.mph).

The next step was to simulate a plate with the fuel and poison explicitly modeled as separate regions, designated the stratified fuel plate model, with a uniform power distribution in the fuel. The geometry chosen for this simulation is depicted in Fig. 11.
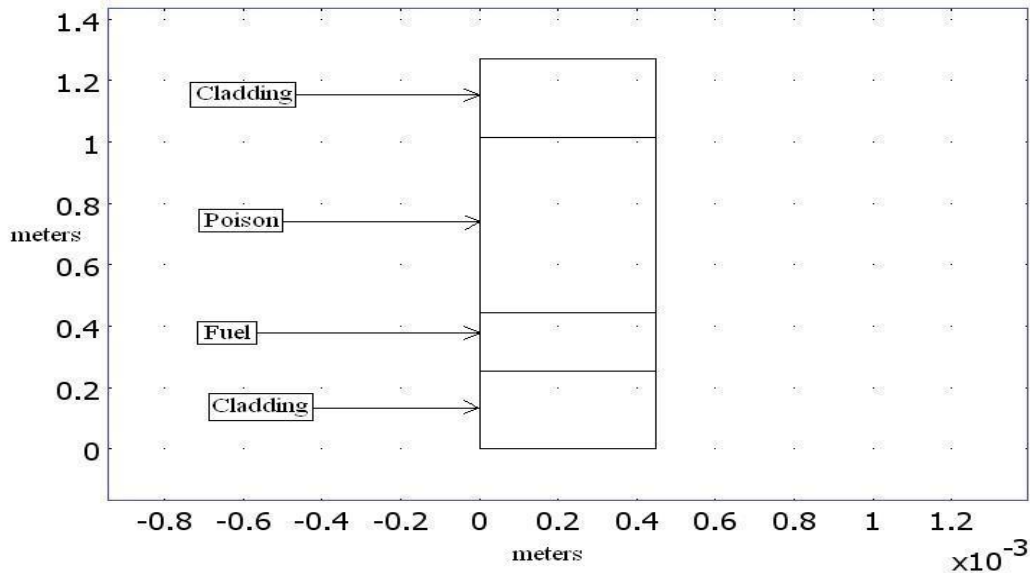
Fig. 11. Stratified fuel plate.

The addition of a poison volume and the resulting decrease in fuel volume, increases the fuel volumetric heating for a fixed power. The poison region shown in Fig. 11 has a thermal conductivity that is 16.6 percent lower than the value of the cladding. The value of the volumetric heating for the stratified simulation is 3544361172 W/m^3. This value was computed using Equation 39, where the fuel volume is now 0.02276856 m^3. This volume is 75 percent smaller than what is used in the non-stratified simulation. The boundary conditions for this simulation and computational mesh are shown in Fig. 12.
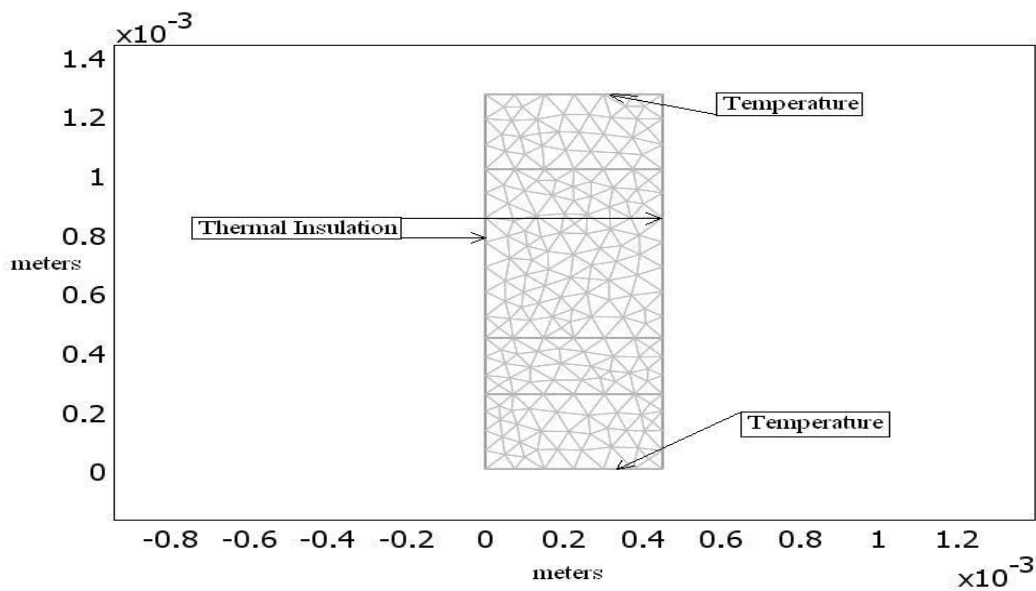
Fig. 12. Mesh and boundary conditions.

Note the mesh used in Fig. 12 is the COMSOL free mesh option, otherwise termed as unstructured mesh, using triangular elements. In the 2-dimensional environment, another free mesh option is available that uses quadrilateral elements instead of triangular elements. This option was not employed for simulations in this report. Figure 13 shows the solution for this simulation. The solver used in this simulation was the stationary direct (UMFPACK) linear system solver.
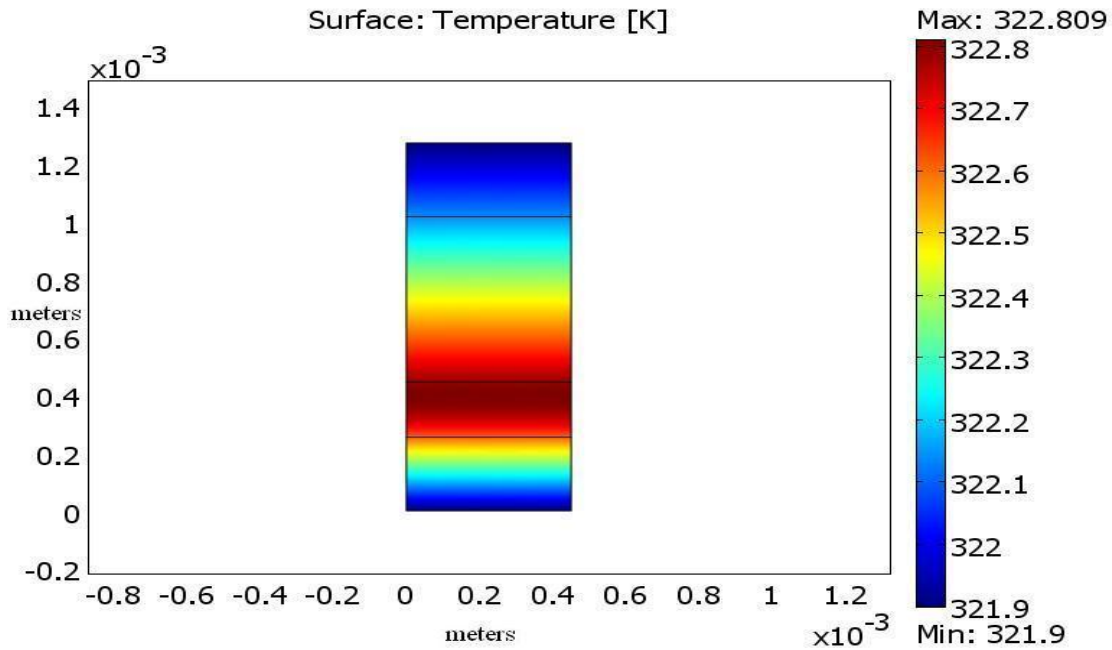
Fig. 13. Temperature profile for a uniform power distribution in a stratified plate (2D-nonuniform_conductionv1.mph).

The temperature indicator to the right of Fig. 10 and Fig. 13 depicts the peak fuel plate temperatures in the non-stratified and stratified fuel plate models. The temperature indicators show the non-stratified model results in a higher peak fuel temperature prediction than the stratified model. The stratified fuel region thickness changes with radial position, as shown in Fig. 2. Thinner fuel regions exaggerate this outcome.

While simulations are possible and various two dimensional fuel plate models are easy to implement, the accuracy of the conduction solutions will be related to the manner in which the computational domain is meshed. The COMSOL simulations are compared to exact analytical solutions for cases where the fuel is not stratified, the volumetric heat generation is uniform, the properties are constant, and the surface temperature is prescribed.

3.1 Analytical solution for fuel plate

Boundary conditions used in the analysis of the heat conduction are representative of the boundary conditions presented for the uniform non-stratified conduction models. Thermal conductivities are listed in Table 2. Figure 14 reflects a sketch of the 1-dimensional heat transfer problem. Equation 44 is integrated with appropriate boundary conditions being applied to obtain the temperature distribution in the cladding of the fuel plate

$$q'' = -k_{clad} \frac{dT}{dy} \qquad \text{Eq. 44}$$

where *q"* is the heat flux in the cladding and k_{clad} is the thermal conductivity of the cladding material. Equation 44 was solved assuming that the plate was thermally insulated in the x-direction and was an infinite plate in the z direction. The boundary condition applied to Equation 44 assumed that at the surface of the cladding the temperature was 321.9 K. The temperature distribution in the cladding can be obtained from,

$$T(y) = -\frac{1012801.205\,y}{181.3} + 325.4473181 \qquad \text{Eq. 45}$$

where *T(y)* is the temperature distribution in the *y* direction. Equation 45 yielded a temperature result for the clad/fuel interface of 324.7378539 K. Equation 46 was used to determine the temperature distribution in the fuel region

$$\frac{d}{dy}\left(k_{fuel} \frac{dT}{dy} \right) = -q''' \qquad \text{Eq. 46}$$

where *q'''* is the volumetric heat generation in the fuel and k_{fuel} is the thermal conductivity of the fuel meat. Assuming that there is no temperature jump at the fuel cladding interface and assuming that the heat generation in the fuel is symmetric, the temperature distribution in the fuel is given by,

$$T(y) = \frac{-2658270879\,y^2}{(176.95)(2)} + 324.4092841 \qquad \text{Eq. 47}$$

Equation 47 yields a max fuel centerline temperature of 324.4092841 K. This temperature is based on the assumption of a volumetric heat generation equal to 2658270879 W/m^3, corresponding to 80.7 MWth.

A graph of the analytical solution was generated using MATLAB and is reflected in Fig. 15. Also, plotted on this graph is the result that was generated in COMSOL for the 1-D solution. On average, the relative error between the COMSOL solution and analytical solution is $1.194(10^{-6})$. Even though the COMSOL solution is an approximation at specific nodes, the accuracy of the solution is good.
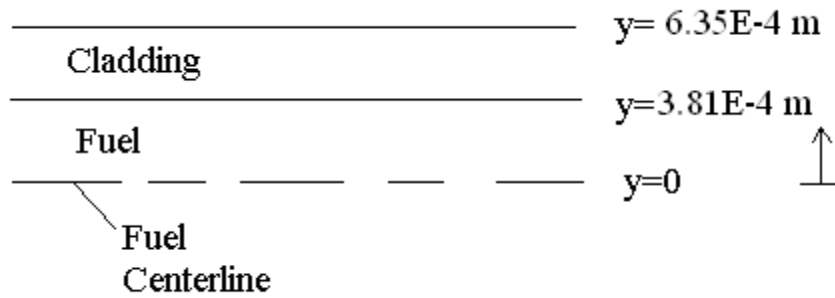
Fig. 14. Half of the fuel plate.
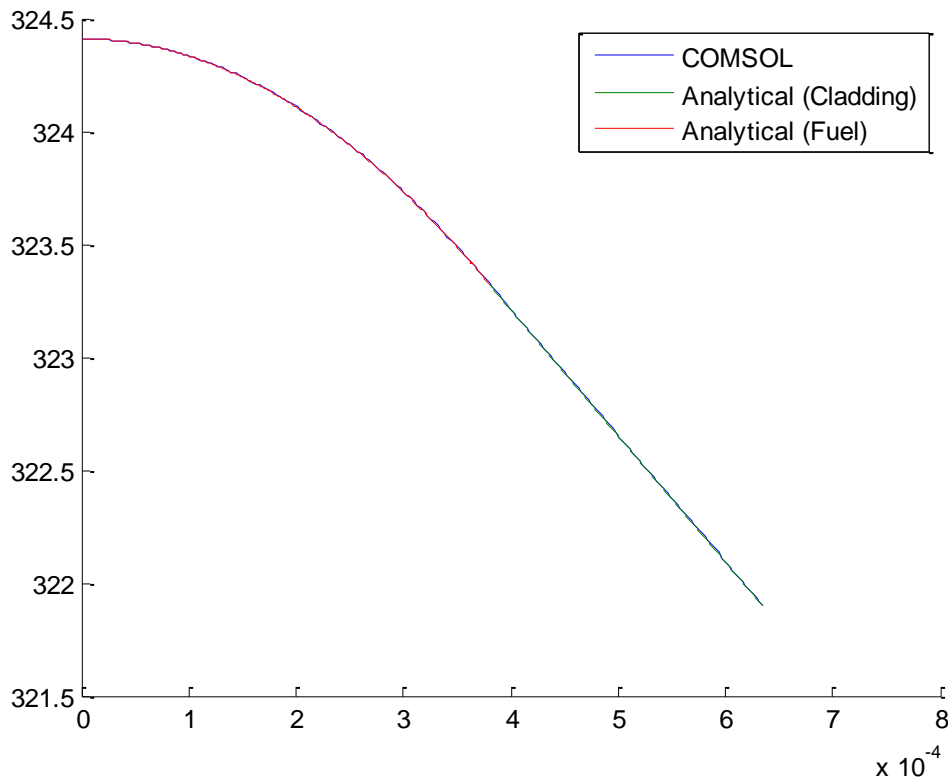
Fig. 15. COMSOL graph compared to analytical result.

3.2 COMSOL model of non-bond between fuel and clad

Next, a non-bond region between the fuel and cladding regions is simulated to ascertain the flexibility of the COMSOL simulation environment to model "real-world" manufacturing flaws. First the <u>non-stratified</u> plate was constructed with a non-bond region. The dimensions of the non-bond region in this simulation are $1(10^{-5})$ meters by $2(10^{-4})$ meters. The mesh for this simulation and boundary conditions are shown in Fig. 16. The mesh used in Fig. 16 is the COMSOL free mesh with triangular elements. This mesh contains $1(10^{3})$ elements and $2.3(10^{3})$ degrees of freedom. The results of this simulation are shown in Fig. 17.
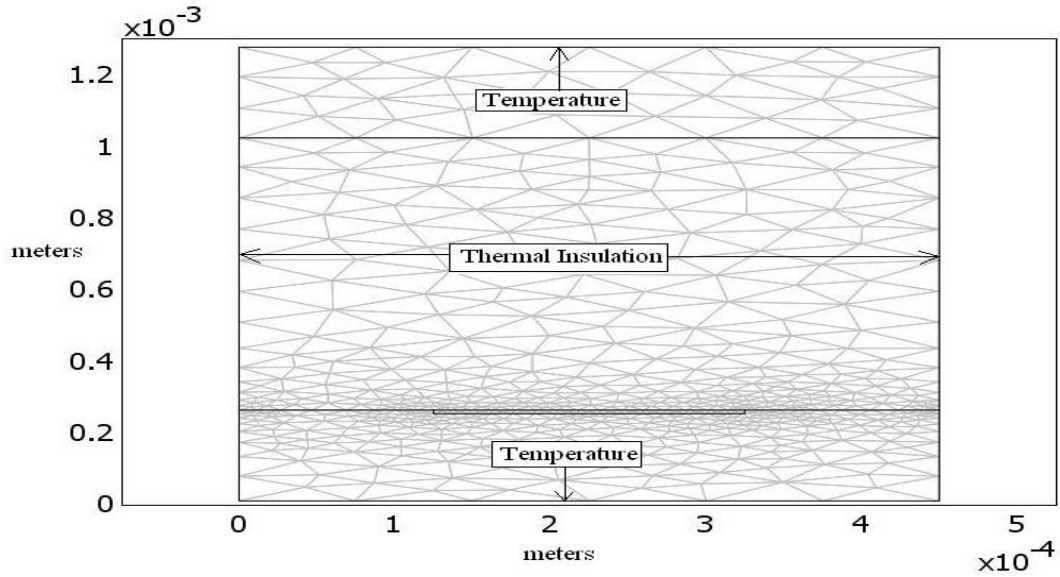
Fig. 16. Mesh and boundary conditions for non-stratified plate.
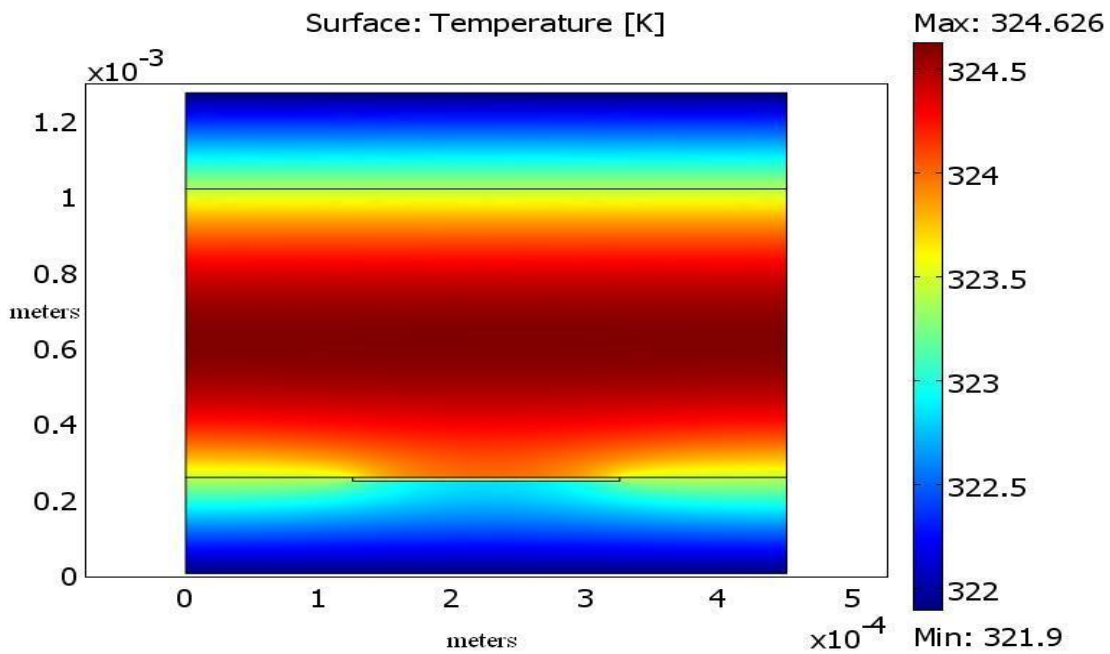
Fig. 17. Solution for non-stratified fuel plate with non-bond (2D-uniform_condcution_nonbondv1.mph).

Continuing this simulation to the <u>stratified</u> fuel and poison model, the mesh and boundary conditions for the stratified fuel case with clad to fuel non-bond are shown in Fig. 18.
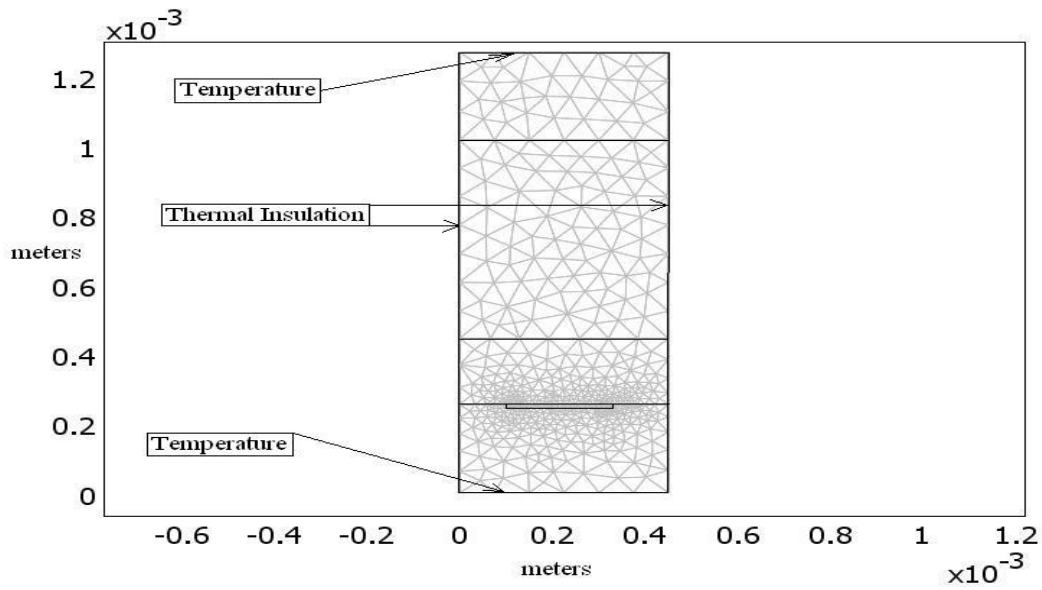
Fig. 18. Mesh and boundary conditions for stratified fuel plate and non-bond.

The result for the stratified fuel plate simulation with non-bond is depicted in Fig. 19. While the chosen fixed surface temperature boundary conditions are artificial, these added simulations indicate the more realistic stratified model of the fuel results in lower peak fuel temperatures.
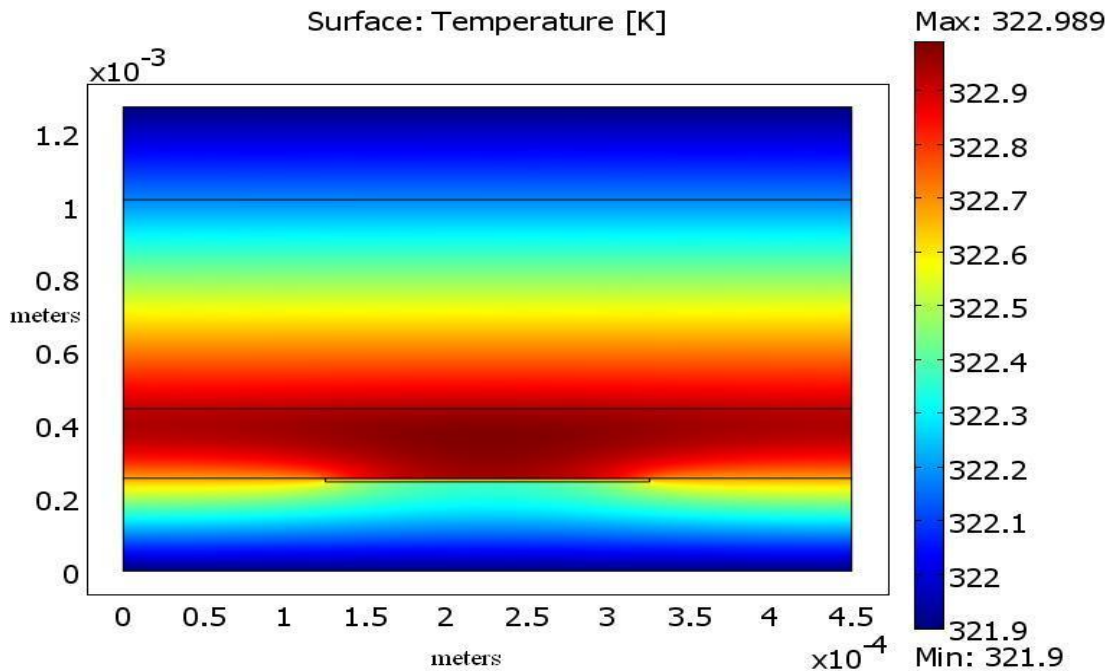
Fig. 19. Solution for stratified fuel plate with non-bond (2D_nonuniform_conduction_nonbondv1.mph).

23

3.3 Conclusions from insulated boundaries model

While the insulated boundaries model does not utilize the capability for multi-dimensional flow modeling in COMSOL, it does provide a basis in the COMSOL environment for direct comparison of outcomes with those from the legacy simulation code (McLain). The relative difference between the COMSOL solution and analytical solution is acceptably small. The ability to model the extent of a non-bond between fuel and clad significantly exceeds the ability to measure the phenomena; minimum diameter of a circular area of measurement being 1.524 mm.

4.0 CONVENTIONAL FUEL TO COOLANT MODELS FOR CODE VALIDATION

Software quality assurance procedures in practice at Research Reactors Division note that one method of verifying a computer program is to compare it to a different, previously verified computer program (verified over an identified area of applicability). To compare the COMSOL model to the currently accepted analysis methodology for HFIR (McLain code), a one dimensional fuel conduction model (from the plate to the coolant) should be mated to a one dimensional, axial fluid flow model (1D/1D). Due to the height of the fuel plate being much greater than the thickness and seven times greater than the span of the fuel plate, two dimensional conduction of heat inside the plate can be modeled with COMSOL with the results of the calculation being very similar to a 1D/1D model. The mating of the two dimensional fuel conduction model to a one dimensional axial fluid flow model is not as well supported in COMSOL as is a two dimensional fuel and two dimensional fluid flow model that can be accomplished using standard COMSOL Graphical User Interface (GUI) tools. The interface between the fuel conduction in the direction normal to the clad surface and the fluid which is flowing along the clad surface, perpendicular to the surface normal direction, would require some advanced techniques in COMSOL to implement and is beyond the scope of this research. However, this is how the McLain code functions, so a heat transfer coefficient is implemented to connect the fuel clad surface to the coolant.

The heat transfer coefficient boundary condition between the fuel model and one dimensional coolant flow was implemented to support the validation exercise. Conventional heat transfer coefficient models like the Modified Hausen model implemented by McLain derive their functional form from boundary layer theory with leading scalar coefficients, refinements in Reynolds Number and Prandtl Number exponents, and thermo-physical property variation corrections based on experimental data. The experimental data are mostly from uniformly heated tubes with steady fully developed flow. The heat transfer coefficient model captures the combined effects of flow turbulence and thermo-physical property variations to model the local temperature gradient at the wall in a relatively simple, algebraic format based on local fluid bulk temperature, fluid properties at bulk fluid temperature, local wall temperature, and cross sectional average flow velocity.

The modified Hausen model used in the McLain report and the revised modified Hausen model (Thomas, 1987) was compared to other heat transfer coefficient models in the literature. Several engineering heat transfer models for Nusselt Number in fully developed turbulent internal flows typical of the HFIR cooling channel flow were coded for comparison with COMSOL outcomes. The Dittus-Boelter model is very commonly used, and has no explicit correction for thermo-physical property variations across the thermal boundary layer,

$$Nu_{db} = 0.023 \, \mathrm{Re}^{0.8} \, \mathrm{Pr}^{0.4} \qquad\qquad\qquad \text{Eq. 48}$$

However, the exponent for the Prandtl number changes to 0.3 if the fluid is being cooled.

Seider-Tate is also commonly used and includes a thermo-physical property variation correction through a ratio of bulk and wall viscosities,

$$Nu_{st} = 0.027 \, \mathrm{Re}^{0.8} \, \mathrm{Pr}^{0.333} (\mu_{bulk} / \mu_{wall})^{0.14} \qquad\qquad \text{Eq. 49}$$

Both Dittus-Boelter and Seider-Tate models use exponents for Reynolds number and Prandtl number that follow closely with boundary layer theory and the so-called Reynolds analogy for fluids with Prandtl numbers of order unity.

Steady state heat transfer coefficients in the HFIR core cooling channels are modeled in the McLain code using the modified Hausen correlation. From the McLain report, the model is,

$$Nu_{mh} = 0.116\{(\mathrm{Re})^{2/3} - 125\}\mathrm{Pr}^{1/3}[\mu_{bulk}/\mu_{wall}]^{0.14}$$ Eq. 50

The modified Hausen model uses an identical thermo-physical property adjustment to that of Seider-Tate, but uses Reynolds number exponent equal 2/3. However, in 1987 this model was revised to:

$$Nu_{revised-mh} = 0.0235\{\mathrm{Re}^{0.8} - 230\}\left[1.8\mathrm{Pr}^{0.3} - 0.8\left(\frac{\mu_{bulk}}{\mu_{wall}}\right)^{0.14}\right]$$ Eq. 51

The four models are compared in Fig. 20 for typical fully developed HFIR core flow conditions. The modified Hausen model predicts lower wall-to-fluid heat transfer coefficients than does Dittus-Boelter and Seider-Tate for steady state HFIR conditions. Modified Hausen appears to be quite conservative when compared with other standard models used for turbulent internal flow.

Specific properties used for this comparison are provided in Table 3. The MATLAB code used for this preliminary comparison is provided in Appendix A. The wall temperature was not converged for this comparison, with the value determined from Dittus-Boelter used to evaluate the wall viscosity in all cases. Thus, the viscosity correction is underrepresented for the Hausen models, which will reduce the predicted wall temperatures slightly.
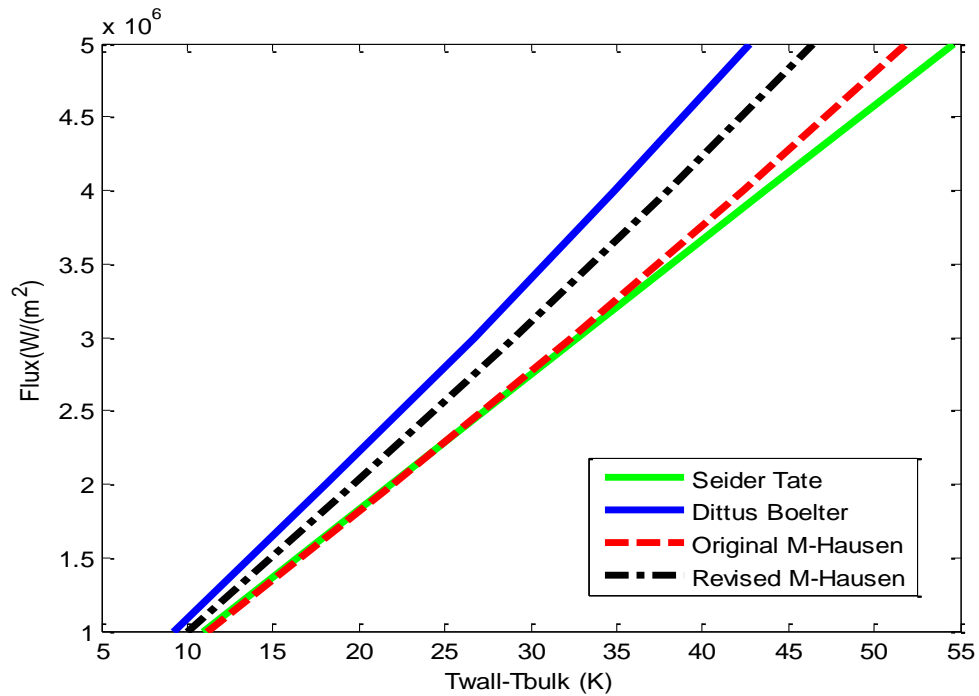

Fig. 20. Comparison of engineering heat transfer models for HFIR steady state conditions, flux versus wall temperature minus bulk temperature.

The domain of the 2-dimensional conduction to a 1-dimensional fluid flow as simulated in COMSOL is that of a half fuel plate in conjunction with a half coolant channel as shown in Fig. 21.

26

Table 2. Conditions for model comparison
(from Holman, Heat Transfer,Table A-9)

Bulk Temperature	76.7 C
Velocity	15.895 m/s
Viscosity	$3.47(10^{-4})$ Kg/m-s
Density	970.2 Kg/m^3
Hydraulic Diameter	a. 0.0025 m
Prandtl Number	2.16
Liquid Conductivity	0.673 W/m-C
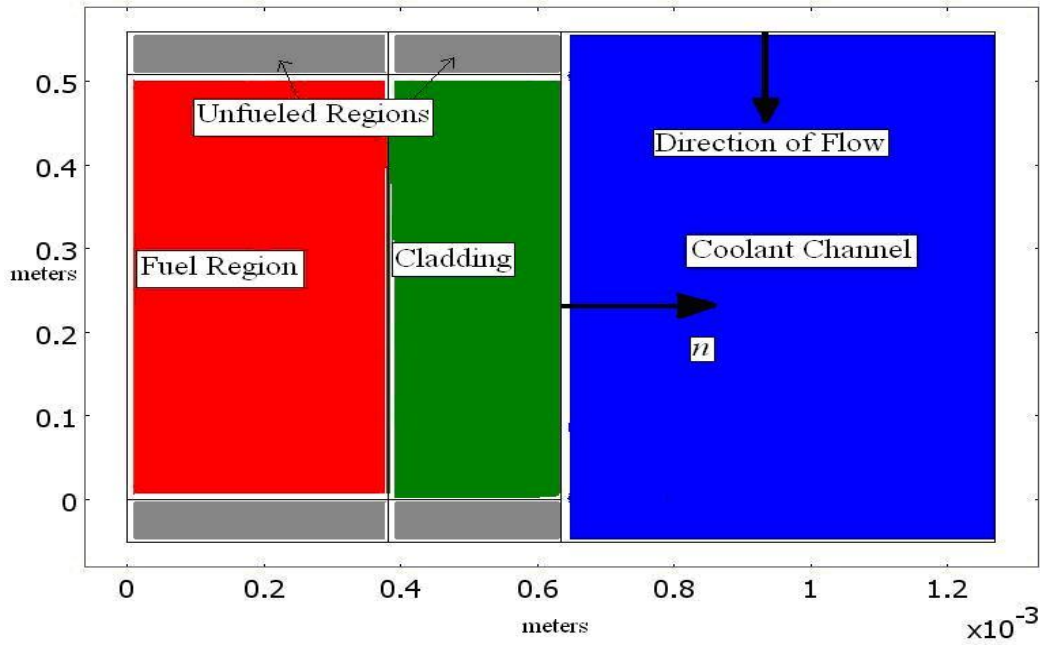
Fig. 21. Half fuel plate and half coolant channel.

4.1 Theoretical bases of COMSOL application modes for simulating current HFIR methods

In order to simulate the heat transfer between the fuel plate and the coolant using the conventional algebraic heat transfer coefficient format, three different modeling application modes in COMSOL must be employed. These application modes are Weakly Compressible Navier-Stokes (chns), Convection and Conduction (chcc), and General Heat Transfer (htgh).

The Weakly Compressible Navier-Stokes module employs Equation 52 and Equation 53 to model the fluid flow in the coolant sub-domain.

$$\rho\mathbf{u} \bullet \nabla \mathbf{u} = \nabla \bullet \left[-p\mathbf{I} + \eta\left(\nabla\mathbf{u} + (\nabla\mathbf{u})^T\right) - \left(\frac{2\eta}{3} - \kappa_{dv}\right)(\nabla \bullet \mathbf{u})\mathbf{I} \right] + \mathbf{F} \qquad \text{Eq. 52}$$

$$\nabla \bullet (\rho\mathbf{u}) = 0 \qquad \text{Eq. 53}$$

where ρ is the density, *u* is the velocity field, *p* is the pressure, *I* is the moment of inertia, η is the dynamic viscosity, κ_{dv} is the dilatational viscosity, and *F* is the volume force vector.

The Convection and Conduction module employs Equation 54 to model the heat transfer in the fluid.

$$\nabla\left(-k\nabla T + \sum_i h_i \mathbf{N}_{D,i}\right) = Q - \rho C_p \mathbf{u} \bullet \nabla T$$

Eq. 54

where k is the thermal conductivity, T is the temperature, $h_i N_{D,I}$ concern species diffusion (inactive for these simulations), Q is the volumetric heat source, and C_p is the heat capacity at constant pressure.

The General Heat Transfer module employs Equation 55 to model the heat conduction in the fuel plate.

$$\nabla \bullet \left(-k\nabla T2\right) = Q$$

Eq. 55

Similar to the conduction modeling, the material properties were assigned constant values. The values listed in Table 2 apply for these simulations. In addition Table 4 displays the material property values used for the coolant. These properties are evaluated at 333.45 Kelvin.

Table 3. Coolant properties at 333.45 K

Thermal Conductivity	0.65414 [1]	W/(m*K)
Density	982.91 [1]	kg/m^3
Heat Capacity	4185 [1]	J/(kg*K)
Dynamic Viscosity	$4.6416(10^{-4})$ [1]	Pa*s

[1]Incropera

The boundary conditions for the Weakly Compressible Navier-Stokes application mode are displayed in Fig. 22.
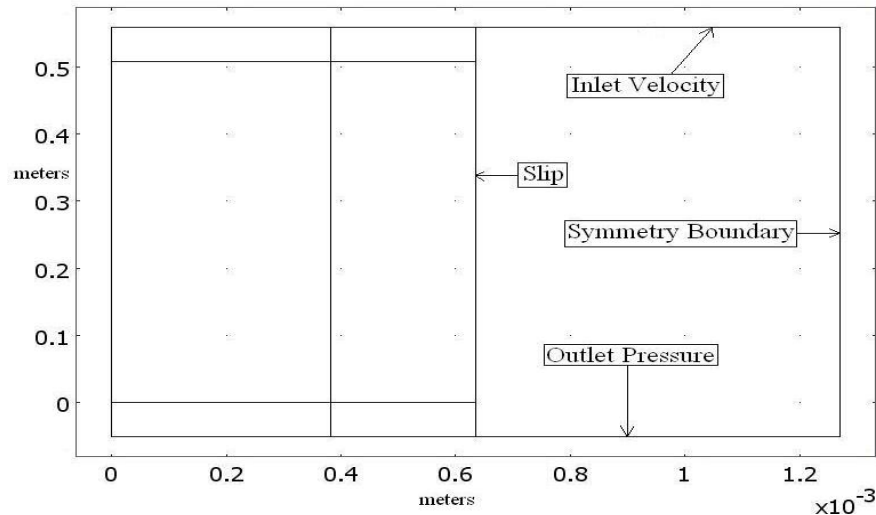

Fig. 22. Weekly compressible Navier-Stokes boundary conditions.

Equation 56 prescribes the inlet velocity.

$$\mathbf{u} = \mathbf{u}_0$$
Eq. 56

where *u* is the velocity field.
    The COMSOL slip condition is prescribed by Equation 57 and Equation 58.

$$\mathbf{n} \bullet \mathbf{u} = 0$$
Eq. 57

$$\mathbf{t} \bullet \left[-p\mathbf{I} + \eta\left(\nabla\mathbf{u} + (\nabla\mathbf{u})^T\right) - \left(\frac{2\eta}{3} - \kappa_{dv}\right)(\nabla \bullet \mathbf{u})\mathbf{I} \right]\mathbf{n} = 0$$
Eq. 58

where *n* is the unit normal vector and is depicted in Fig. 21, t is the tangential vector to the boundary, and *I* is the unit matrix. Equation 58 specifies that there can be no flow through the boundary. As a consequence of the slip condition there is no wall shear and no boundary layer development simulated.
    The symmetry boundary condition is derived from the following normal stress boundary condition:

$$\left(-p\mathbf{I} + \eta\left(\nabla\mathbf{u} + (\nabla\mathbf{u})^T\right)\right)\mathbf{n} = -f_0\mathbf{n}$$
Eq. 59

Where the total stress on a boundary is set equal to a stress vector of magnitude, f_0, oriented in the negative normal direction (COMSOL Digital Guide). This will lead to Equation 60, where the total stress in the tangential direction is zero.

$$p = 2\eta\frac{\partial u_n}{\partial n} + f_0$$
Eq. 60

As $\dfrac{\partial u_n}{\partial n}$ becomes small, Equation 60 approaches $p=f_0$. This finally allows for the development of a symmetry boundary condition, where there is no flow through the boundary and shear stresses are zero. The representative equation for the symmetry boundary condition is therefore prescribed by Equation 44 and Equation 59.
    The outlet pressure is prescribed by,

$$\left[\eta\left(\nabla\mathbf{u} + (\nabla\mathbf{u})^T\right) - \left(\frac{2\eta}{3} - \kappa_{dv}\right)(\nabla \bullet \mathbf{u})\mathbf{I} \right]\mathbf{n} = 0$$
Eq. 61

$$p = p_0$$
Eq. 62

where *p* is the pressure, and p_0 is the prescribed outlet pressure value.
    The boundary conditions for the Convection and Conduction modeling application mode are displayed in Fig. 23.
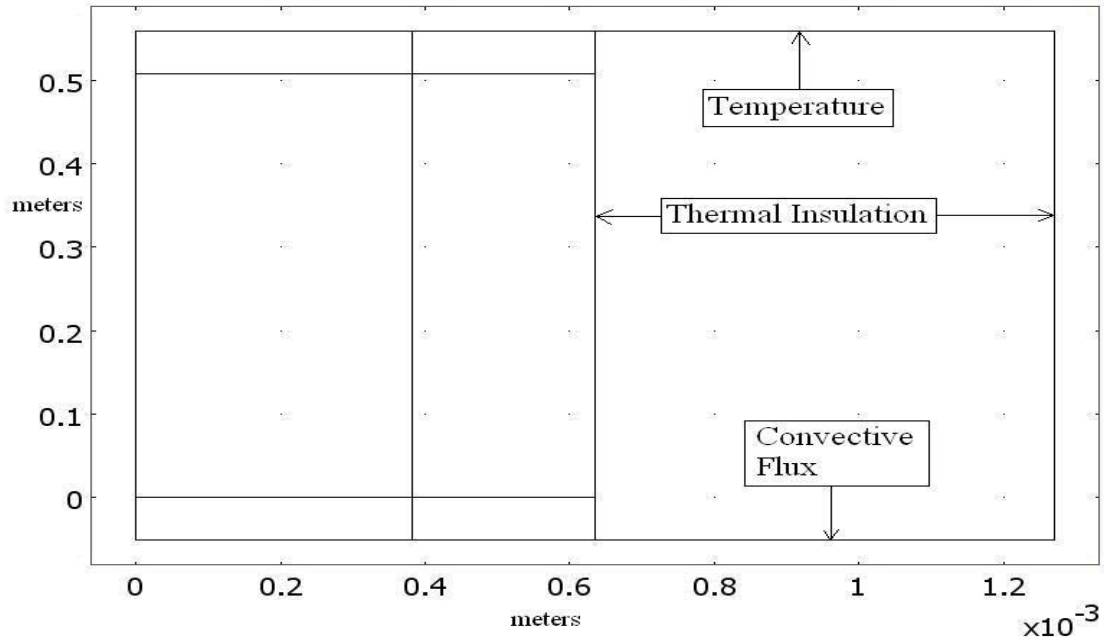
Fig. 23. Convection and conduction boundary conditions.

The thermal insulation boundary condition is prescribed by,

$$\mathbf{n} \bullet \mathbf{q} = 0 \qquad \qquad \text{Eq. 63}$$

$$\mathbf{q} = -k\nabla T + \rho C_p T\mathbf{u} \qquad \qquad \text{Eq. 64}$$

The convective flux boundary condition is prescribed by,

$$\mathbf{n} \bullet \left(-k\nabla T \right) = 0 \qquad \qquad \text{Eq. 65}$$

The boundary conditions for the General Heat Transfer modeling application mode are displayed in Fig. 24.

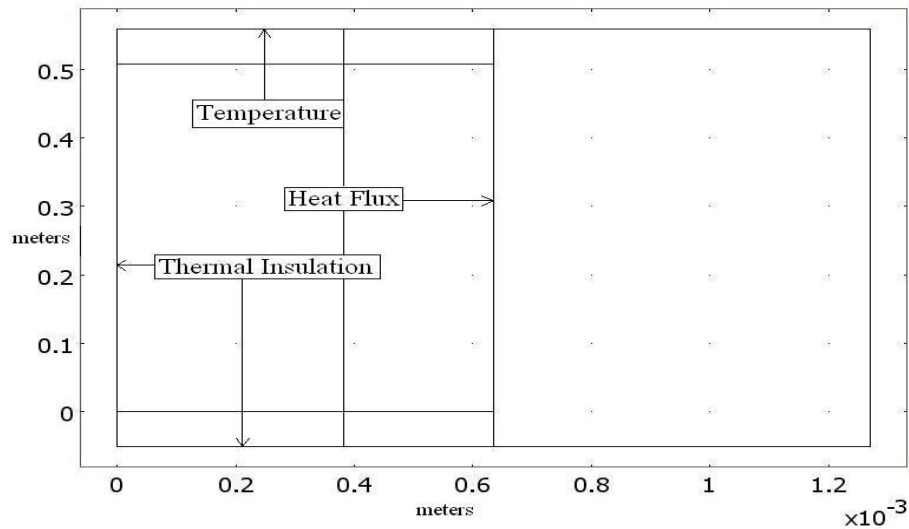**Fig. 24. General heat transfer boundary conditions.**

30

The temperature boundary condition is prescribed by,

$$T2 = T2_0 \qquad \text{Eq. 66}$$

This condition forces the finite element simulation to return a solution in which the above condition is either true or closely approximated (COMSOL Digital Guide).

The heat flux boundary condition is prescribed by,

$$-\mathbf{n} \bullet \left(-k\nabla T2\right) = q_0 + h\left(T_{\text{inf}} - T2\right) \qquad \text{Eq. 67}$$

where h is the heat transfer coefficient, T_{inf} is the ambient bulk temperature, and q_0 is the inward heat flux.

The thermal insulation boundary condition is prescribed by,

$$-\mathbf{n} \bullet \left(-k\nabla T2\right) = 0 \qquad \text{Eq. 68}$$

An extrusion coupling variable must be employed to map the conduction of the heat from the fuel plate to the clad to obtain a successful simulation of the heat transfer from the fuel plate into the coolant. Table 5 is a list of variable values used in this simulation.

Table 4. Half fuel and half coolant channel values

Heat Transfer Coefficient	88392	$W/(m^2*K)$
Inlet Velocity	-15.895	m/s
Inlet Temperature	321.9	K
Volumetric Heating	$2.66(10^9)$	W/m^3

4.2 Results of COMSOL simulations

The first simulation was for uniform volumetric heating. Included in this simulation are the spaces above and below the active fuel region where no heat is generated. Figure 25 displays the mesh that was used for this simulation.
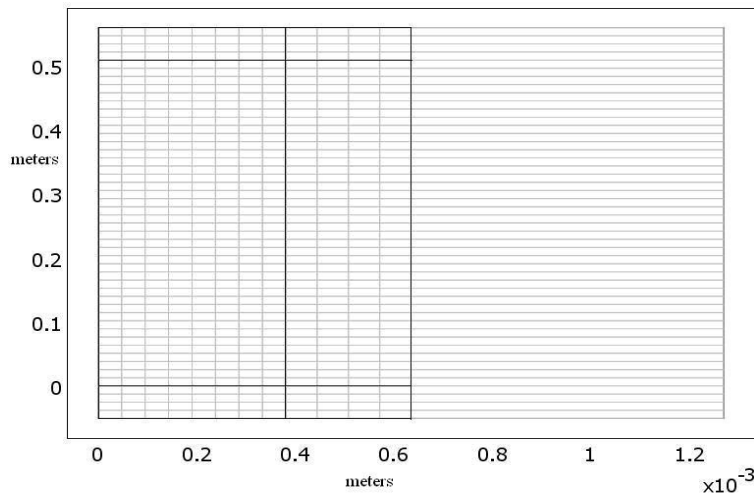
Fig. 25. Half fuel plate and coolant channel mesh.

31

The solver used for Figs. 26-27 and 30-31 is Stationary. Direct (PARDISO). PARDISO works on general systems of the form $Ax = b$, (COMSOL Digital Guide).

The result for the temperature distribution in the coolant is depicted in Fig. 26.
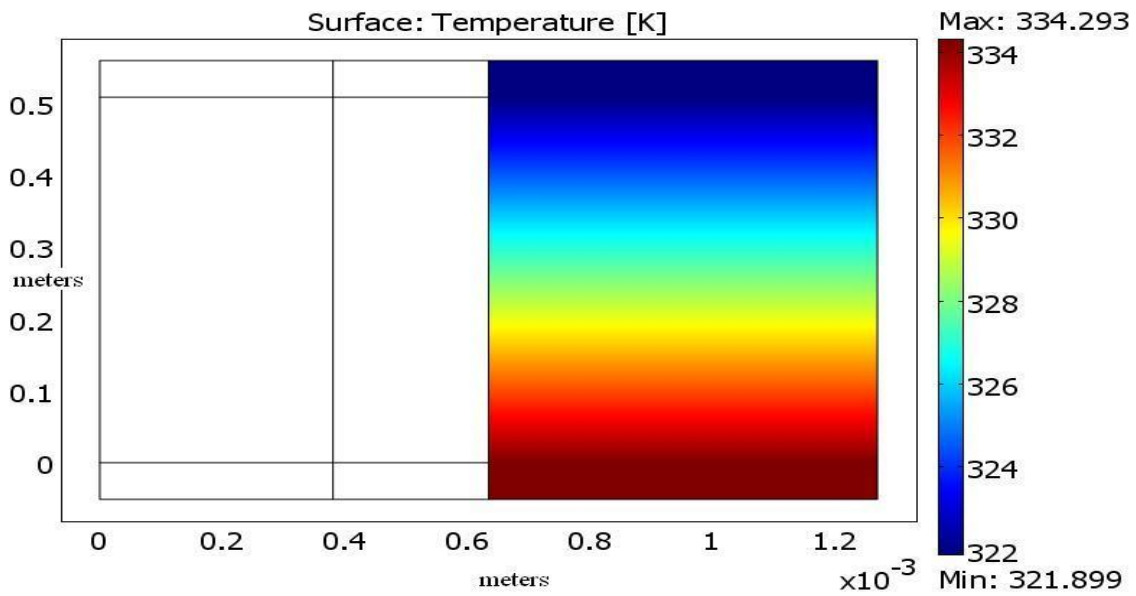
Fig. 26. Coolant temperature profile, uniform power density (Uniform_inactive_regionsv1.mph).

The temperature distribution in the fuel plate is shown in Fig. 27. Figure 27 shows, spikes in the temperature profile at the top of the fuel material and bottom of the fuel material. A temperature trace for the fuel is shown in Fig. 28. The simulated spikes in the temperature profile are a result of the mapped mesh coarseness used in the simulation.
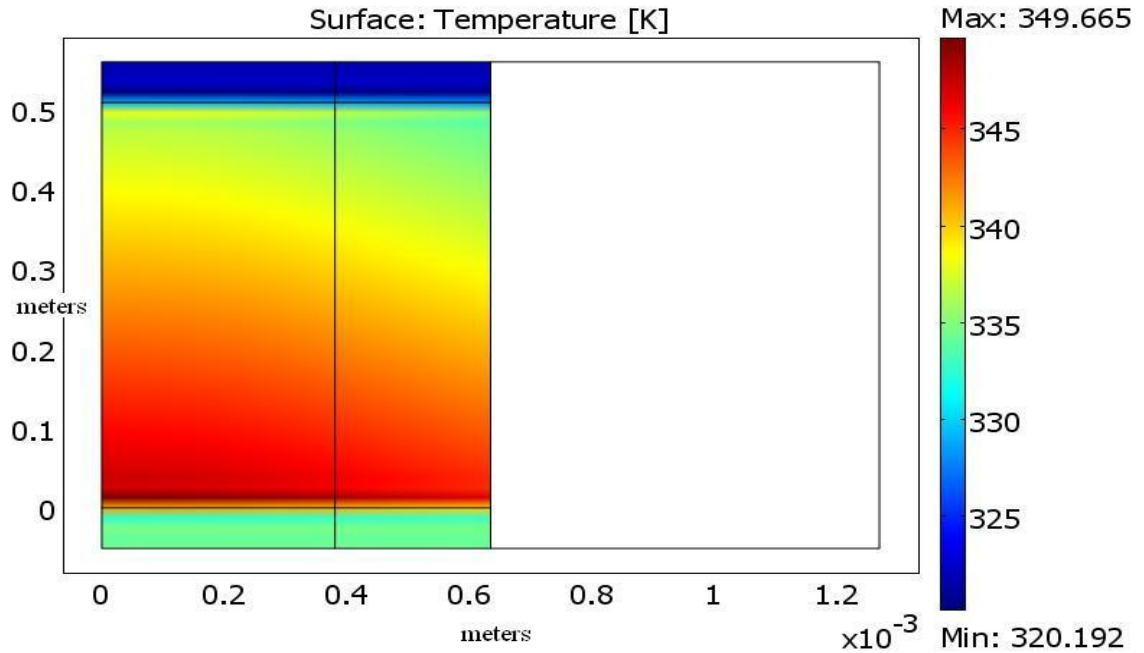
Fig. 27. Temperature profile for fuel region, uniform power density (Uniform_inactive_regionsv1.mph).
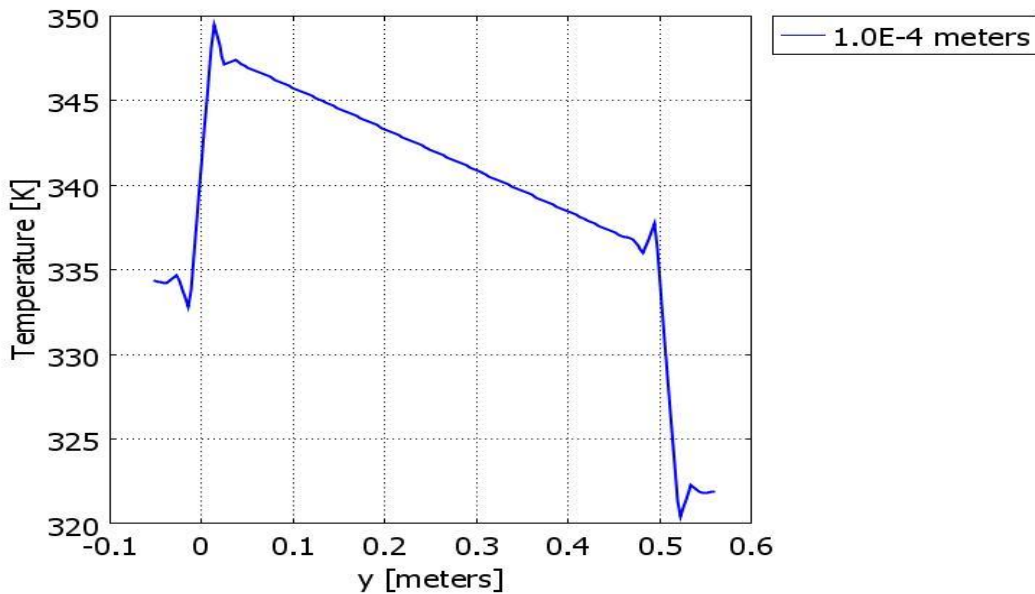
Fig. 28. Temperature trace for mapped mesh (Uniform_inactive_regionsv1.mph).

When a sufficiently dense mesh is used these spikes do not occur. Employing a more dense generated mesh shown in Fig. 29, resolves the temperature spikes. Figure 29 has approximately 180,000 additional elements (too fine to be visible) compared to the coarse mesh shown in Fig. 25. The resulting temperature profiles in the coolant and fuel material are shown in Figs. 30 and 31.
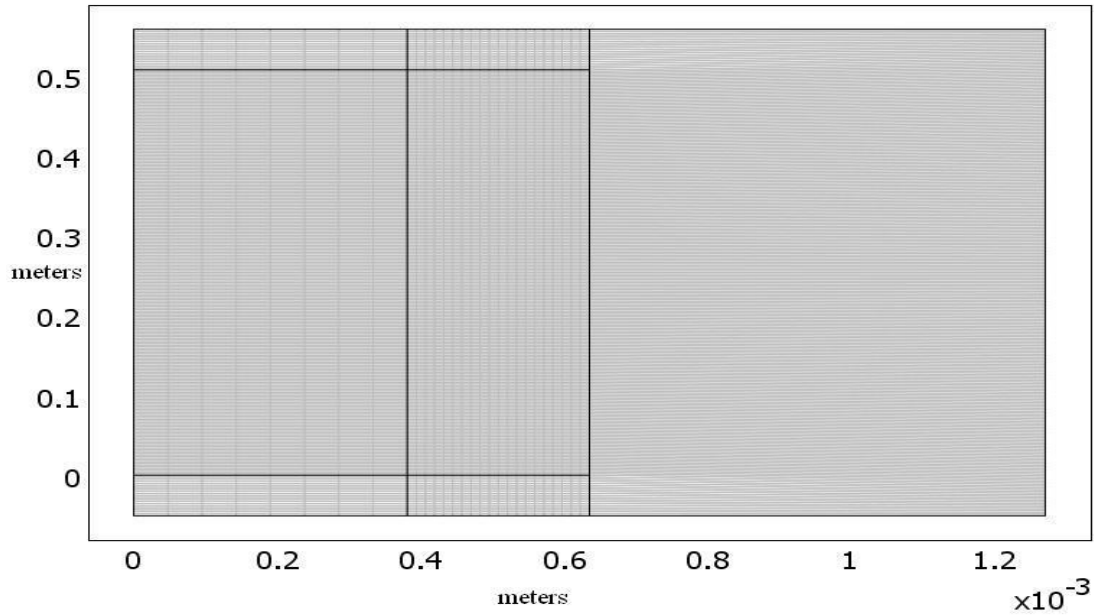
Fig. 29. Refined mapped generated mesh (Uniform_inactive_regionsv4.mph).
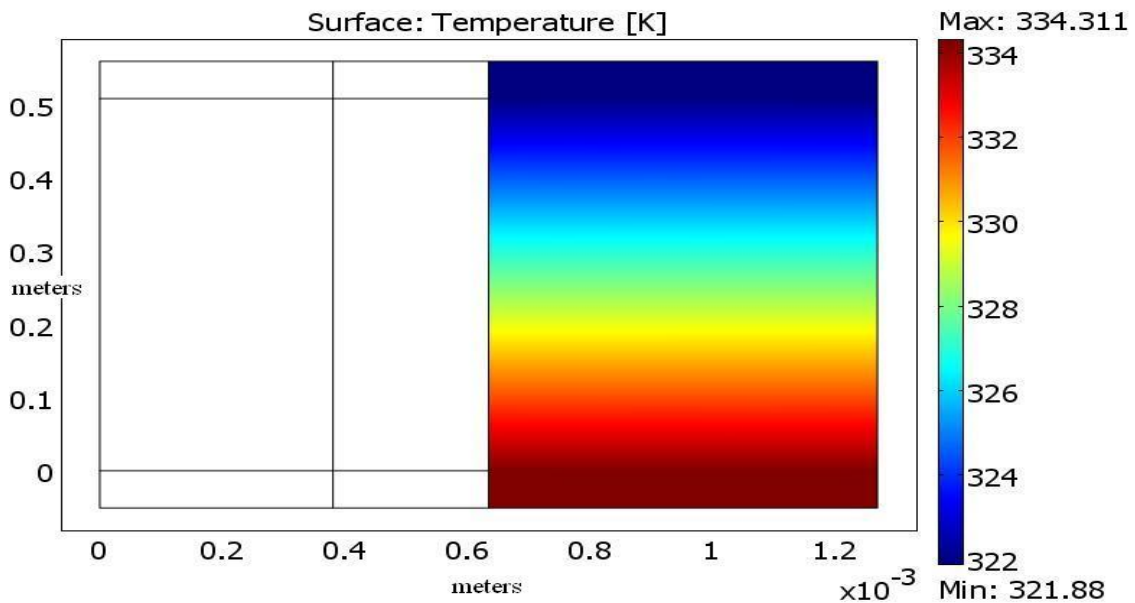
Fig. 30. Temperature profile for coolant channel (Uniform_inactive_regionsv4.mph).
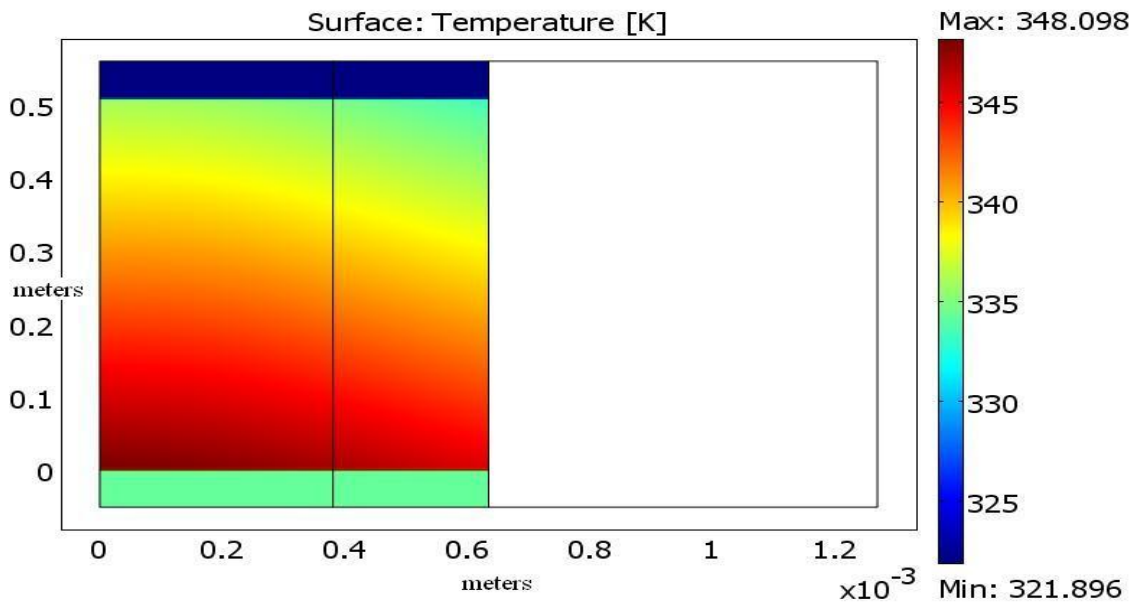
Fig. 31. Temperature profile for the fuel plate (Uniform_inactive_regionsv4.mph).

A temperature trace for the fuel, at the same position as in Fig. 28, is shown in Fig. 32. The temperature spikes have been resolved.
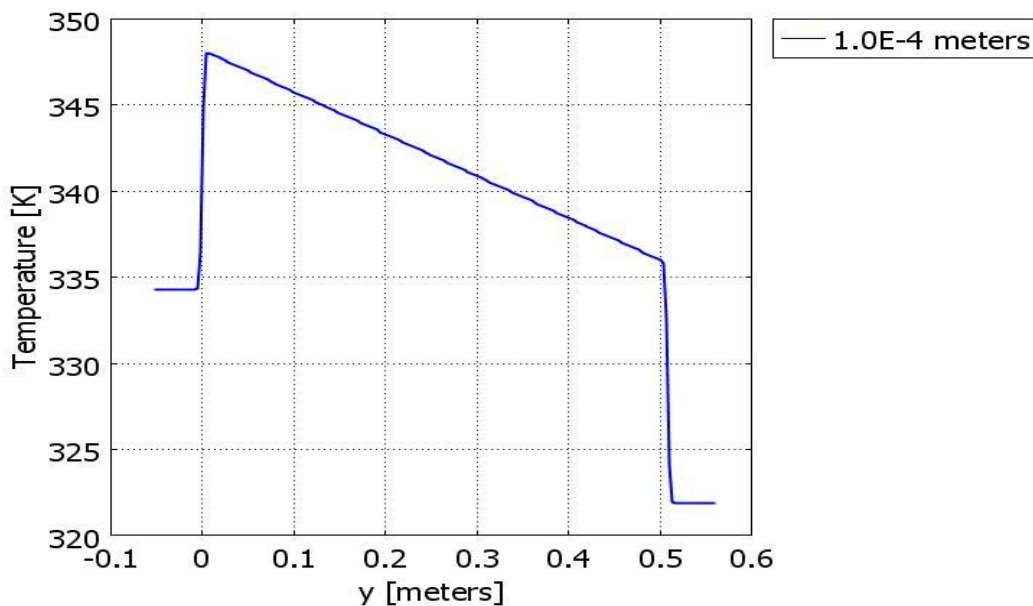
**Fig. 32. Temperature trace for refined mapped generated mesh
(Uniform_inactive_regionsv4.mph).**

A typical HFIR non-stratified sub-channel power distribution is given in Fig. 33 and Table 6. The axial multipliers listed in the first column of Table 6 correspond to a single stripe within a peak sub-channel at beginning-of-cycle that is documented in the HFIR Safety Analysis Report and is included as an appendix to this report. The HFIR HEU power distribution is

determined by multiplying the volumetric power production, 2658270879 W/m^3, by an axial multiplier that corresponds to an axial position in the core. This power distribution was used to generate a volumetric heating distribution in the fuel and was simulated using the same approach as that for the uniform power distribution. Figure 34 is a representation of the mesh used for simulating the HFIR sub-channel power distribution. The same boundary conditions and modeling application modes used for the uniform power distribution model are used for the HFIR representative power distribution. Figure 35 depicts the temperature profile within the fuel plate.
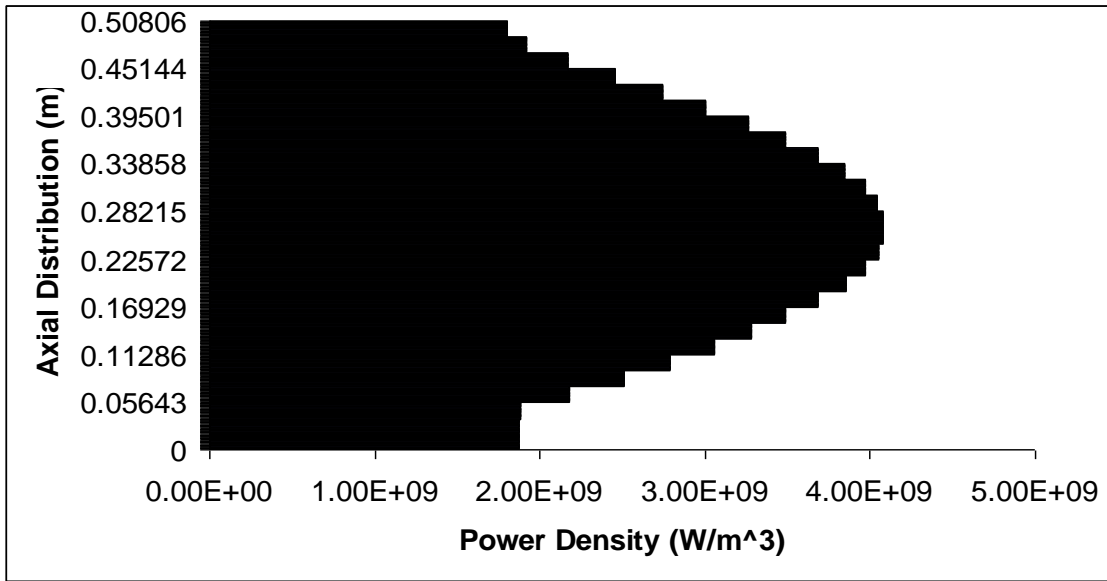
Fig. 33. HEU HFIR power profile (axial position in meters at left).

Table 5. Fuel power distribution sub-channel axial multipliers

Axial multipliers	Power distribution (10^9 W/m^3)
0.678	1.802
0.722	1.919
0.815	2.166
0.924	2.456
1.031	2.741
1.13	3.004
1.227	3.262
1.312	3.488
1.387	3.687
1.447	3.847
1.493	3.969
1.52	4.041
1.532	4.072
1.533	4.075
1.523	4.049
1.494	3.971
1.448	3.849
1.384	3.679
1.312	3.488
1.235	3.283
1.148	3.052
1.05	2.791
0.944	2.509
0.819	2.177
0.709	1.885
0.706	1.877
0.703	1.869
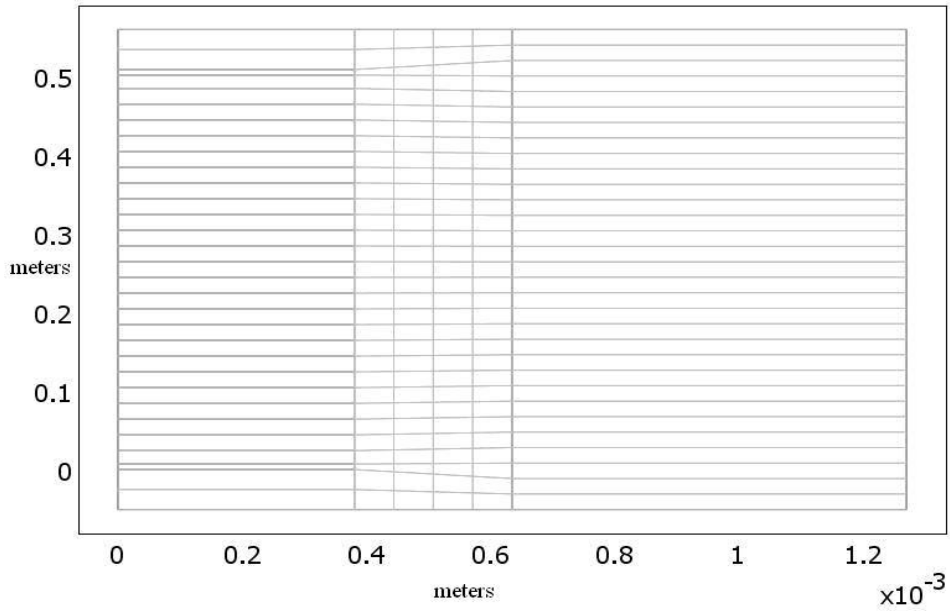
Fig. 34. Mesh of fuel plate with varying power density.
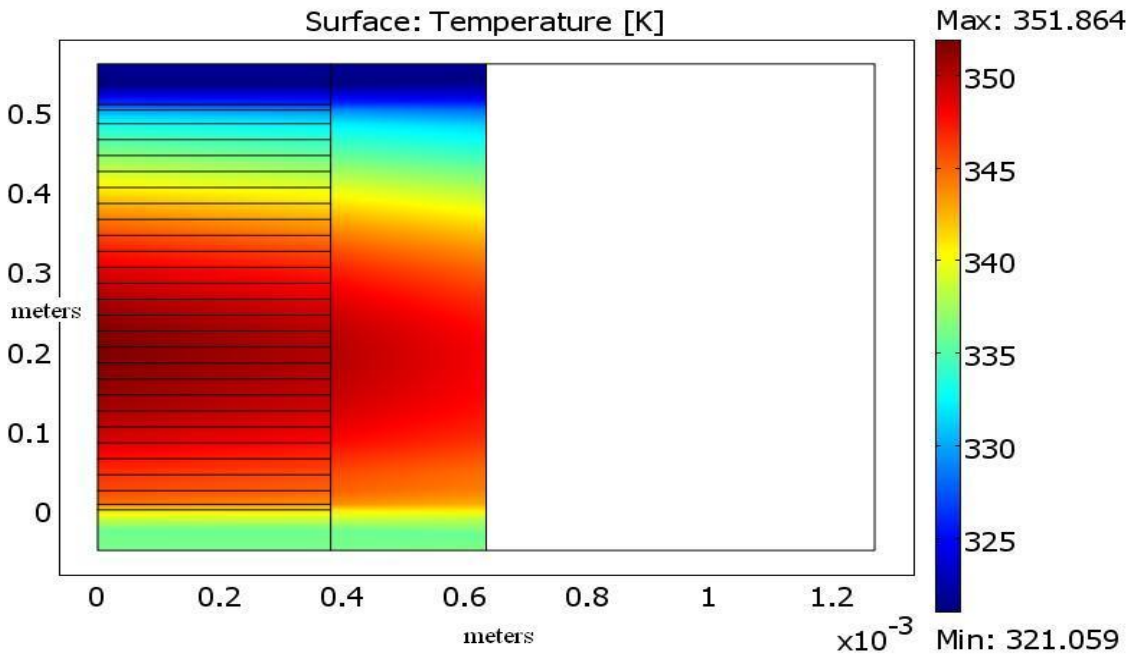
Fig. 35. Temperature profile in the fuel region with varying power density fuel plate (HFIR_dist_inactivev1.mph).

Figure 36 depicts the temperature profile in the coolant for the typical axial power distribution and inactive inlet and exit regions.

38
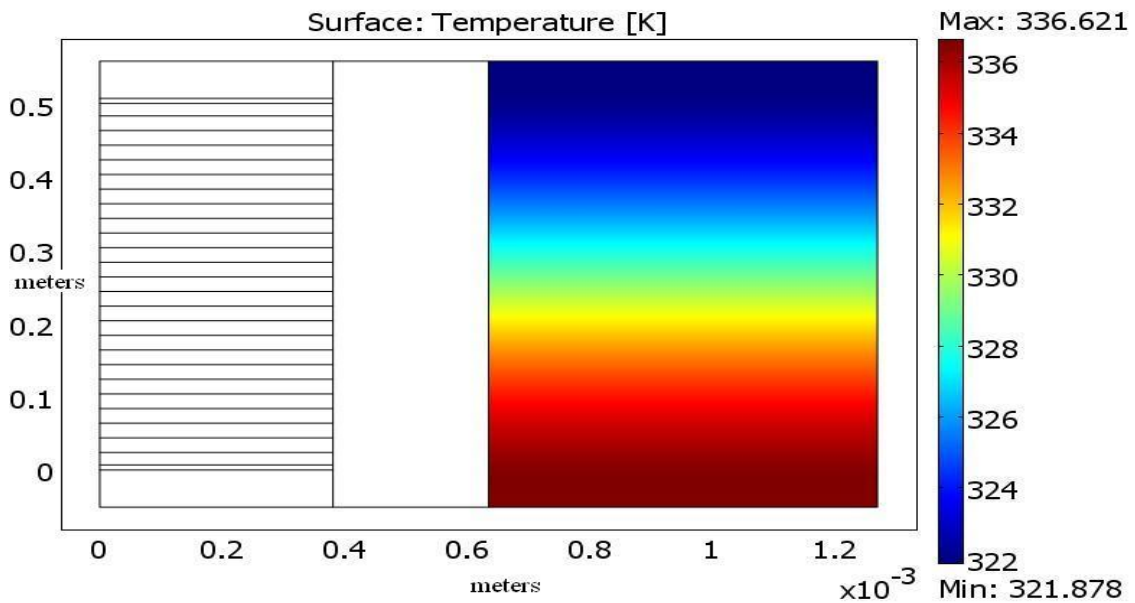
Fig. 36. Coolant varying temperature (HFIR_dist_inactivev1.mph).

The temperature profiles in Figs. 35 and 36 are reproduced as temperature traces for the fuel centerline, fuel/cladding interface, cladding/coolant interface, and for the bulk fluid temperature (center of the coolant channel) in Figs. 37, 38, 39, and 40. The temperature traces for the cladding/coolant interface, and coolant centerline can then be compared to the McLain outcomes shown in Figs. 41 and 42. The coolant flows from right to left in Figs. 37-42.
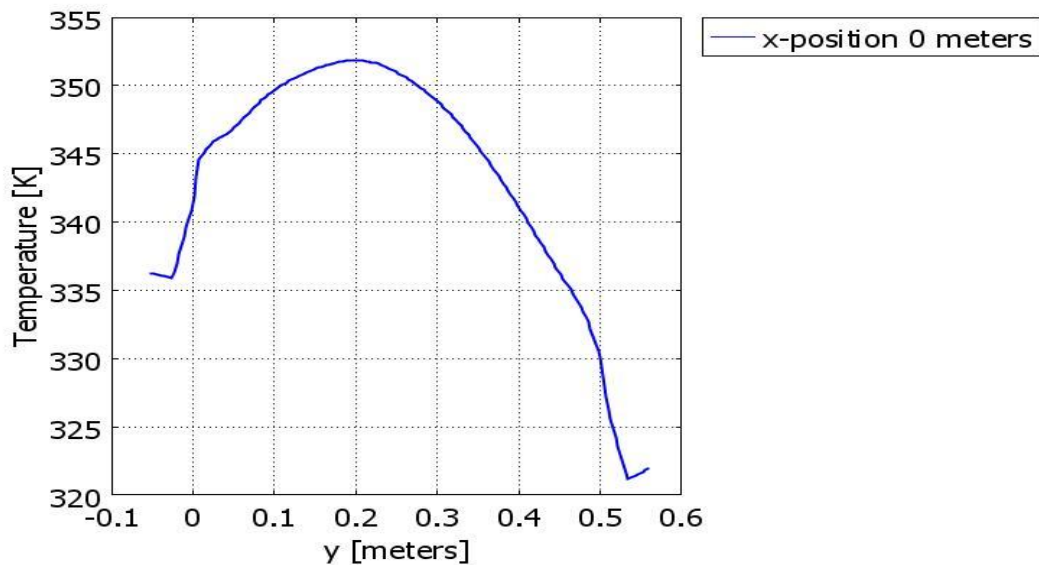
Fig. 37. Centerline temperature profile versus axial position (HFIR_dist_inactivev1.mph).

39
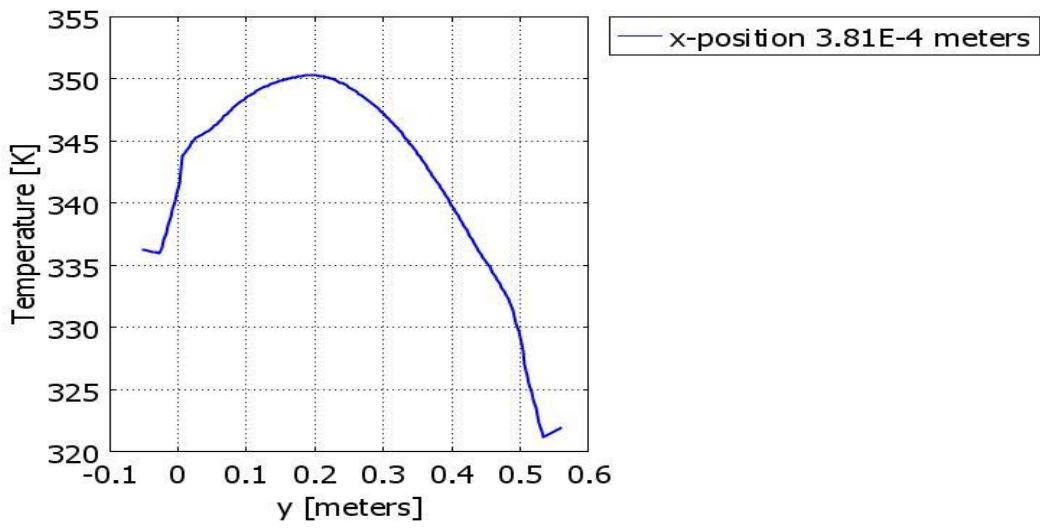
Fig. 38. Temperature profile for fuel and clad interface (HFIR_dist_inactivev1.mph)   h=91314 W/m^2*K.
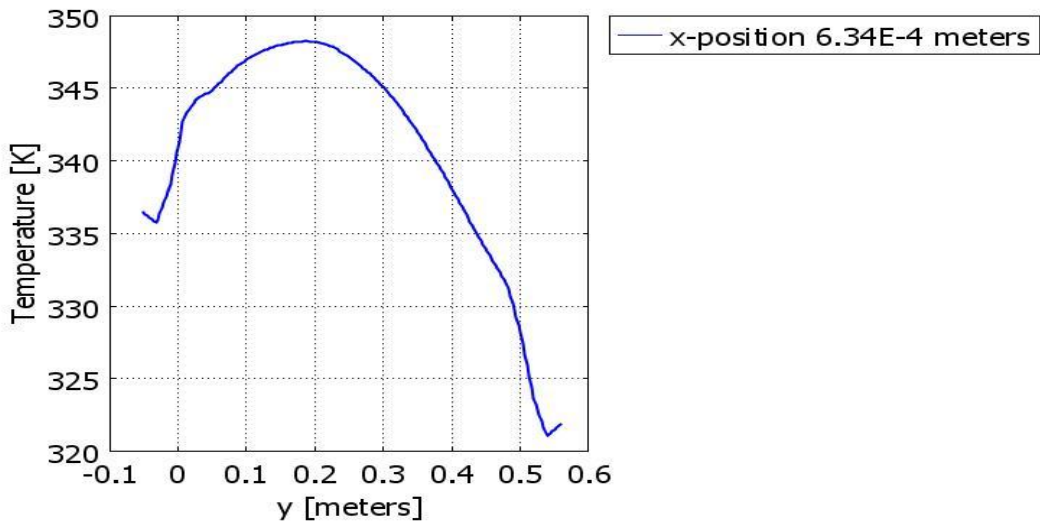
Fig. 39. Cladding surface temperature versus axial position (HFIR_dist_inactivev1.mph)   h=91314 W/m^2*K.
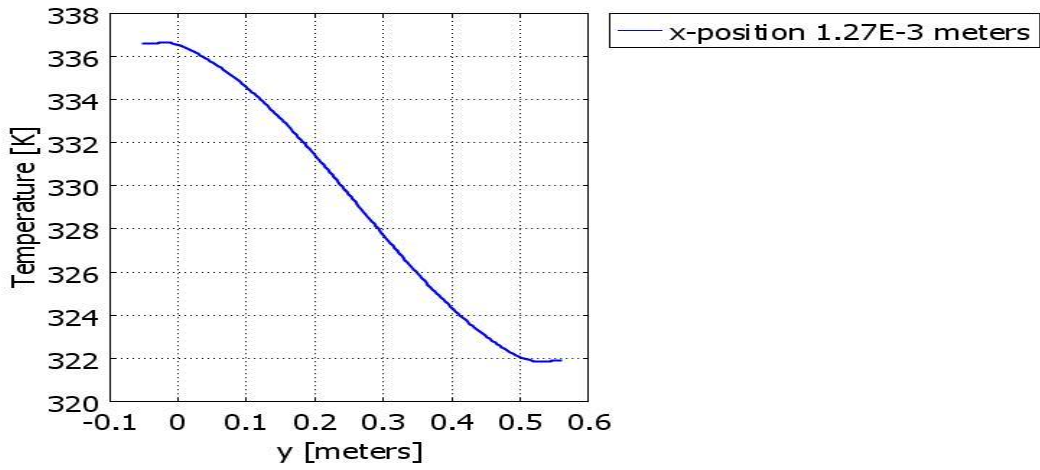
Fig. 40. Bulk fluid temperature versus axial position (HFIR_dist_inactivev1.mph).
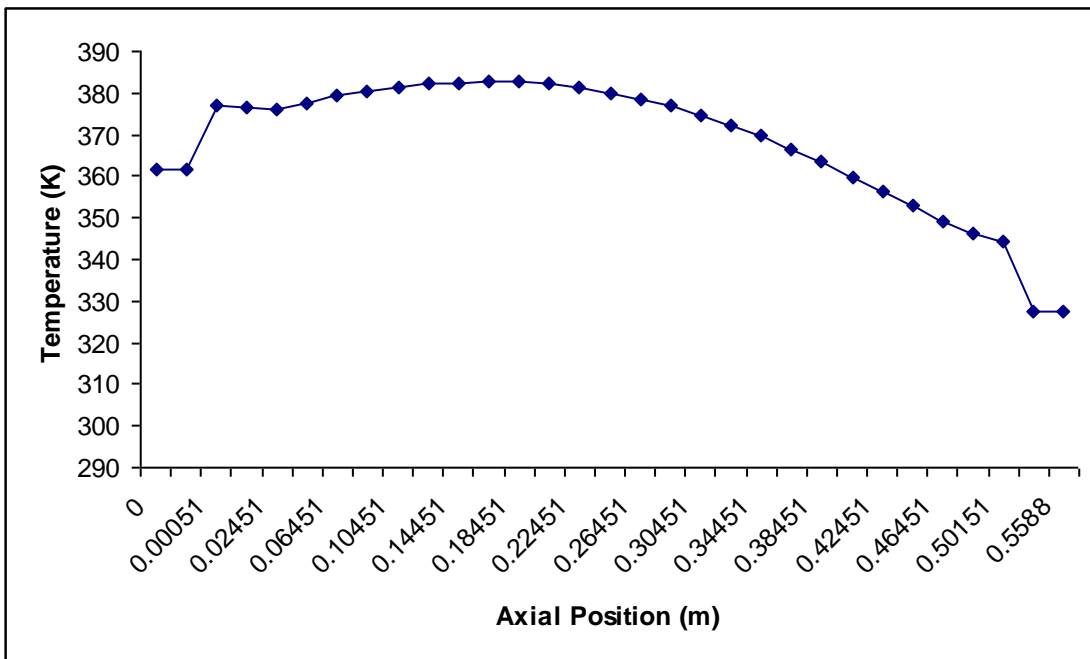
Fig. 41. McLain predicted cladding surface temperature for HEU profile.
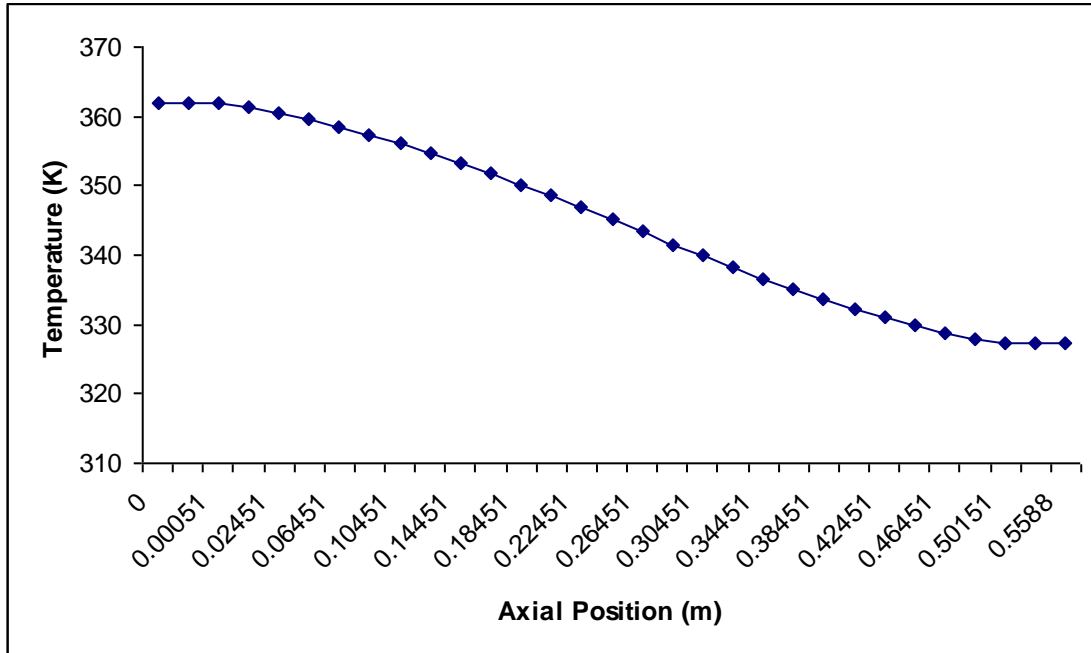
Fig. 42. McLain predicted bulk fluid temperature.

4.3   Conclusions from 2D fuel conduction, 1D flow model

The McLain code predicts cladding surface temperatures that are approximately 25 K higher than what COMSOL predicts and bulk fluid temperatures at the exit of the coolant channel that are 27 K higher than that which COMSOL predicts. The differences may be due to an inconsistency in energy partitioning between the two modeling methods since the heat transfer coefficient used in the COMSOL simulation is chosen close to the modified Hausen model implemented in the McLain code. Note: COMSOL simulations were run at 321.9 K inlet, not 327.6 K. All properties as a result were evaluated at the mean temperature 333.45 K.   The McLain code results are known to be correct because validation is provided by results from reactor operations. COMSOL can also be shown to produce correct results on similar problems as provided by the code documentation with referenceable validation data. Therefore, it must be concluded that there is an inconsistency in the COMSOL setup of the problem. Results presented in section 5.3 provide some resolution of these inconsistencies and insight as to the cause.

5.0 TWO DIMENSIONAL FUEL CONDUCTION WITH TWO DIMENSIONAL TURBULENT FLUID FLOW

Once these initial simulations were investigated, work progressed to the development of a 2-dimensional model of the fuel plate mated to a two dimensional cooling channel including turbulence modeling. The fuel plate and channel are flat for the simulation. Sensitivity studies were conducted to find mesh densities at the fluid/cladding interface that produce accurate and converged temperature and velocity profiles. The computational domains for the 2-dimensional simulation are depicted in Fig. 21. A half fuel plate and half cooling channel are depicted, with the scale in the direction of flow drastically reduced. The boundary conditions for these simulations are depicted in Figs. 43, 44, and 45. The material properties for the coolant in this simulation were taken from the COMSOL library. As a result, the viscosity and density vary with temperature. The variations in properties are examined in some detail later. Flow and power conditions for these simulations are provided in Table 7. Plate power is uniformly distributed for these evaluations to facilitate validation of models.
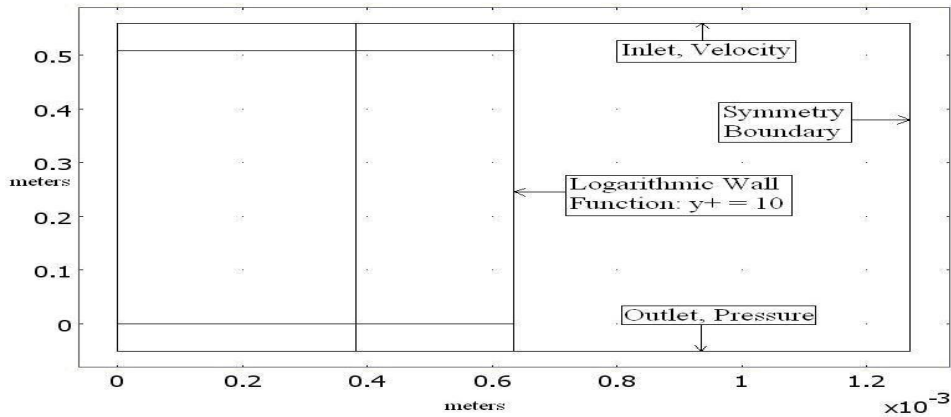
Fig. 43. K-Epsilon boundary condition for $y^+ = 10$.

Table 6. Half fuel and half coolant channel values

Inlet velocity	-15.895	m/s
Inlet temperature	321.9	K
Volumetric heating	2658270879	W/m^3

5.1 Theoretical bases of COMSOL application modes for simulating 2D fuel conduction, 2D flow

The suite of COMSOL application modes employed previously was changed when the simulations began to include turbulence. Found within the Heat Transfer Module and the Fluid-Thermal Interaction sub-folder is a suite of application modes for Turbulent Non-Isothermal Flow, k-ε. This Turbulent Non-Isothermal Flow, k-ε option includes three application modes; k-ε Turbulence Model (chns), General Heat Transfer (htgh), and General Heat Transfer (htgh2).

43
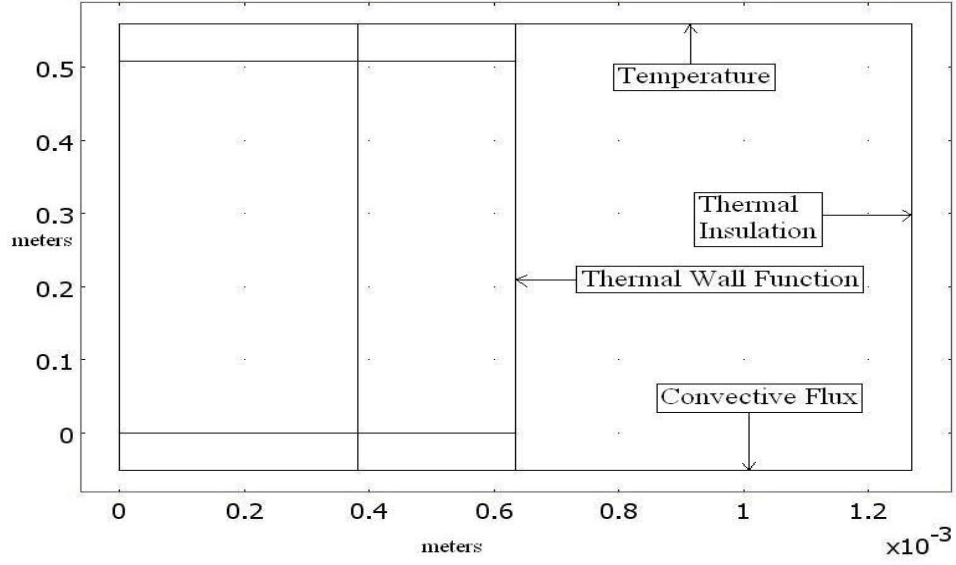
Fig. 44. Fluid heat transfer boundary conditions.
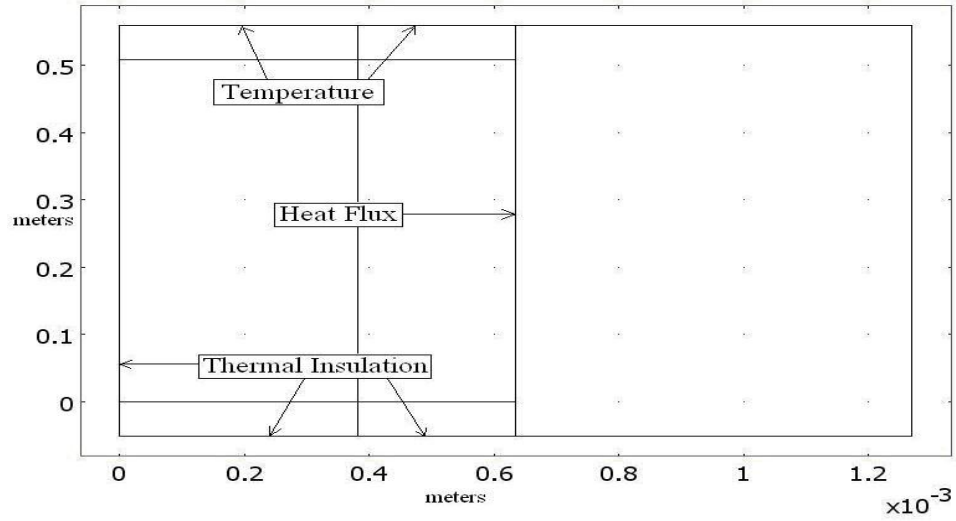
Fig. 45. Fuel plate heat transfer boundary conditions.

The k-ε Turbulence Model employs Equations 69-74 to describe the coolant flow.

$$\rho\mathbf{u}\bullet\nabla\mathbf{u}=\nabla\bullet\left[-p\mathbf{I}+\left(\eta+\eta_T\right)\left(\nabla\mathbf{u}+\left(\nabla\mathbf{u}\right)^T-\left(\frac{2}{3}\right)\left(\nabla\bullet\mathbf{u}\right)\mathbf{I}\right)-\left(\frac{2}{3}\right)\rho k_{TKE}\mathbf{I}\right]+\mathbf{F} \qquad \text{Eq. 69}$$

$$\nabla\bullet\left(\rho\mathbf{u}\right)=0 \qquad\qquad \text{Eq. 70}$$

$$\rho\mathbf{u}\bullet\nabla k_{TKE}=\nabla\bullet\left[\left(\eta+\frac{\eta_T}{\sigma_k}\right)\nabla k_{TKE}\right]+\eta_T P(\mathbf{u})-\left(\frac{2\rho k_{TKE}}{3}\right)\nabla\bullet\mathbf{u}-\rho\varepsilon \qquad \text{Eq. 71}$$

44

$$\rho \mathbf{u} \bullet \nabla \varepsilon = \nabla \bullet \left[\left(\eta + \frac{\eta_T}{\sigma_\varepsilon} \right) \nabla \varepsilon \right] + \left(\frac{C_{\varepsilon 1} \varepsilon}{k_{TKE}} \right) \left[\eta_T P(\mathbf{u}) - \left(\frac{2 \rho k_{TKE}}{3} \right) \nabla \bullet \mathbf{u} \right] - \frac{C_{\varepsilon 2} \rho \varepsilon^2}{k_{TKE}} \qquad \text{Eq. 72}$$

$$P(\mathbf{u}) = \nabla \mathbf{u} : \left(\nabla \mathbf{u} + (\nabla \mathbf{u})^T \right) - \left(\frac{2}{3} \right) (\nabla \bullet \mathbf{u})^2 \qquad \text{Eq. 73}$$

$$\eta_T = \frac{\rho C_\mu k^2}{\varepsilon} \qquad \text{Eq. 74}$$

where k_{TKE} is the turbulent kinetic energy.

The General Heat Transfer (htgh) employs Equations 75 to describe the heat transfer in the coolant.

$$\nabla \bullet \left(-(k + k_T) \nabla Tf \right) = Q - \rho C_p \mathbf{u} \bullet \nabla Tf \qquad \text{Eq. 75}$$

where, $(k + k_T)$ are the molecular and turbulent conductivity in the coolant, Q is the power, and $\rho C_p \mathbf{u} \nabla Tf$ are the terms that govern the convective heat transfer in the coolant.

The General Heat Transfer (htgh2) employs Equations 76 to describe the heat transfer in the fuel plate.

$$\nabla \bullet \left(-k \nabla Ts \right) = Q \qquad \text{Eq. 76}$$

The coolant inlet velocity is prescribed by Equations 77, 78, and 79.

$$\mathbf{u} = \mathbf{u}_0 \qquad \text{Eq. 77}$$

$$k_{TKE} = \left(\frac{3 I_T^2}{2} \right) (\mathbf{u}_0 \bullet \mathbf{u}_0) \qquad \text{Eq. 78}$$

$$\varepsilon = C_\mu^{0.75} \left(\left(\frac{3 I_T^2}{2} \right) (\mathbf{u}_0 \bullet \mathbf{u}_0) \right)^{1.5} \Bigg/ L_T \qquad \text{Eq. 79}$$

where, C_μ is a constant equal to 0.09.

The logarithmic wall function is prescribed by Equation 80, 81, 82, and 83.

$$\mathbf{n} \bullet \mathbf{u} = 0 \qquad \text{Eq. 80}$$

$$\left[(\eta + \eta_T) \left(\nabla \mathbf{u} + (\nabla \mathbf{u})^T - \left(\frac{2}{3} \right) (\nabla \bullet \mathbf{u}) \mathbf{I} \right) \right] \mathbf{n} = \left[\rho C_\mu^{0.25} k^{0.5} \Big/ \left(\ln(\delta_w^+) / \kappa + C^+ \right) \right] \mathbf{u} \qquad \text{Eq. 81}$$

$$\mathbf{n} \bullet \nabla k = 0 \qquad \text{Eq. 82}$$

$$\varepsilon = \frac{\rho C_{\mu} k^2}{\left(\kappa \delta_w^{+} \eta\right)}$$

Eq. 83

The symmetry boundary is prescribed by,

$$\mathbf{t} \bullet \left[-p\mathbf{I} + \left(\eta + \eta_T\right)\left(\nabla \mathbf{u} + \left(\nabla \mathbf{u}\right)^T - \left(\frac{2}{3}\right)\left(\nabla \bullet \mathbf{u}\right)\mathbf{I}\right)\right]\mathbf{n} = 0$$

Eq. 84

$$\mathbf{n} \bullet \left[\left(\eta + \eta_T / \sigma_k\right)\nabla k - \rho \mathbf{u} k\right] = 0$$

Eq. 85

$$\mathbf{n} \bullet \left[\left(\eta + \eta_T / \sigma_\varepsilon\right)\nabla \varepsilon - \rho \mathbf{u} \varepsilon\right] = 0$$

Eq. 86

The outlet pressure is defined by,

$$\mathbf{n} \bullet \nabla \varepsilon = 0$$

Eq. 87

$$\left[\left(\eta + \eta_T\right)\left(\nabla \mathbf{u} + \left(\nabla \mathbf{u}\right)^T - \left(\frac{2}{3}\right)\left(\nabla \bullet \mathbf{u}\right)\mathbf{I}\right)\right]\mathbf{n} = 0$$

Eq. 88

The convective flux boundary condition is prescribed by,

$$\mathbf{n} \bullet \left(-k\nabla Tf\right) = 0$$

Eq. 89

The thermal insulation boundary condition is prescribed by,

$$-\mathbf{n} \bullet \left(-k\nabla Tf + \rho C_p \mathbf{u} Tf\right) = 0$$

Eq. 90

The thermal wall function is prescribed by,

$$-\mathbf{n} \bullet \left(-k\nabla Tf + \rho C_p \mathbf{u} Tf\right) = q_0$$

Eq. 91

The heat flux boundary condition is prescribed by,

$$-\mathbf{n} \bullet \left(-k\nabla Ts\right) = q_0 + h\left(T_{\text{inf}} - Ts\right)$$

Eq. 92

The temperature boundary condition is prescribed by,

$$Ts = Ts_0$$

Eq. 93

The thermal insulation boundary condition is prescribed by,

$$-\mathbf{n} \bullet \left(-k\nabla Ts\right) = 0$$

Eq. 94

Boundary layer modeling in the computational fluid dynamics domain often uses a form of the law of the wall to reduce mesh demands at the wall to fluid interface. The turbulence is suppressed near the wall, leading to increased importance of molecular viscosity and conductivity values. In the case of HFIR core cooling, the near wall temperature variations are quite large due to the high thermal flux, so the near wall region should be modeled to allow proper simulation of near wall thermo-physical property variation, and attendant influence on velocity and temperature gradients. One scale parameter for mesh selection near the wall is the normalized wall dimension, y^+, defined as,

$$y^+ = \frac{y\sqrt{\tau/\rho}}{\upsilon}$$

Eq. 95

where τ is the wall shear stress (783.4635 kg/(ms^2)), ρ is the fluid bulk density (982.91 kg/m^3), y is the dimension normal to the cladding surface, extending into the coolant, in meters, and ν is the kinematic viscosity of the fluid [4.7223(10^{-7}) m^2/s], all taken at a temperature of 333.45 K.

The wall shear, τ, was defined from an integral channel momentum balance as shown in Fig. 46, to first order, as,

$$\tau = \frac{(P1 - P2)A_{xs}}{A_{wet}}$$

Eq. 96

where P1 is the pressure at the inlet, P2 is the pressure at the exit, A_{xs} is the cross sectional area of the coolant channel, and A_{wet} is the wetted area of the cladding. The pressure difference between the inlet and exit was taken as 7.52125(10^5) Pa, typical from operational experience. The cross sectional area is 0.000635 m^2 and the wetted area is 0.6096 m^2.
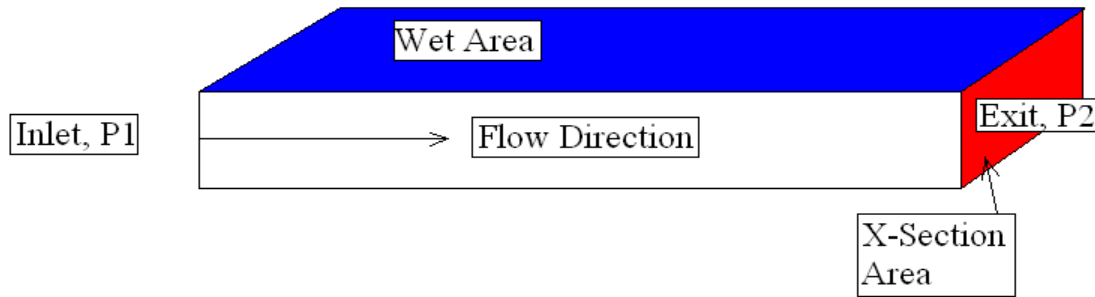
Fig. 46. Flow diagram used for force balance.

5.2 Results of COMSOL simulations

The COMSOL GUI allows y^+ be set equal to 10 to constrain near wall meshing. The value for y at y^+ equal 10 is 5.289(10^{-6}) m using Equation 95. The actual value used in the construction of the boundary layer mesh was 5.35(10^{-6}) m. Figure 46 depicts the mesh used for a solution to the full axial channel simulation with a y^+ value of 10.
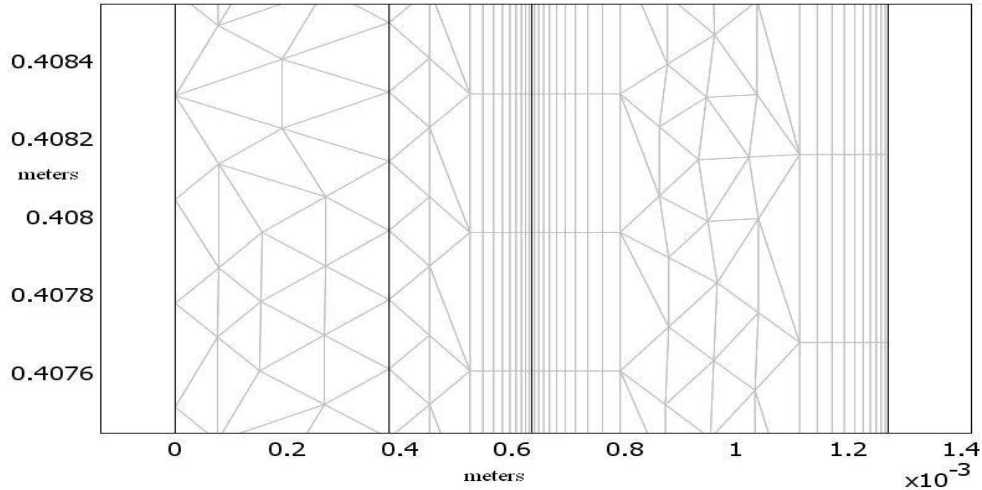
Fig. 47. Mesh for $y^+ = 10$ (kepsitest12.mph).

5.2.1 Uniform power distribution

The temperature distribution for a uniform, constant power distribution is shown in Fig. 48 generated with the mesh shown Fig. 47.   It is important to note that the mesh density shown in Fig. 47 is to scale, but only one millimeter of the total 0.6096 meter fuel plate height is shown.
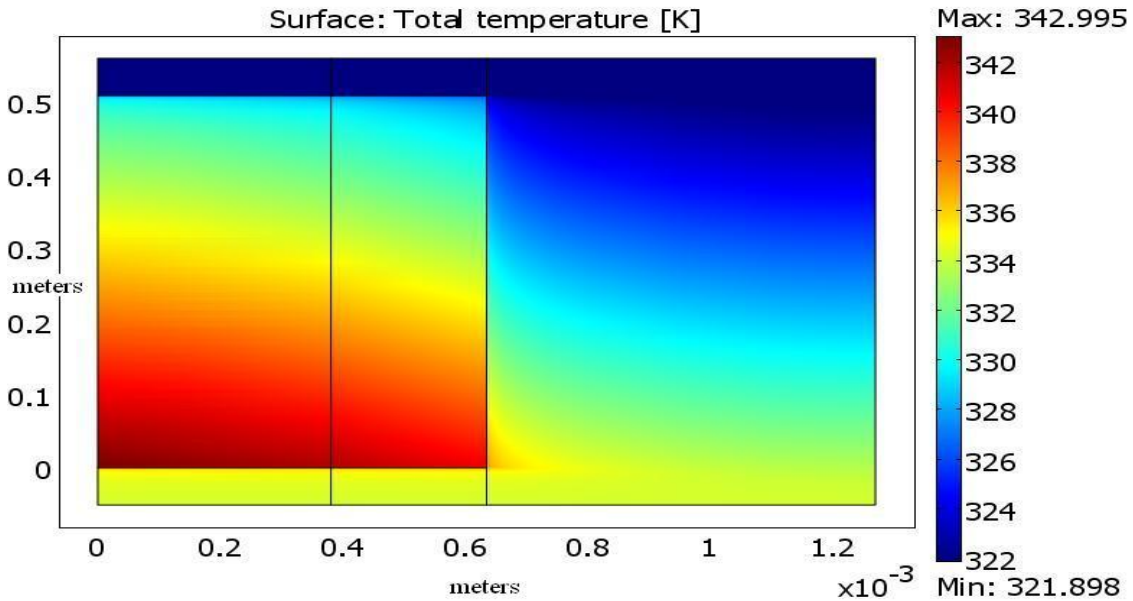
Fig. 48. Temperature distribution (kepsitest12v1.mph).

The HFIR cooling model in use in the current core thermal model is due to Hausen, later modified by Thomas, as documented in the HFIR Safety Analysis Report. The modified Hausen model, with no thermal property variations, predicts an exit wall temperature near 356.3 K, and the widely used Dittus-Boelter correlation predicts 358.5 K. Figure 49 depicts the temperature profiles at the near entrance, mid channel, and near exit regions of the simulation. The exit wall temperature is near 340 K in the simulation outcome. Note the temperature profile in the coolant near the wall is quite steep.

48
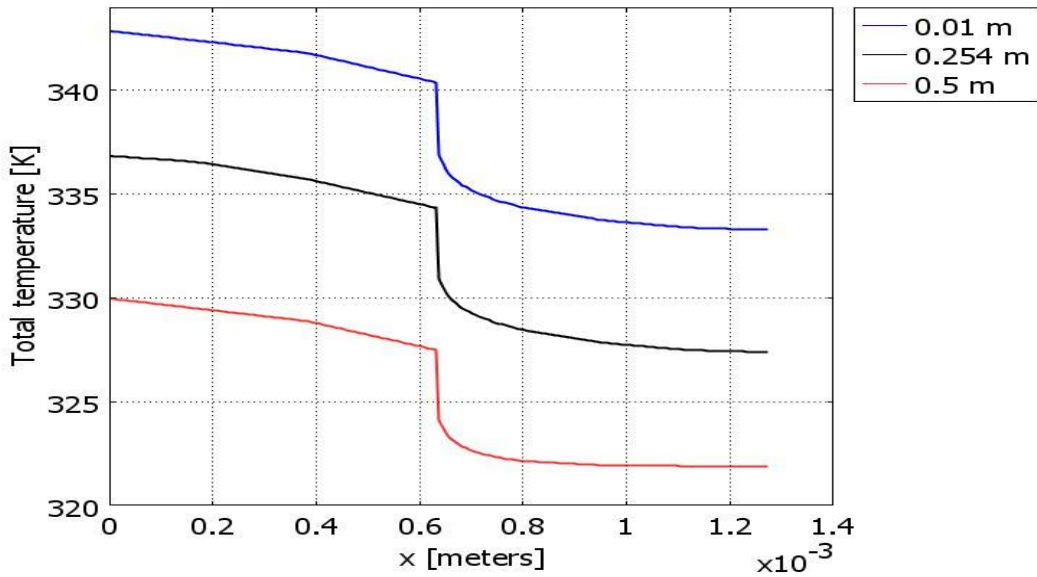
Fig. 49. Temperature profile (kepsitest12v1.mph).

Fig. 50 depicts the fluid density variation due to temperature variation with position.
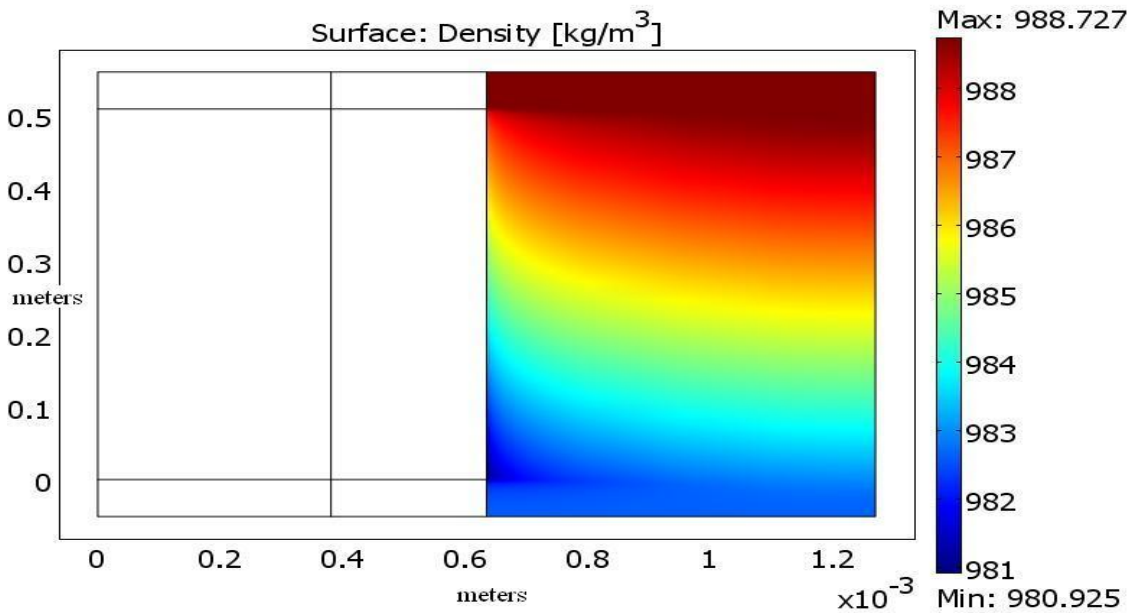
Fig. 50. Temperature dependent density (kepsitest12v1.mph).

The classical turbulence modeling employed here adds to the fluid effective viscosity. The turbulence is suppressed near the wall, with the effective viscosity declining to the molecular value. The progression of effective viscosity in the cooling channel cross-section is shown in Fig. 51.
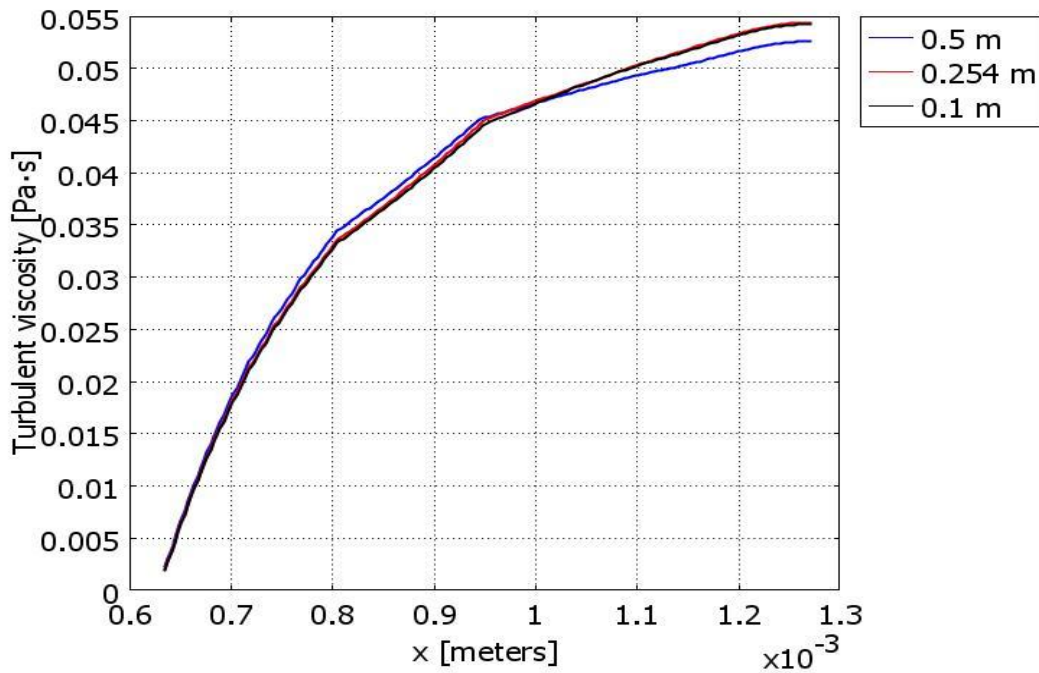
Fig. 51. Turbulent viscosity (kepsitest12v1.mph).

The legend in Fig. 51 depicts the axial position in the coolant channel for the viscosity profile, with 0.5 meters near the coolant inlet. The eddy diffusivity in the flow due to turbulence also leads to enhancement of the fluid effective conductivity. The value for the turbulent thermal conductivity, λ, is defined as,

$$\lambda = \frac{c_p \upsilon}{\mathrm{Pr}_t}$$

Eq. 97

where c_p is the specific heat of the coolant, υ is the turbulent viscosity, and Pr_t is the turbulent Prandtl number, here taken as unity. Figure 52 shows the effective fluid conductivity attributable to flow turbulence. Note that flow conductivity values range near those for the fuel clad, Aluminum 6061, taken as 181.3 W/(m*K).

50
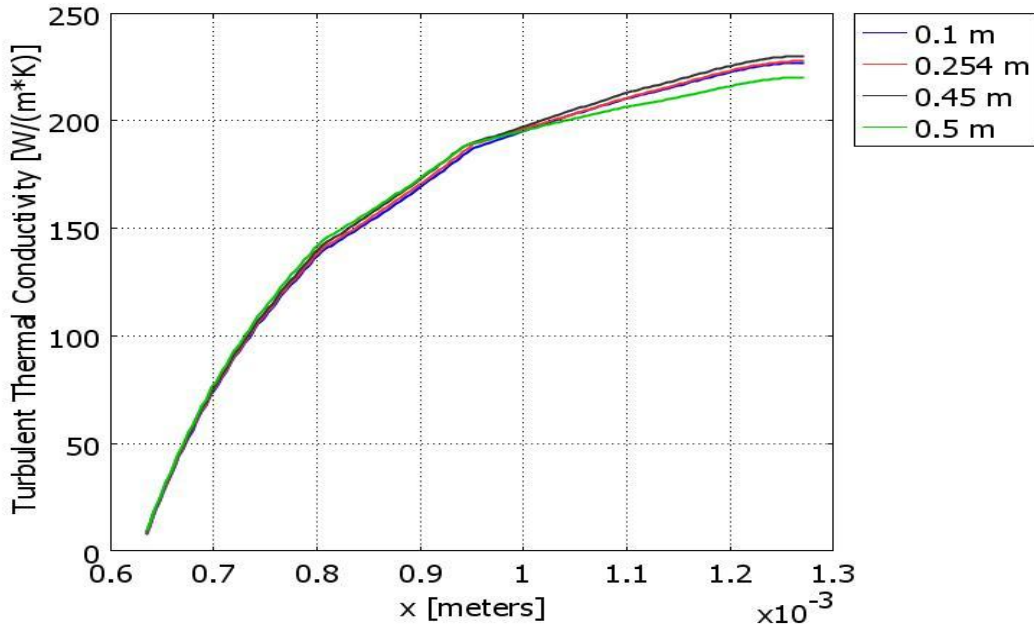
Fig. 52. Turbulent thermal conductivity (kepsitest12.mph).

The turbulent conductivity values are consistent with those developed for lateral conduction in the HFIR fuel cooling channel from simulations performed by Ruggles in 1997, using models from Hatton and Quarmby, 1963. This offers another indirect validation of the fidelity of the COMSOL two-dimensional fluid simulation.

5.2.2 Localized hot spot in power distribution

In order to examine COMSOL's abilities to correctly model small perturbations in fuel loading, a 0.008m thick region with higher volumetric heating was placed at the center of the fueled region. This region's volumetric heating is increased by 20 percent over the surrounding regions. The volumetric heating in the increased region is $3.189925055(10^9)$ W/m^3. The basic model from Fig. 21 is modified for this simulation as shown in Fig. 53. The mesh for this model is shown in Fig. 54.
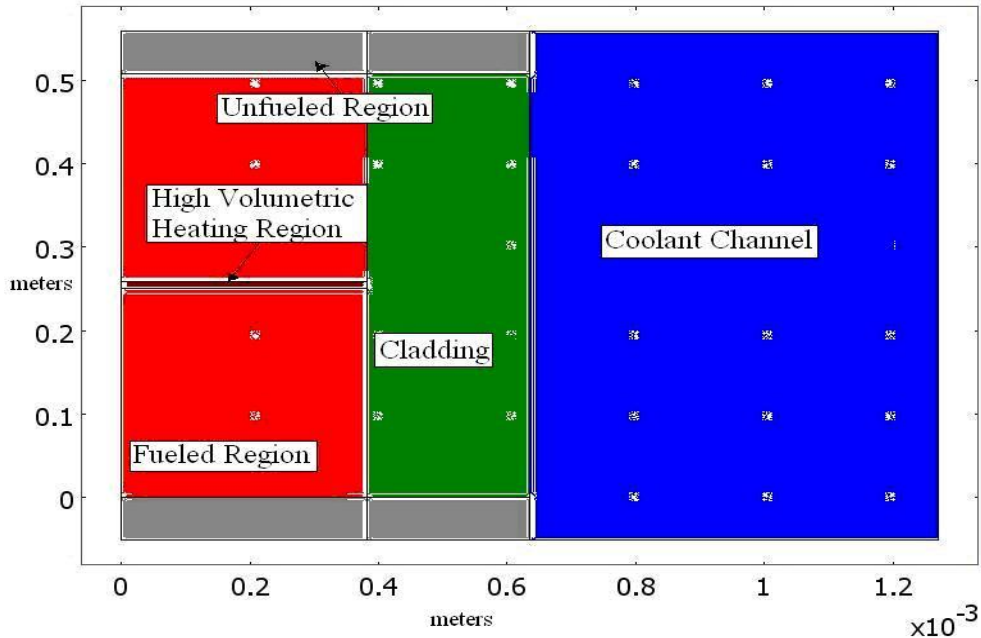
Fig. 53. Increased volumetric heating region (kepsitest10v1.mph).

Figure 55 shows the temperature profile for the model with the increased volumetric heating region. The temperature profile across the wetted surface of the "hot spot" is depicted in Fig. 56. This is the temperature profile of the fluid at the coolant/cladding interface (0.000635m) between y=0.248 m and y=0.261 m. Recall the flow is downward, so the fluid first encounters elevated flux near 0.258 m, with evidence of the hot spot diminished to near zero at 0.249 m. The beginning of the profile is as expected; with boundary layer growth leading to locally elevated heat transfer at the leading edge of the perturbation.

There is a difference in performance of the un-fueled inlet relative to the un-fueled outlet. The inlet is observed to follow the coolant inlet temperature, while the outlet un-fueled region has a more gradual temperature gradient.
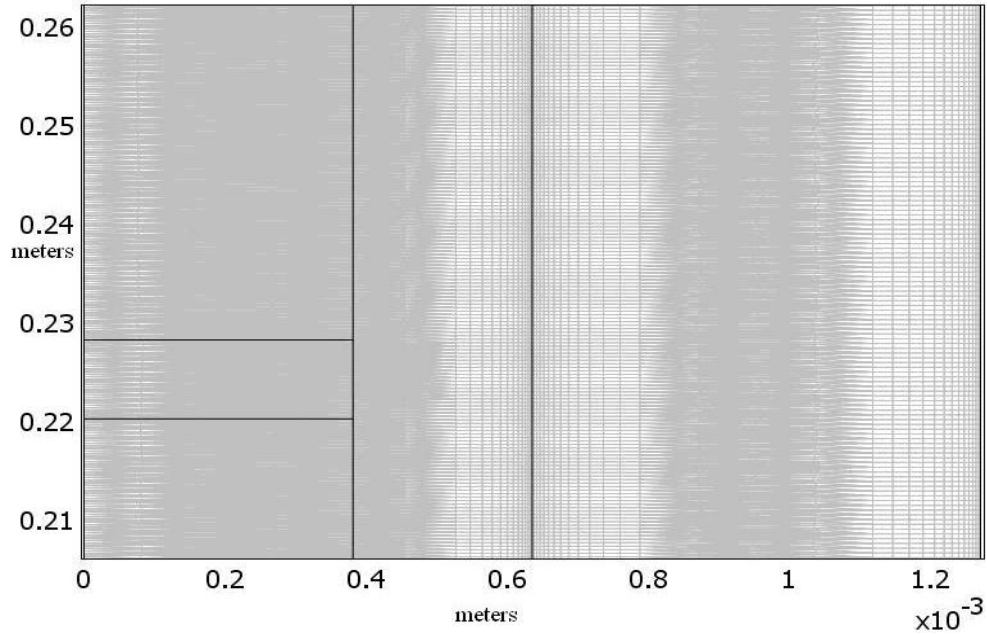
Fig. 54. Mesh for the 20% increased volumetric heating hotspot (kepsitest10v1.mph).
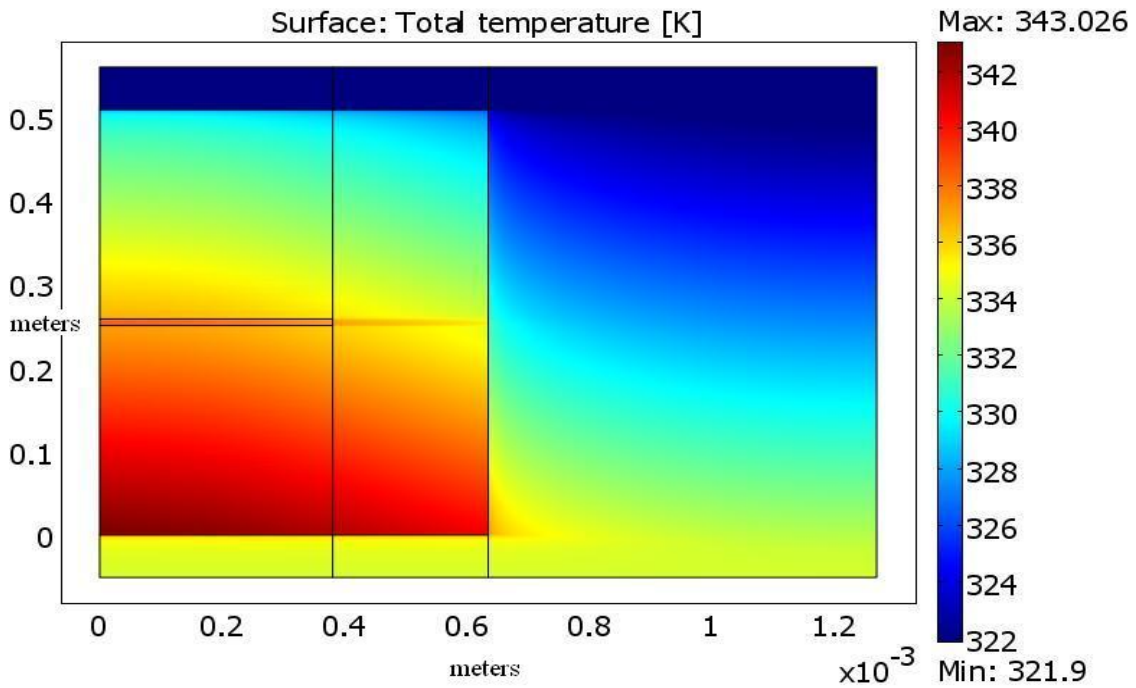
Fig. 55. Temperature profile (kepsitest10v1.mph).
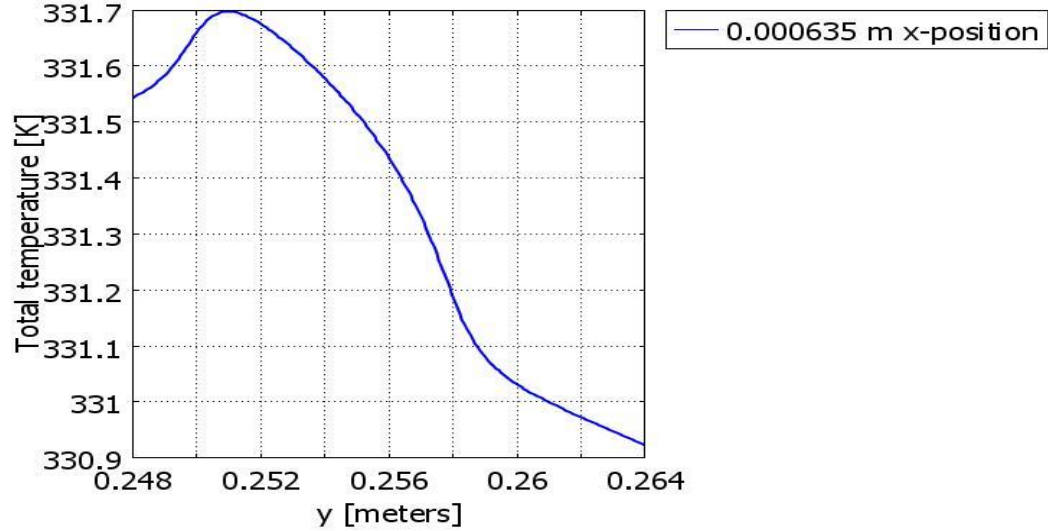
Fig. 56. Temperature profile (kepsitest10v1.mph).

When the constant property and constant volumetric heating rate model is run, the surface heat transfer coefficient between the clad and coolant is constant, leading to constant difference between the coolant bulk temperature and clad surface temperature. The difference between the fuel centerline temperature and the coolant bulk temperature is also constant for such simulations. The axial conduction in the fuel plate is small relative to through plate conduction since the temperature gradient along the plate is of order 50 degrees C per meter, while the through plate temperature gradient is of order 15,000 degrees C per meter. When the fueled region of the fuel plate ends, the energy propagated due to axial conduction is quickly moved into the coolant, so the leading unfueled end of the fuel plate follows the inlet coolant temperature up to a few millimeters of the fueled region. The trailing unfueled end of the fuel plate also closely follows the coolant temperature, but there is more evidence of axial temperature variation in the trailing edge of the fuel plate. This is not because of chosen boundary conditions.

The system is thermally symmetric axially except for the temperature profile in the coolant. The coolant flow enters the channel at uniform temperature, but it leaves the fueled region with a temperature profile. The temperature profile relaxes as the coolant moves past the unfueled exit portion of the plate. This behavior is shown in Fig. 57, with the first trace at x=0, which is just at the end of the fueled region of the plate.

Fig. 57. Coolant temperature profile relaxation in unfueled exit region (kepsitest10v1.mph).

The relaxation of the temperature profile in the coolant influences the temperature and flux at the clad to coolant interface in the exit unfueled region.

5.2.3 Simulation of a proposed LEU fuel

A representative axial power profile for hot channel at beginning-of-life (BOL) for the proposed HFIR LEU core design was provided by Primm and is included in Appendix C. This power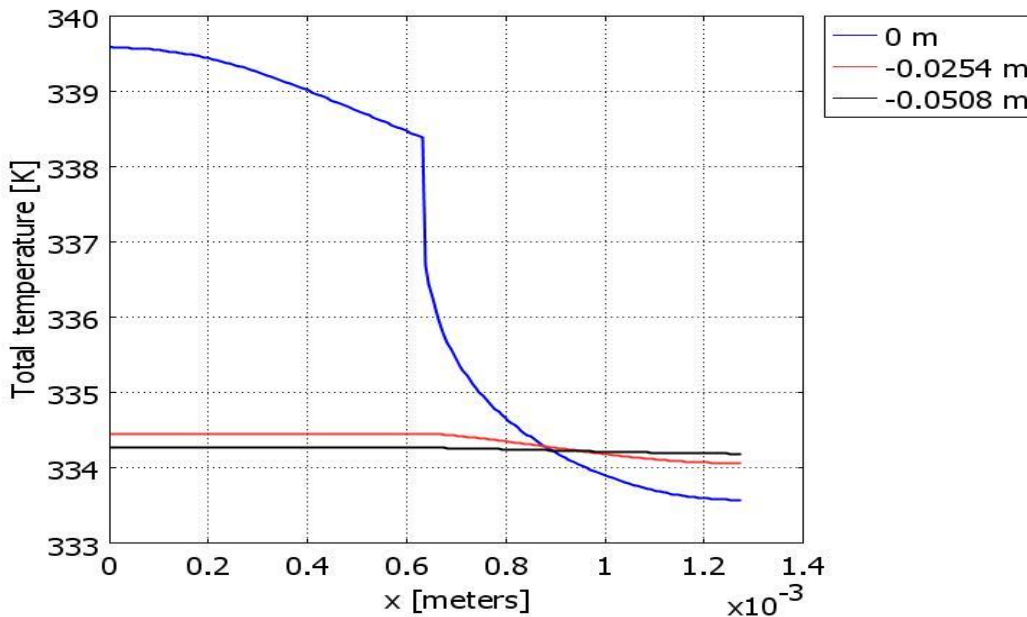 profile is implemented in the files PowerProfile.mph. The power profile assumes the same fuel conductivity values as were used in the prior, high enriched uranium (HEU) fuel simulations. This was done because the current work is being validated by comparison to the McLain code and the McLain code incorporated fuel conductivity values into the FORTRAN coding. Thus modeling of LEU fuel with the McLain code would require rewriting the code. Indeed, this condition is one of several factors considered in migrating from the current methodology (the McLain steady state heat transfer code [SSHTC]) to the new COMSOL-based methodology.

The power profile was implemented in the fuel meat by first creating 19 sub-domains congruent with the information that was provided in the file ANSpaperData.txt. Each sub-domain corresponds to a new local power density. It is assumed that of the 85 MW deposited in the core, only 80.7 MW is deposited in the fuel. The model PowerProfile.mph was simulated using a boundary condition wall offset equal 10. The boundary conditions for the thermal modeling of the fuel plate and coolant are displayed in Figs. 59-60. The boundary conditions for the k-ε modeling as it pertains to PowerProfile.mph are displayed in Fig. 61. The mesh used for the PowerProfile.mph simulation is displayed in Fig. 62. The value for y at y^+ equal 10 is $5.289(10^{-6})$. The actual value used in the construction of the boundary layer mesh was $5.35(10^{-6})$ m. The 19 individual sub-domains for the fuel meat to allow power profile representation are shown in Fig. 63, with the actual power profile illustrated in Fig. 58. Figure 63 also displays the temperature profile for the $y^+=10$ simulation.

Axial Distribution (m)
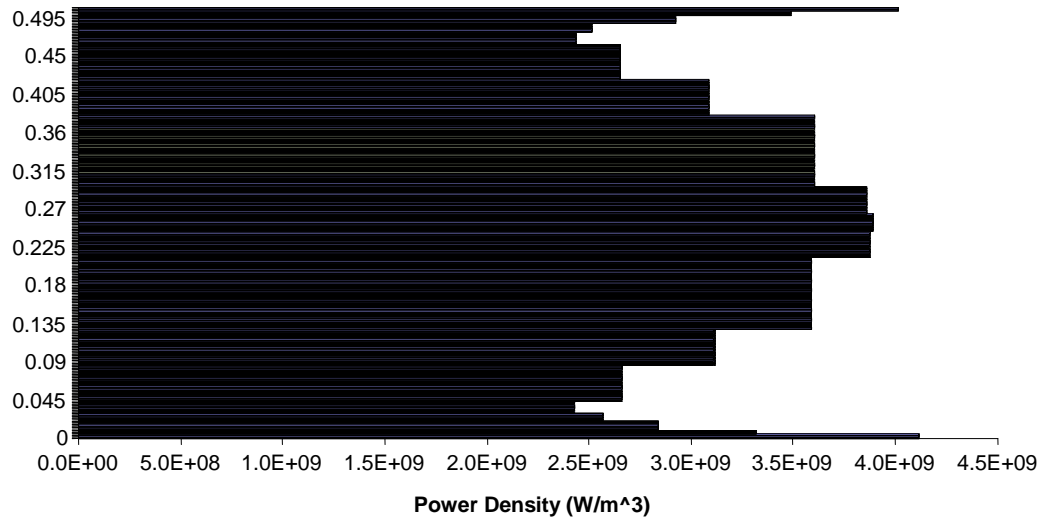
Power Density (W/m^3)

Fig. 58. Power density variation (PowerProfile.mph).
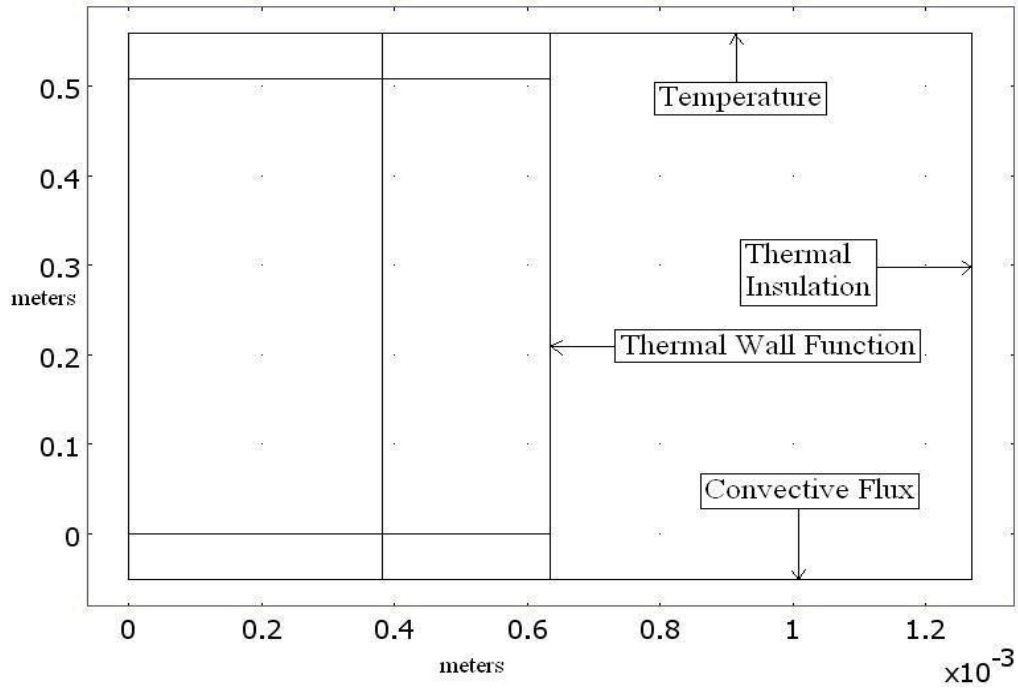
Fig. 59. Fluid heat transfer boundary conditions.

56
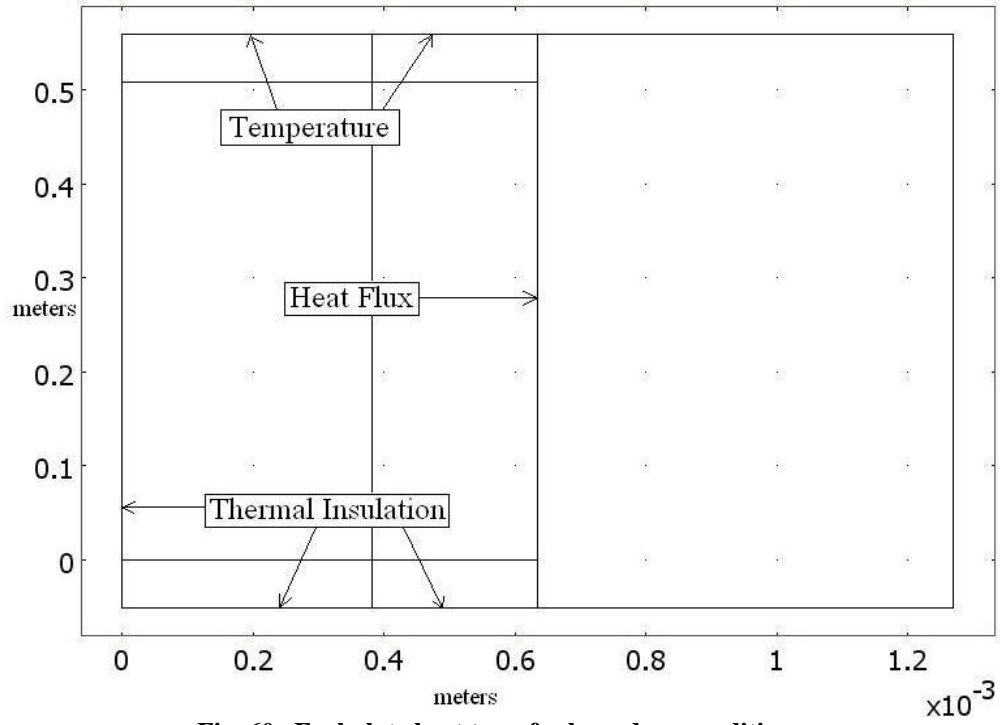
Fig. 60. Fuel plate heat transfer boundary conditions.
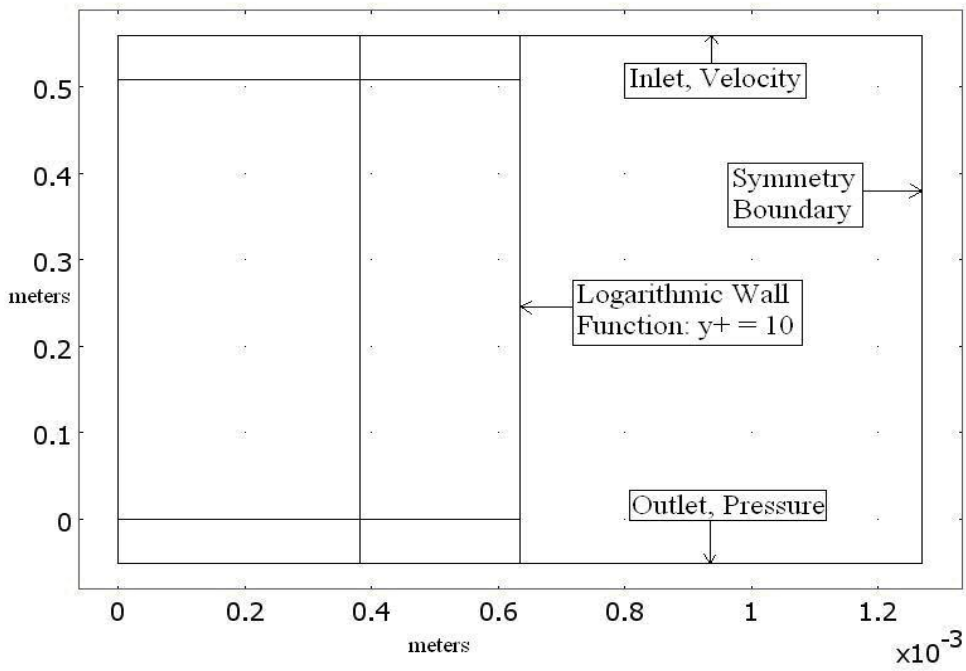
Fig. 61. K-Epsilon boundary condition for y$^+$ = 10.
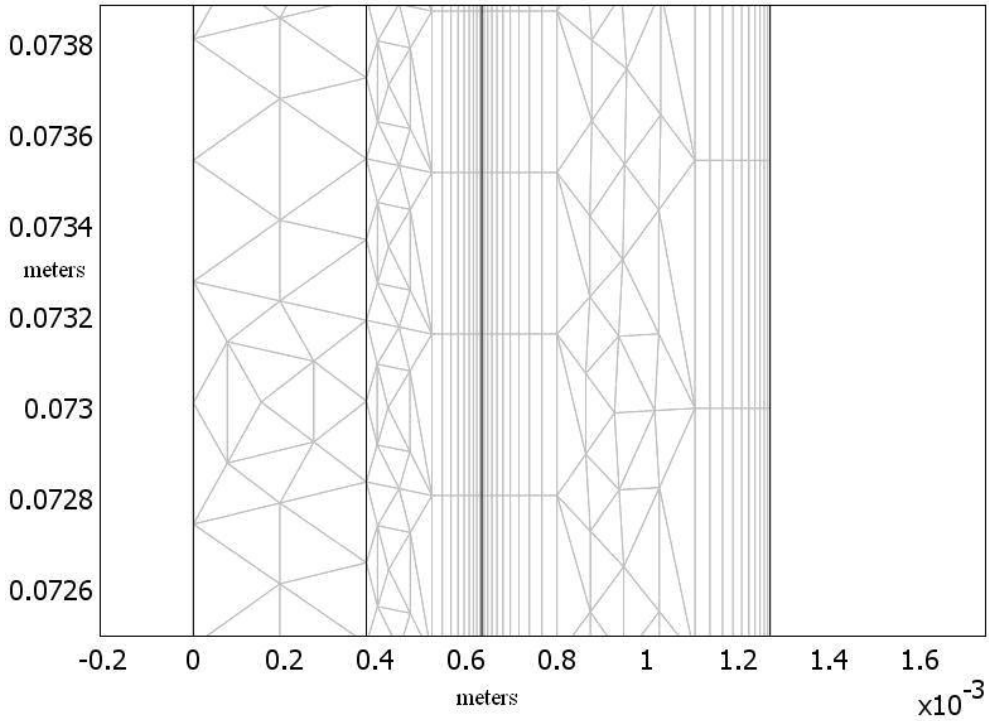
Fig. 62. Mesh representation.
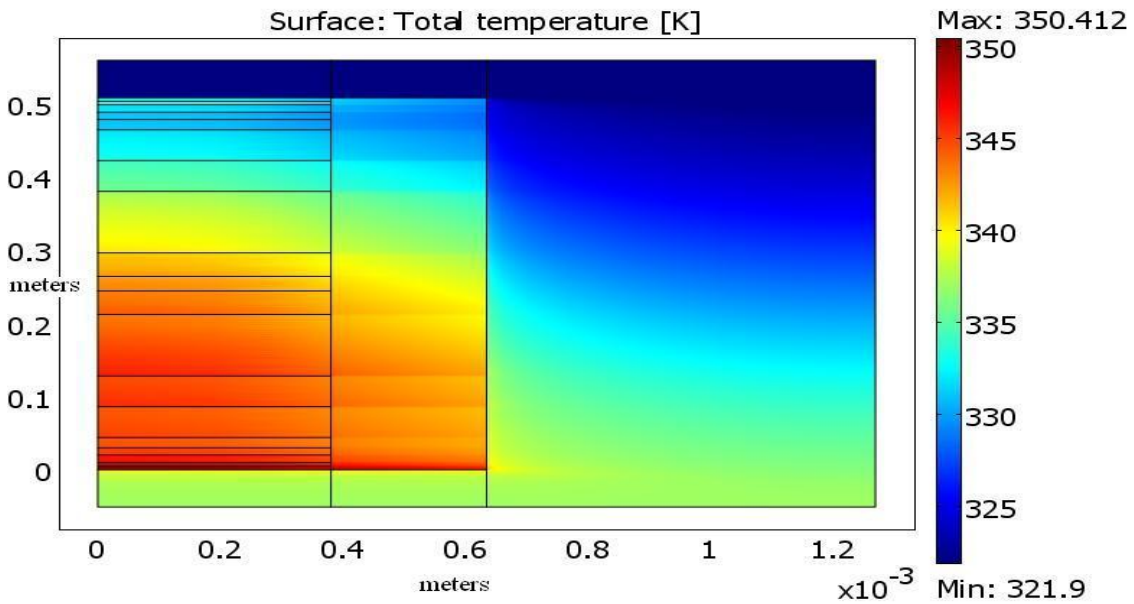
Fig. 63. Temperature profile (PowerProfilev1.mph).

Upon initial inspection of the rendered output in Fig. 63 it appears that there are distinct "thermal layers" in the cladding. Apparently, COMSOL is having some difficulties simulating the axial conduction in the cladding at this mesh density. However, when the image is scaled to its actual dimensions and a close inspection of these regions is performed, the thermal layers are less exaggerated, as shown in Fig. 64.

58
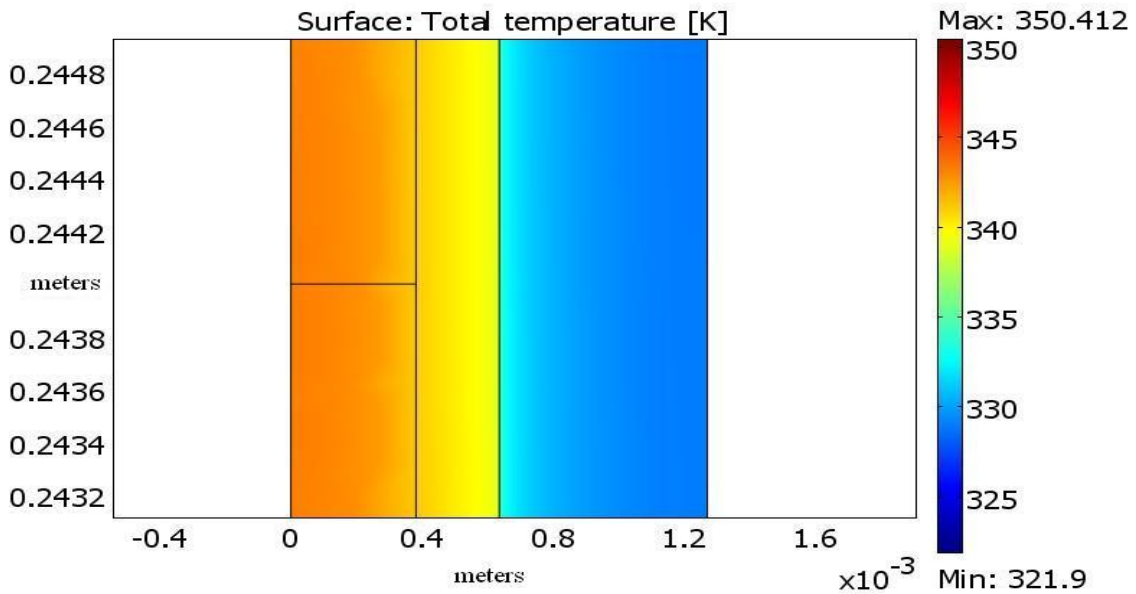
Fig. 64. Enhanced temperature profile (PowerProfilev1.mph).

The COMSOL generated temperature profile for the fuel centerline is displayed in Fig. 65.
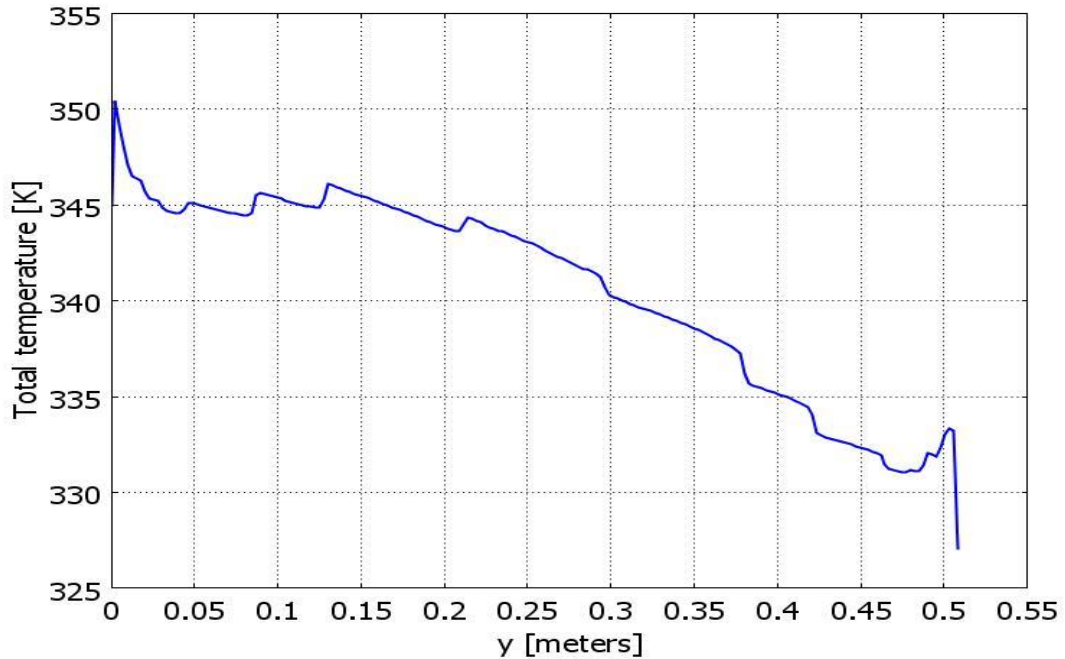
Fig. 65. Temperature profile for fuel centerline (PowerProfilev1.mph).

59

The larger perturbations in the temperature line on Fig. 65 correspond to changing power density regions, but some roughness in the profile is due to the coarseness of the mesh employed. Figure 66 shows the temperature profile at the clad/coolant interface.
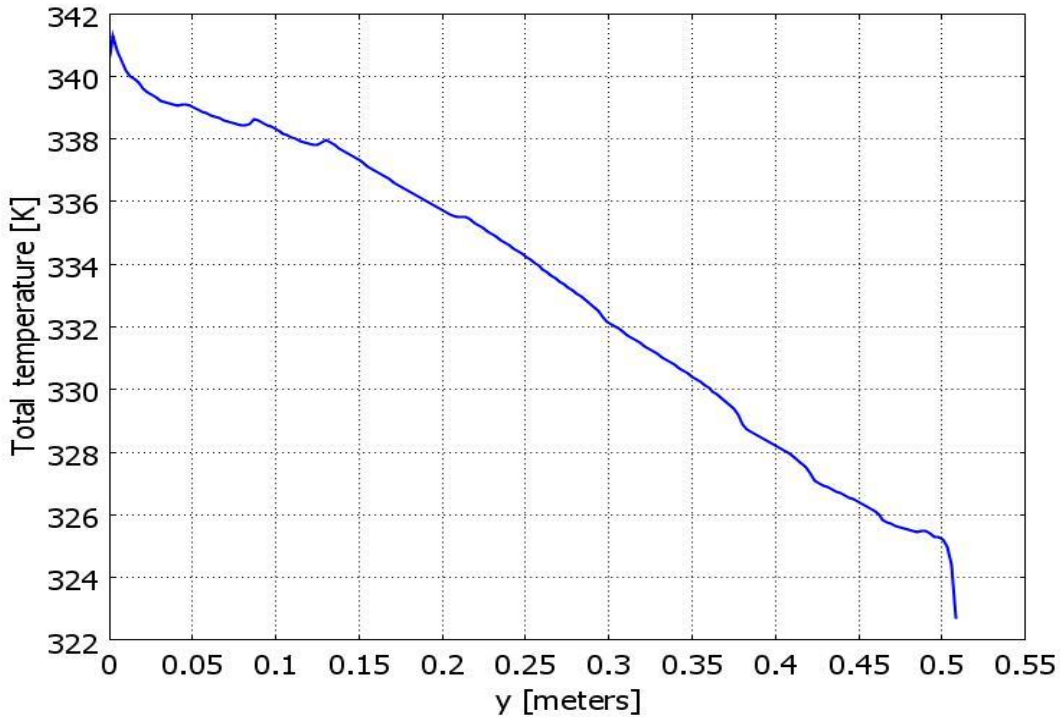
Fig. 66. Temperature profile at the clad/coolant interface (PowerProfilev1.mph).

The convex increases in the temperature curve correspond to newly developing thermal boundary layers as the fluid enters a region of higher thermal flux. The concave portions of the line are indications that the coolant is entering regions of lower thermal flux. The combined action of boundary layer development and conduction in the fuel cause these transitions. The hot spot simulation developed earlier in the project exhibited similar behavior.

A comparison between the COMSOL predicted outcomes for the wall temperature and Dittus Boelter and revised Modified Hausen predicted outcomes for the wall temperature was conducted at the axial position, y = 0.2125 meters, for the power density variation depicted in Fig. 58. Assuming COMSOL correctly transfers the energy to the fluid, the assumed heat flux at the prescribed location is $1.477676(10^6)$ W/m^2. In addition the bulk temperature used in the following calculations is an average of the coolant channel centerline temperature. This average assumes the inlet temperature is 321.9 K and the centerline temperature at the end of the fueled region is 336.3K. The average centerline temperature is thus, 329.1 K. The bulk temperature is rounded to 330 K. At this location, COMSOL predicted a wall temperature of 337.8 K (average of a temperature jump between the cladding and the coolant).

Given these temperature values and the applied heat flux, the COMSOL simulated heat transfer coefficient can be determined. COMSOL calculates a heat transfer coefficient of 199546 (W/m^2*K).

The Dittus Boelter and revised Modified Hausen predictions were made via the MATLAB code presented in Appendix B. The code neglects property variations, and the COMSOL bulk temperature is applied. The resulting wall temperatures as predicted by the Dittus Boelter and Revised Modified Hausen are 352 K and 350 K, respectively. The heat transfer

coefficient associated with each of these temperatures are 81019 (W/m^2*K), and 88393 (W/m^2*K).

5.3 Observations from Review of the 2D Fuel Conduction, 2D Flow Model

All of the model meshes in this section correctly show a boundary layer mesh in the coolant (fluid) adjacent to the fuel cladding wall. However, there is also a companion refined mesh, as if there were a boundary layer, within the clad sub-domain and again in the coolant free-stream symmetrical boundary. This was likely caused by the automatic features of the COMSOL mesh generator and not by purposeful user input.   Fortunately, this additional mesh should not invalidate the solution unless the mesh becomes extremely fine to the point of causing round-off error in the solution. This can happen, but is unlikely in this application. Therefore, the main negative impact of having the refined mesh where it is not needed is to add additional degrees of freedom to the problem solution, and as a consequence, add more cpu time and memory requirement to each problem solution.

The COMSOL automatic mesh generator features can be over-ridden and refined mesh can be placed only where it is needed. Indeed, mesh generation features new at version 3.4, called "interactive mesh generation" allow the user to first create a free or unstructured mesh, and then impose a boundary layer, or structured mesh only adjacent to the boundary where a fluid flow interface exists. These new advanced mesh generation features are not easy to grasp and were not utilized in this instance.

The issue of unnecessary mesh is exacerbated when the problem definition is extended to 3D. The fuel-plate geometry is a good example whereby if previously shown mesh surfaces in 2D are extended span-wise from side plate to side plate, the number of mesh points is roughly 3 times the minimum necessary to compute an adequate solution. A preliminary model to address this issue and others is discussed in Section 7.3 (3D observations). An end-view of the mesh generation used in this preliminary model is shown below in Figure 67.
– Top View of the Mesh Design for a Preliminary 3D Model of the HFIR Fuel Half-Plate and Half-Coolant Channel; top full view, bottom zoom near side plate shown boundary layer meshing.
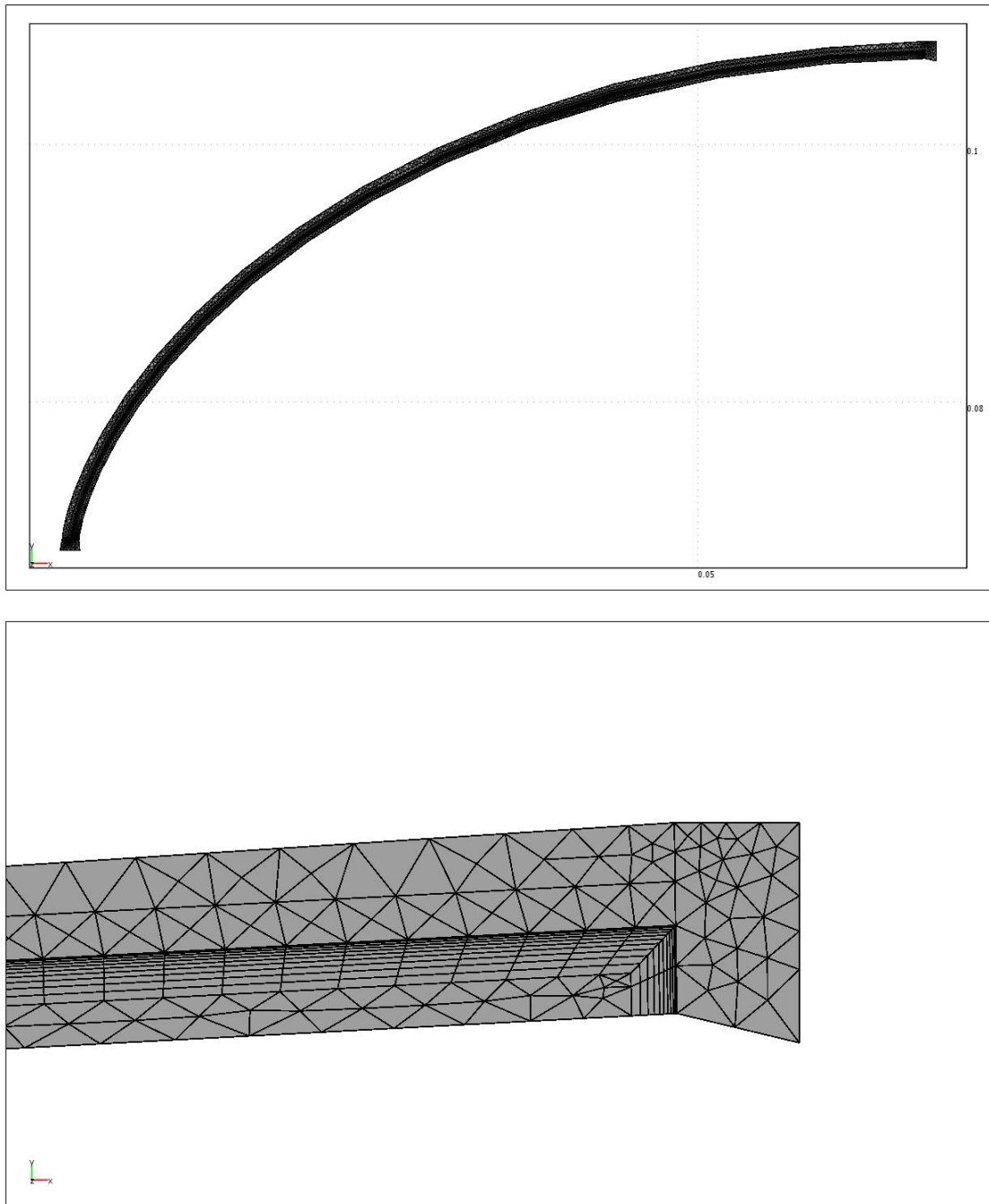
Fig. 67. Preliminary 3D model of the HFIR fuel half-plate and half-coolant channel

6.0 EXTENSION OF 2-D SIMULATION TO THREE DIMENSIONS

The initial 3-dimensional simulation of the half fuel plate and half coolant channel model is constructed by taking the 2-dimensional model, shown in Fig. 68, and extending it into the z-direction by 0.001 m. There are no side walls to the z direction extension of the cooling channel, so corners and attendant secondary flows are not part of the expected simulation outcomes. This simulation should render outcomes almost exactly like the previous 2-dimensional simulation if the mesh is similar. The COMSOL generated mesh is displayed in Fig. 69.
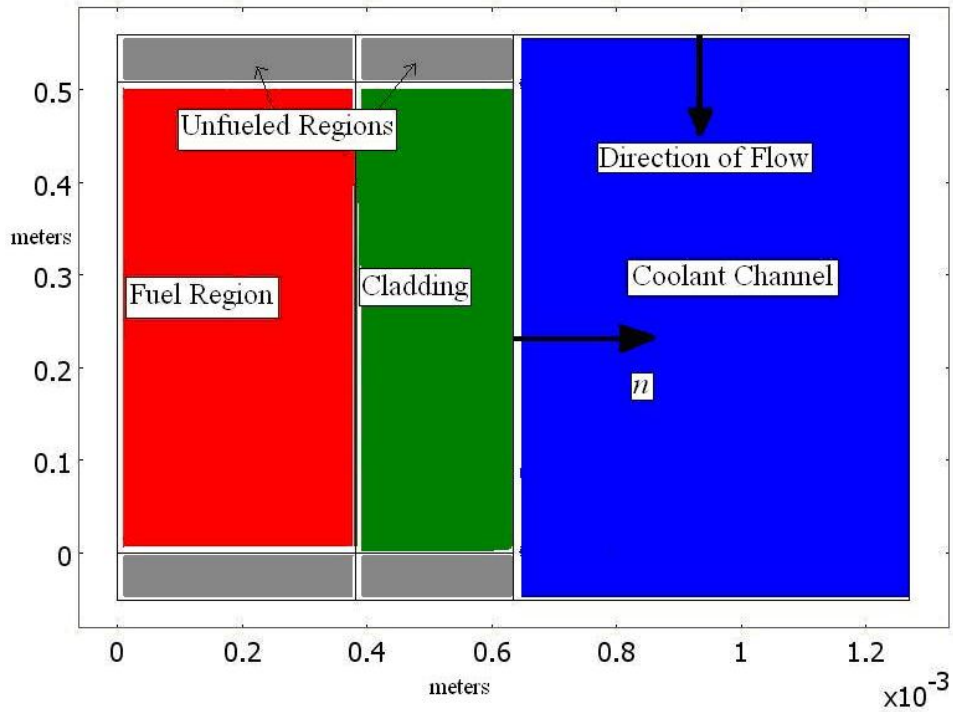
Fig. 68. 2D model.
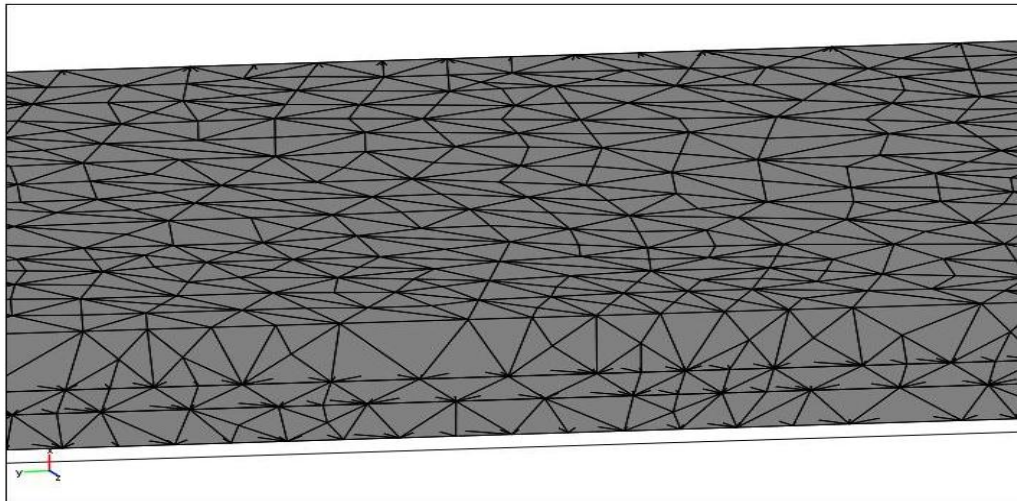
Fig. 69. 3D mesh simulation (3dsolution_random_meshv1.mph).

The mesh consists of $1.09(10^6)$ mesh elements and $1.18(10^6)$ degrees of freedom. This free mesh is coarse compared to previous 2-dimensional modeling efforts, especially in the near wall fluid region. The fuel plate surface temperature of the free-mesh generation is displayed in Fig. 70.
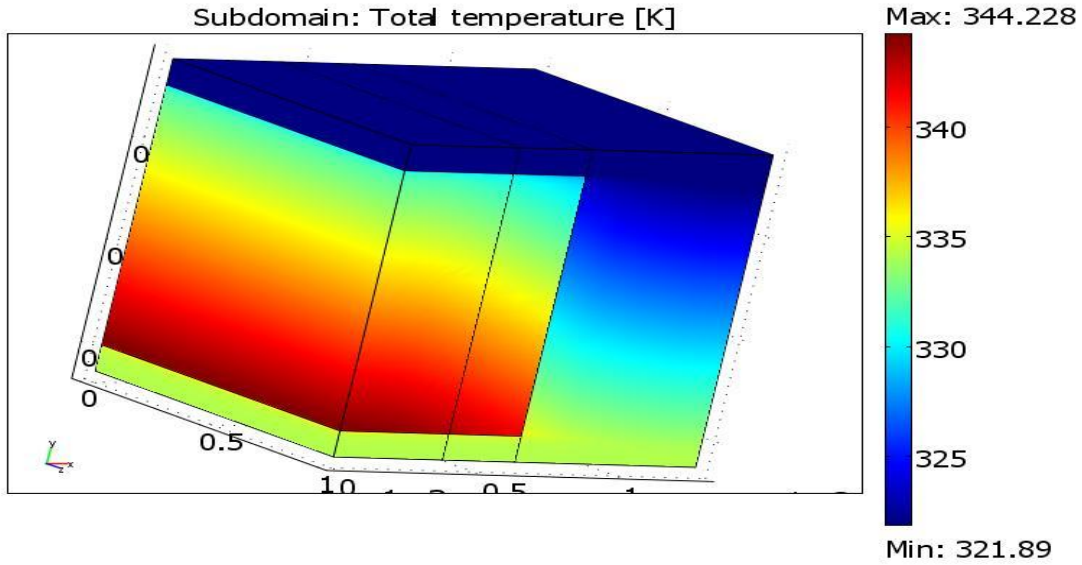
Fig. 70. Temperature distribution (3dsolution_random_meshv1.mph).

The maximum simulated temperature for this solution was 344.228 K, the maximum from previous more refined 2-dimensional simulations using the same uniform power density and flow parameters is 343 K. The temperature distribution at various layers within the fuel plate region is shown in Fig. 71.
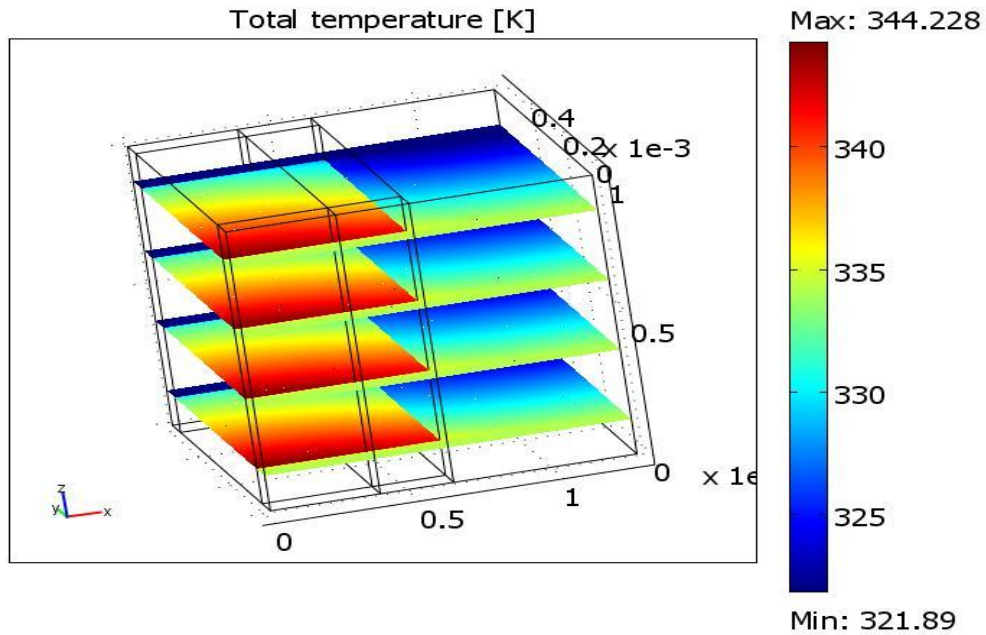
Fig. 71. Temperature distribution at layers (3dsolution_random_meshv1.mph).

6.1 Revision of model to incorporate mapped mesh

Next, a simulation of a full length channel was performed using a *mapped mesh*. Fig. 72 is the 2-dimensional representation of the simulation. The 2-dimensional mesh was extruded 0.1 meters (100 times larger than the previous case) to create the 3-dimensional simulation and the resulting mesh is depicted in Fig. 73.
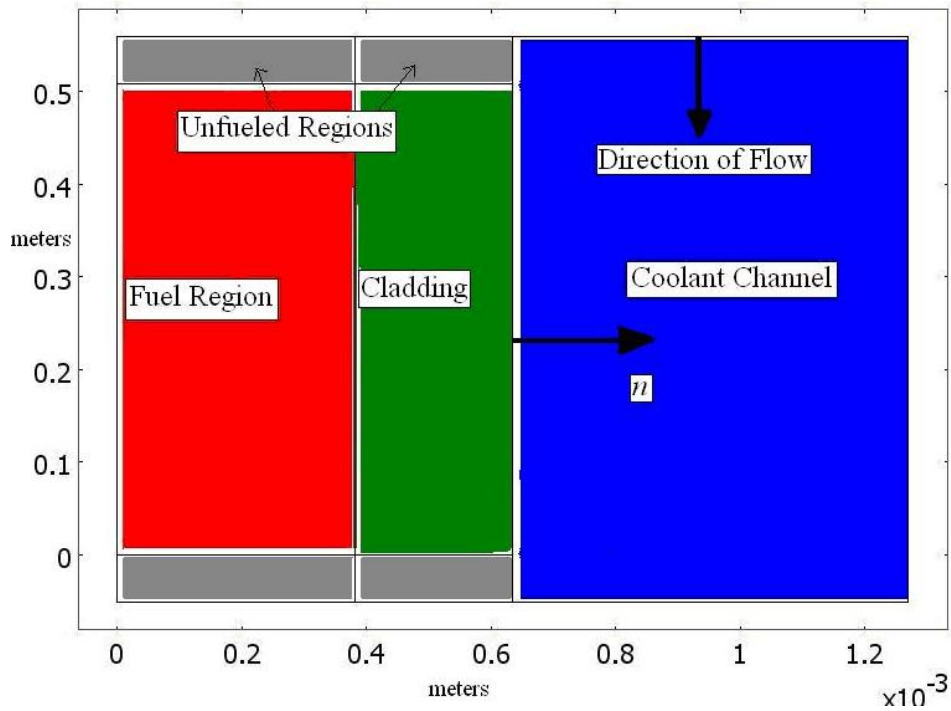
Fig. 72. 2D representation (3D_mapped_mesh_v1.mph).
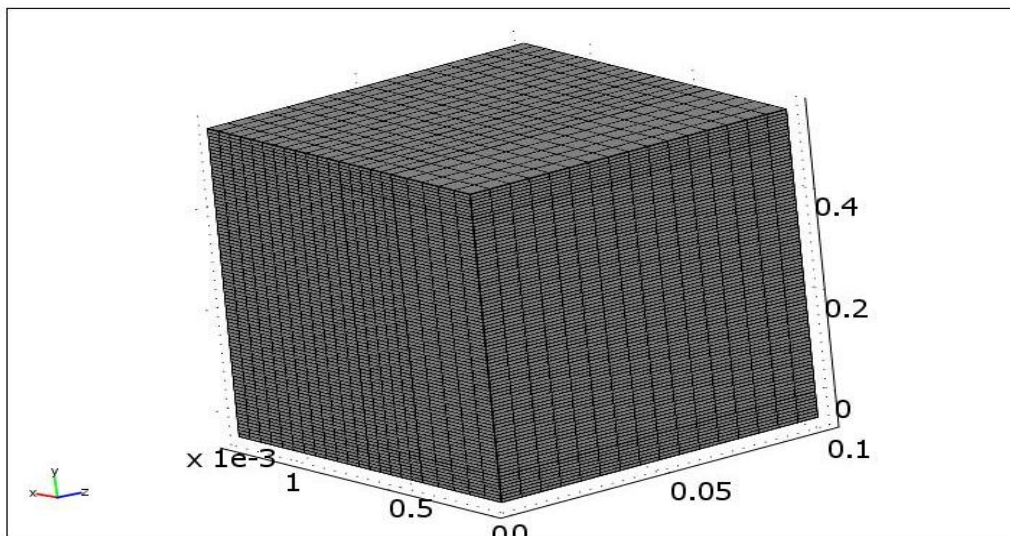
Fig. 73. Mapped mesh (3D_mapped_mesh_v1.mph).

This mesh consists of 32032 elements and 169546 degrees of freedom. The resulting temperature distribution for this simulation is displayed in Fig. 74.
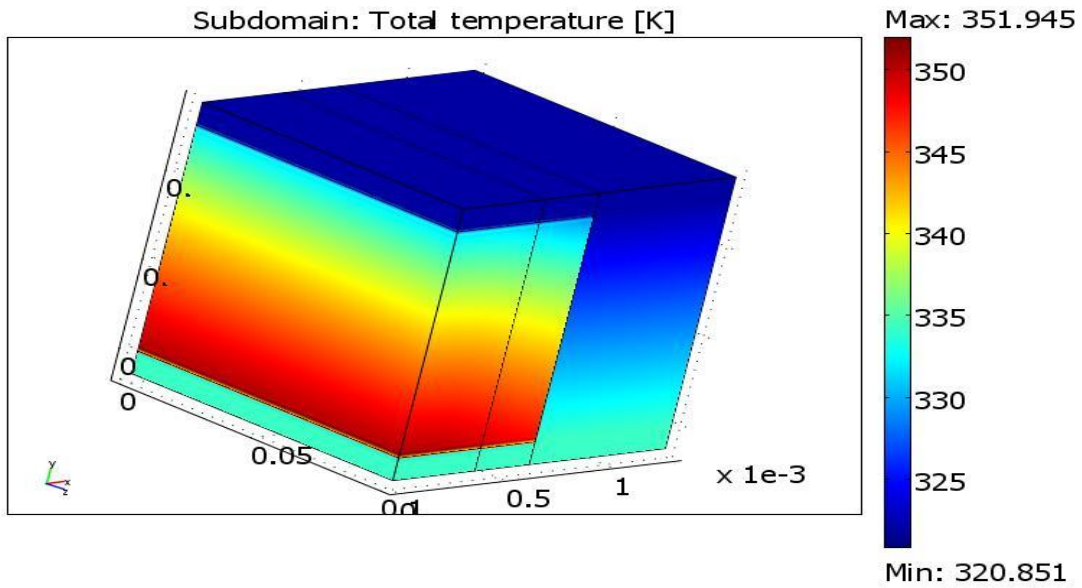
Fig. 74. Temperature distribution (3D_mapped_mesh_v1.mph).

Figure 75 displays the temperature distribution at regular intervals throughout the fueled region. The mapped mesh simulations result in peak fuel centerline temperatures nearly nine degrees higher than those predicted using the free-mesh generation option.
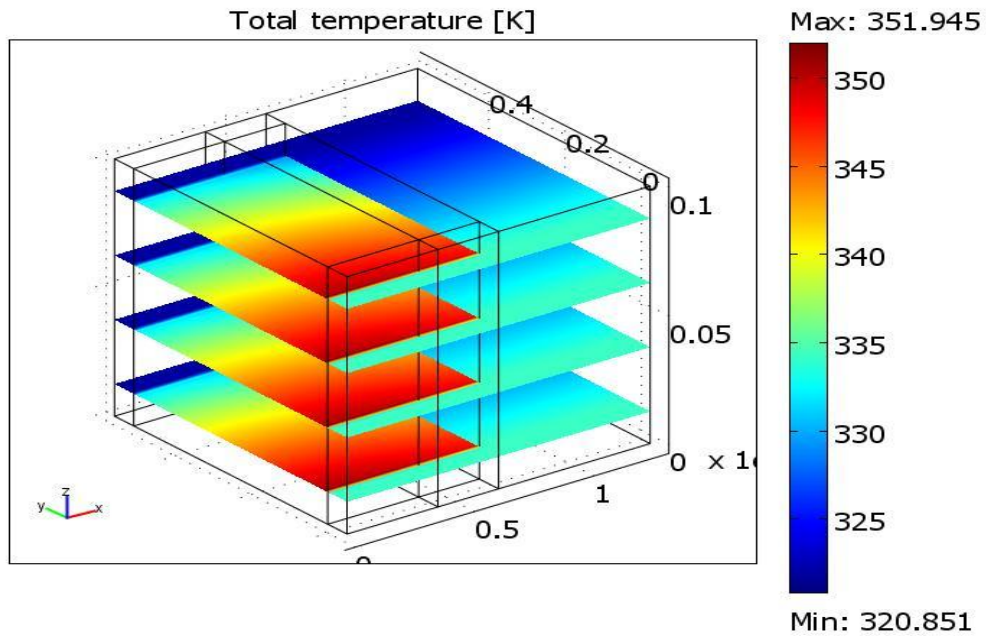
Fig. 75. Temperature distribution (3D_mapped_mesh_v1.mph).

6.2 Conclusions from extending model to three dimensions

The maximum simulated temperature for this solution was 344.228 K, the maximum from previous more refined 2-dimensional simulations using the same uniform power density and flow parameters is 343 K. While the level of agreement is close, further investigation is needed to understand the source of the difference. Likely a related problem is that the mapped mesh simulations result in peak fuel centerline temperatures nearly nine degrees higher than those predicted using the free-mesh option. Resources available for this study limited further investigation at this time. These results are reported to provide a "starting point" for future studies.

This page blank.

7.0 THREE DIMENSIONAL SIMULATIONS OF FULL HFIR ELEMENT

The extension of the two-dimensional HFIR plate model to three dimensions – discussed in the previous section – revealed inconsistencies among COMSOL solutions that are not currently understood. Nevertheless, model development proceeded with the intent of examining the impact of perturbations in the model on calculated thermal hydraulic parameters.

7.1 Hot stripe in fuel due to mis-manufacture

A hot stripe simulation was conducted for a 3-dimensional model. The total width of the simulated channel was 0.024 meters. This simulation had a 0.004 meter wide hot stripe that extends the length of the channel. The hot stripe is 20% higher volumetric heating than the surrounding fuel. The volumetric heating of the hot stripe is $3.19(10^9)$ W/m^3 and the volumetric heating of the surrounding fuel is $2.66(10^9)$ W/m^3. The temperature profile for the hot stripe simulation is displayed in Fig. 76. The mesh used for the hot stripe simulation is presented in Fig. 76.
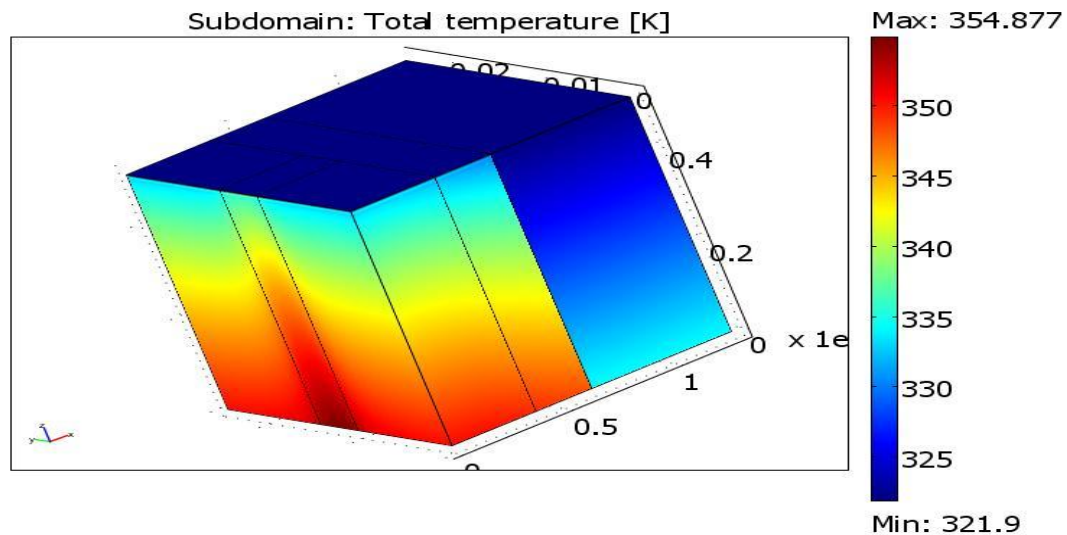
Fig. 76. Temperature profile (hotstripe_3Da.mph).
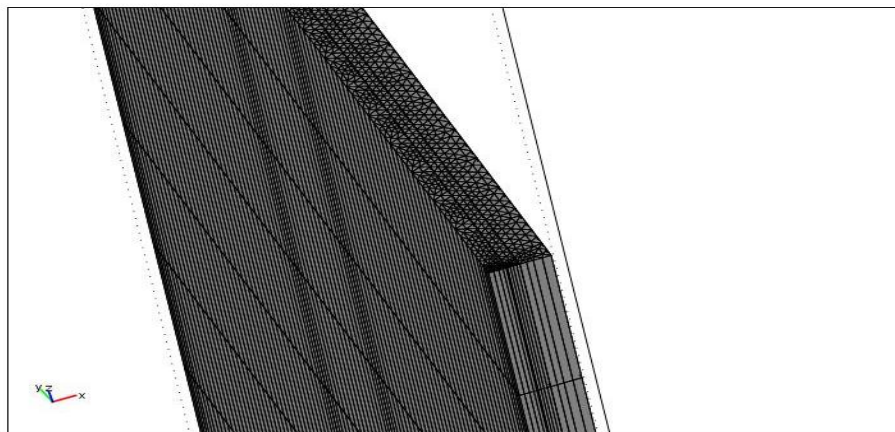
Fig. 77. Mesh density (hotstripe_3Da.mph).

69

Figure 78 is the temperature profile at the surface of the cladding at an axial position of 0 and 0.1 meters. Figure 79 is the temperature profile $2.65(10^{-4})$ meters into the channel.
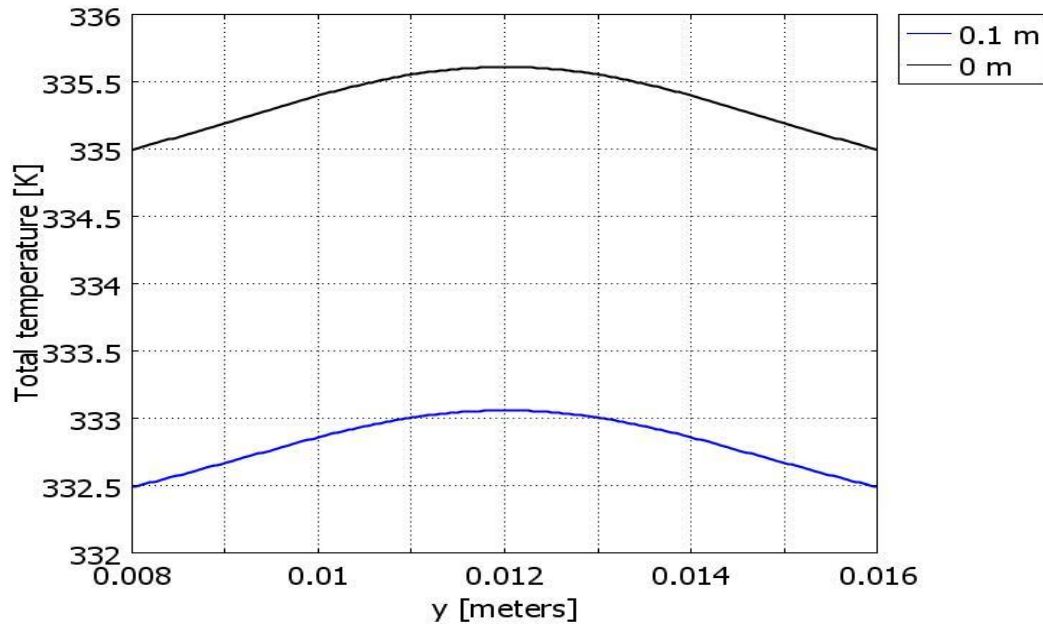
Fig. 78. Cladding temperature near the exit (hotstripe_3Da.mph).
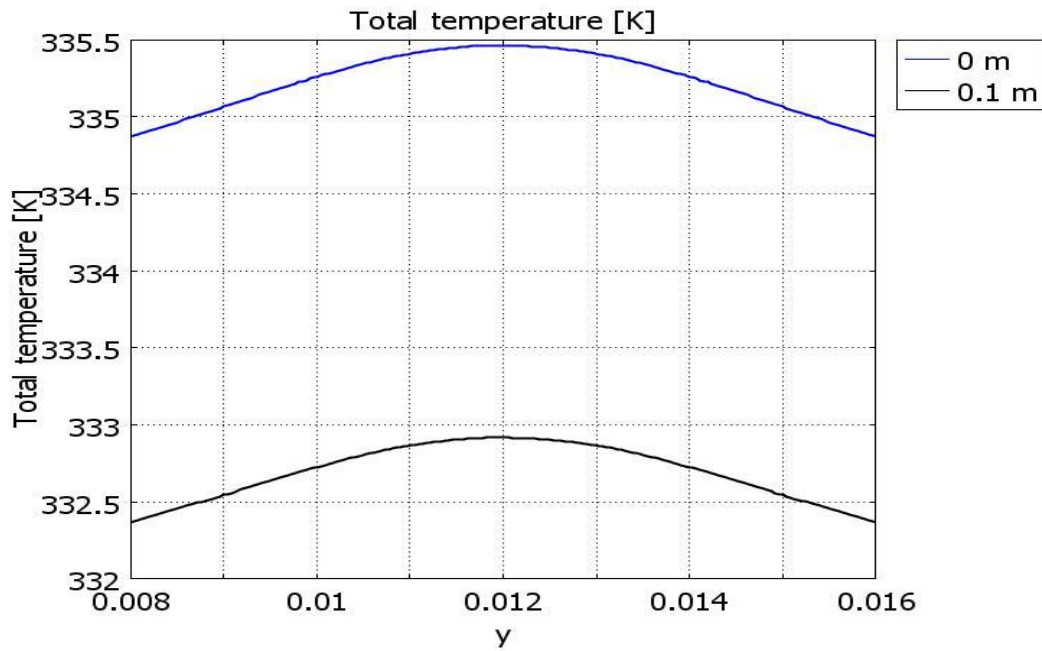
Fig. 79. Temperature profile in coolant (hotstripe_3Da.mph).

The turbulent conductivity values at the entrances, mid-channel, and exit are displayed for the hot stripe simulation in Fig. 80-82. The expected value for the turbulent conductivity in HFIR is approximately 150-250 W/(m*K), per the values developed for fuel hot stripe simulations performed by Ruggles in 1997, using models from Hatton and Quarmby, 1963. The COMSOL simulated turbulent conductivity is 1-2 orders of magnitude larger in these simulations. The unnaturally large conductivity values cause the energy across the hot stripe to be artificially conducted to surrounding fluid. This error likely stems from the coarse nodalization of the fluid flow channel. Finer nodalization is not practical .when using the direct-solver solution methods of COMSOL. Utilizing the more memory-efficient indirect iterative solvers available in COMSOL will allow for finer nodalization to be solved at the expense of longer solution times. The choice of using the more-complex default indirect iterative solution method provided by COMSOL for 3D flow problems was determined to be beyond the scope of this research project.
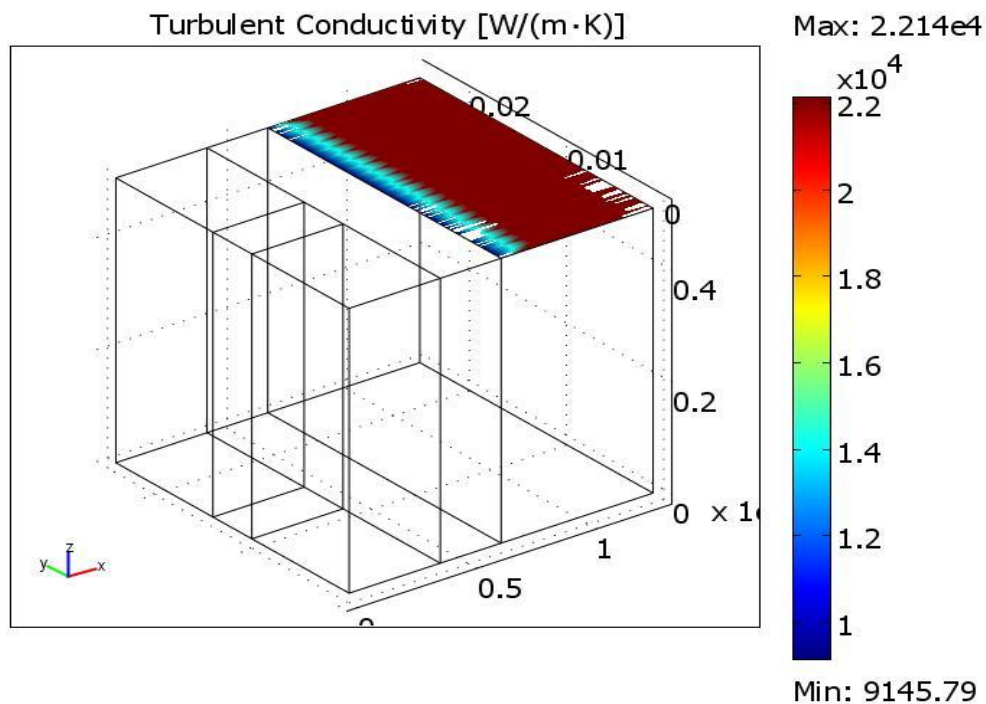
Fig. 80. Turbulent conductivity, entrance (hotstripe_3Da.mph).
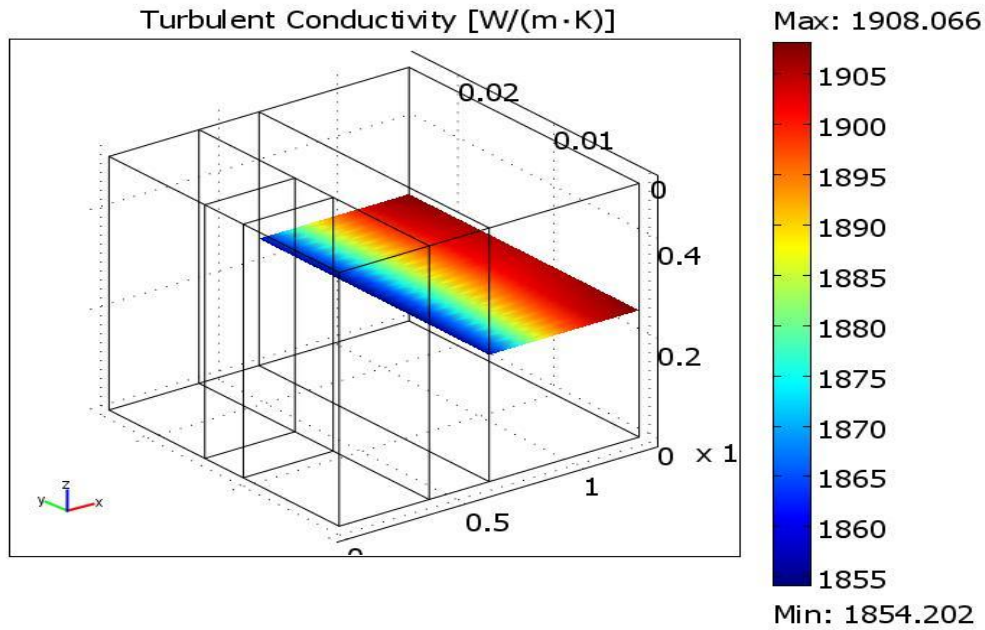
Fig. 81. Turbulent conductivity, mid-channel (hotstripe_3Da.mph).
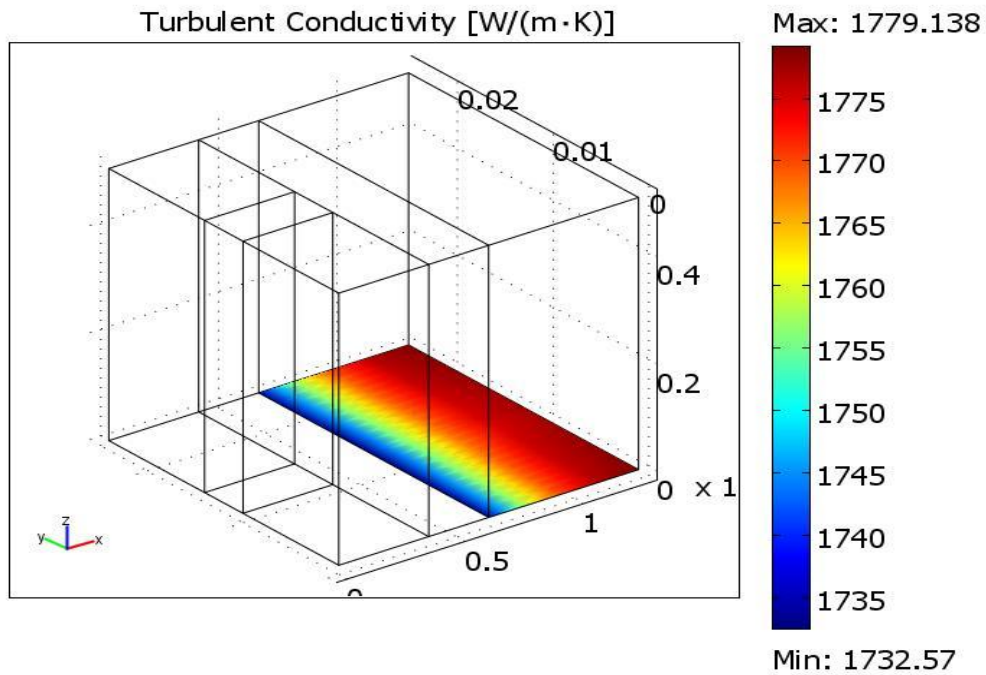
Fig. 82. Turbulent conductivity, exit (hotstripe_3Da.mph).

The 3-dimensional simulations were modified to include a hotspot condition similar to the analysis from the 2-dimensional simulation, but only extending partially across the channel span. The fuel plate and coolant channel were 0.204 meters long in order to minimize the computation resource requirements that a longer channel would require. Figure 83 shows the 3-dimensional model. The high power fuel region depicted in Fig. 80 is $3.19(10^9)$ W/m^3 and the low flux fuel region depicted in. 83 is $2.66(10^9)$ W/m^3.

72
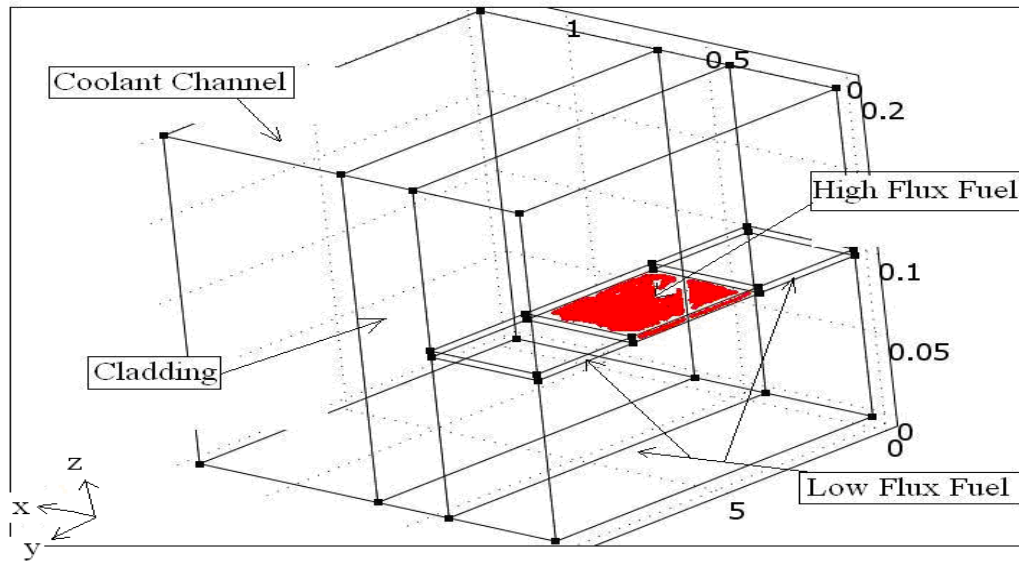
Fig. 83. Hotspot picture (hotspot_3D_v2a.mph).

The boundary conditions for this model are shown in Figs. 84-86. Figure 84 depicts the boundary conditions for the k-epsilon module. All boundary conditions not shown in Fig. 84 are symmetry boundaries.
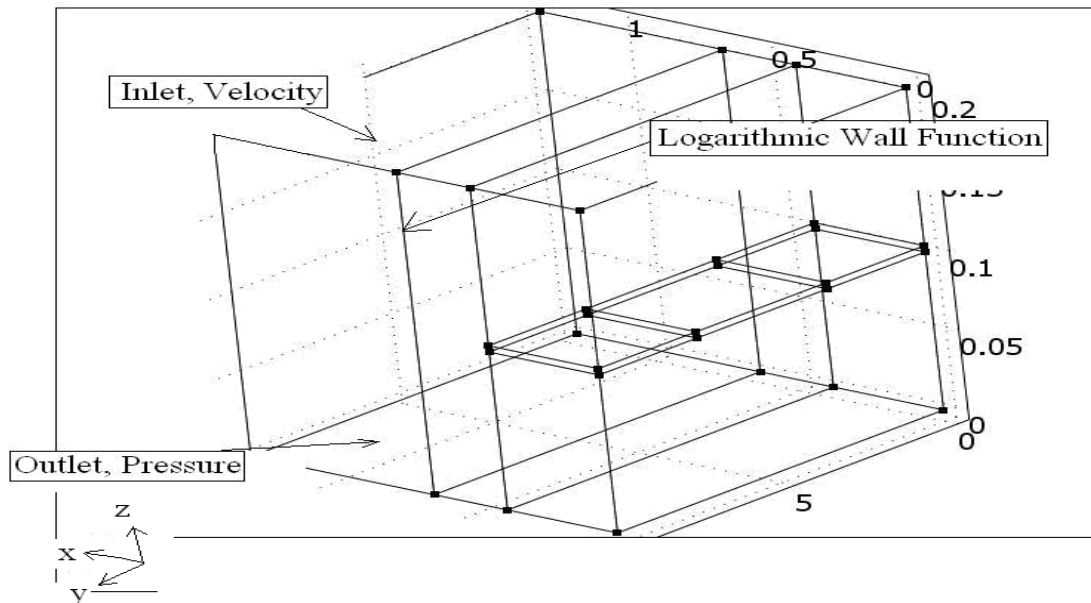
Fig. 84. K-Epsilon fluid boundary conditions.

Figure 85 depicts the heat transfer boundary conditions for the coolant channel. The boundary conditions that are not depicted in Fig. 85 are thermal insulation boundary conditions.
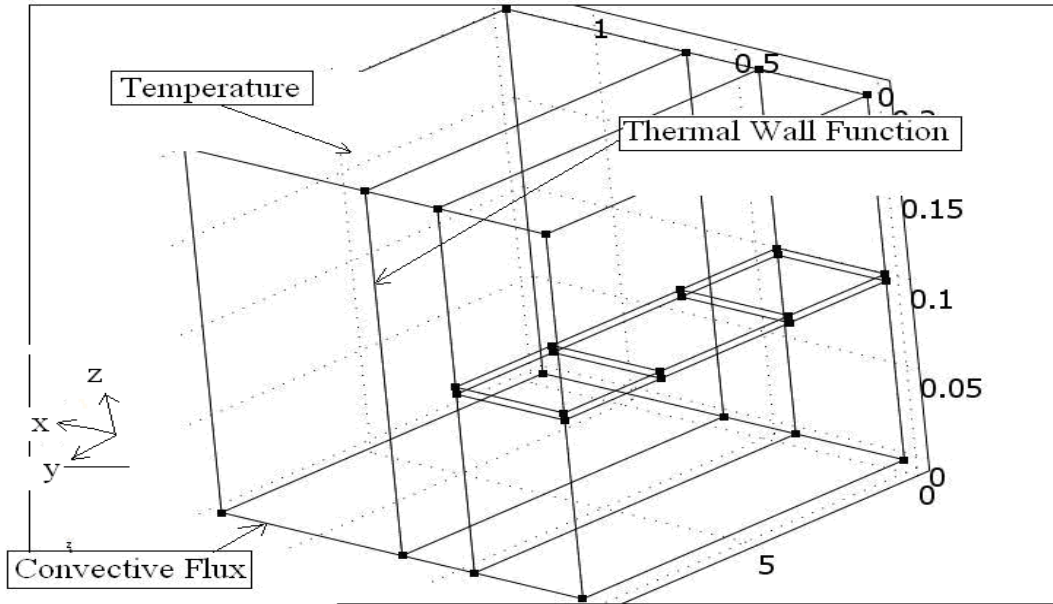
Fig. 85. Fluid heat transfer boundary conditions.

Figure 86 depicts the heat transfer boundary conditions for the fuel plate. The external boundary conditions that are not depicted in Fig. 86 are thermal insulation boundary conditions and the internal boundary conditions are all continuity.
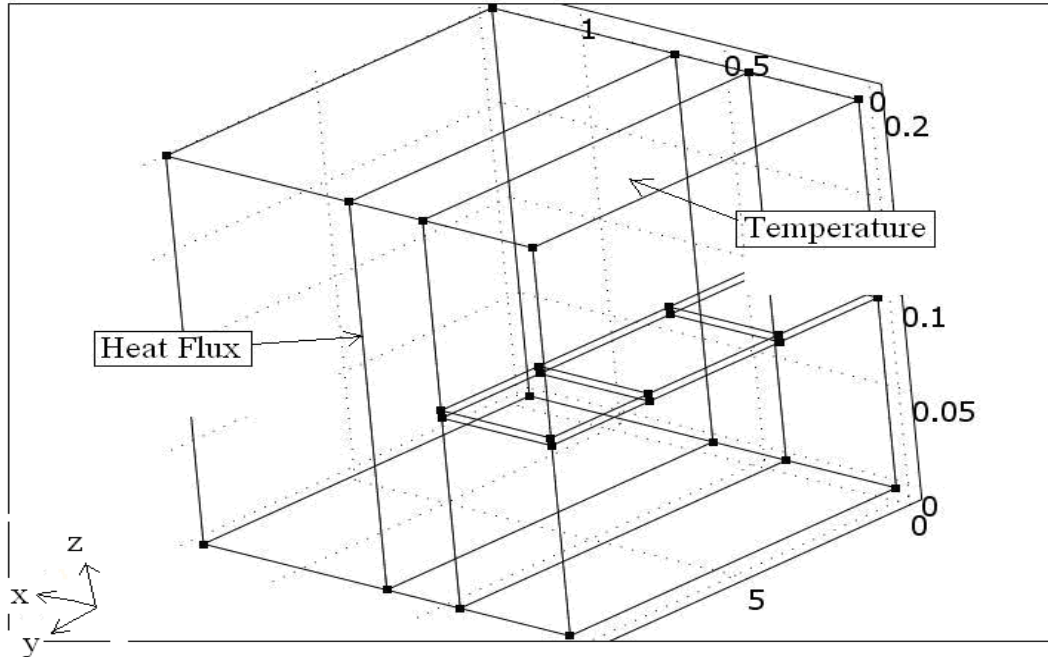
Fig. 86. Fuel plate heat transfer boundary conditions.

The mesh that is used in the evaluation of this simulation is depicted in Fig. 87. Figure 87 consists of 1,146,905 elements and 828,584 degrees of freedom. (In the free mesh parameter dialogue box in COMSOL, the predefined mesh size is set to Extra Fine.)
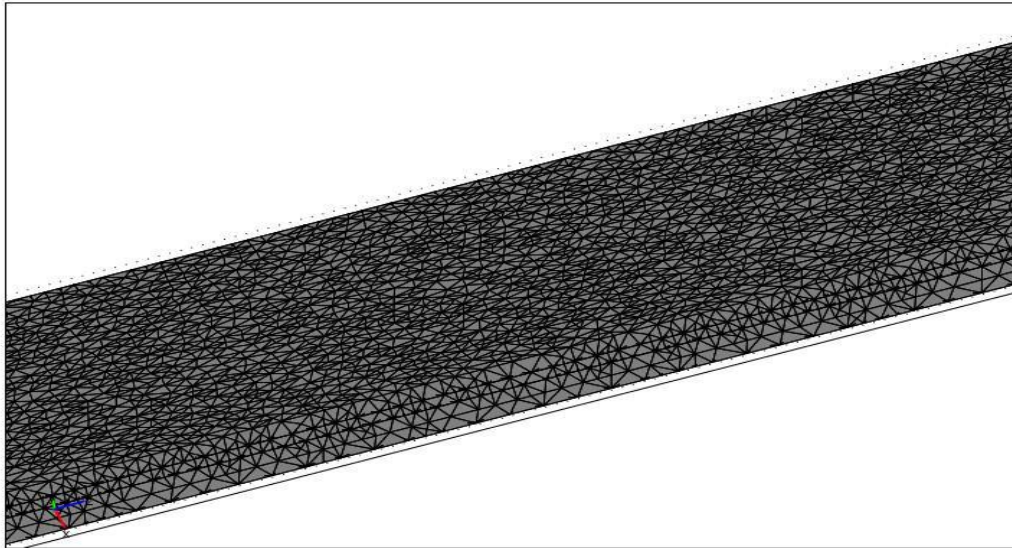
Fig. 87. Mesh for the hotspot simulation (hotspot_3D_v2a.mph).

Figure 88 depicts the temperature distribution for the hotspot analysis. Figure 89 depicts the Maximum fuel centerline temperature. This profile corresponds to the position x0 = 0 y0 = 0 z0 = 0.102; x1 = 0 y1 = 0.01 z1 = 0.102. Artifacts of the mesh coarseness are apparent in Fig. 89. Flow is from left to right.
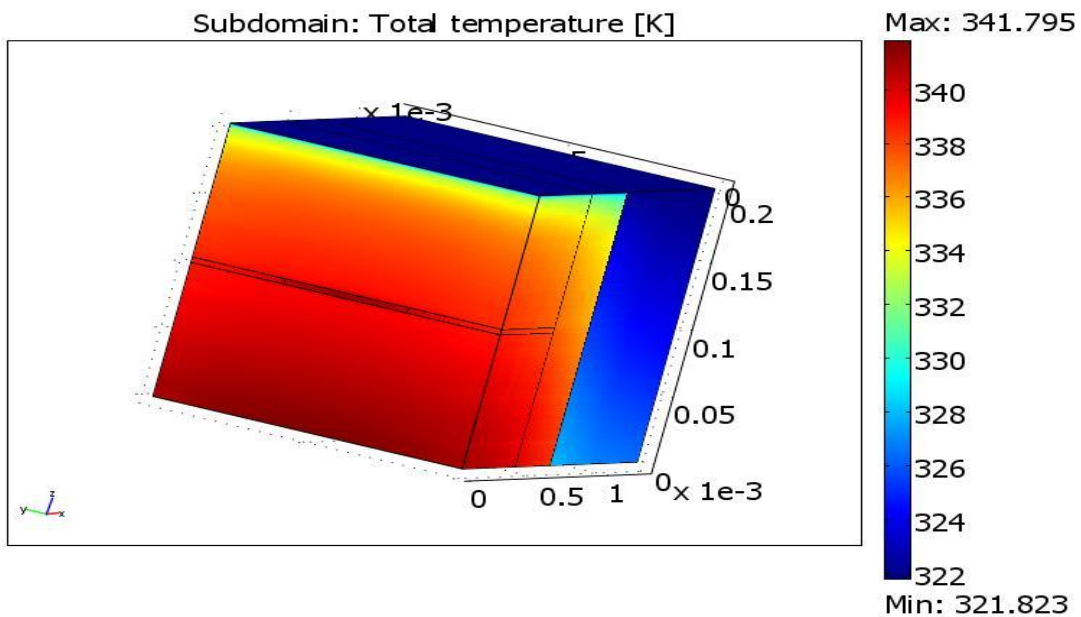
Fig. 88. Temperature distribution (hotspot_3D_v2a.mph).
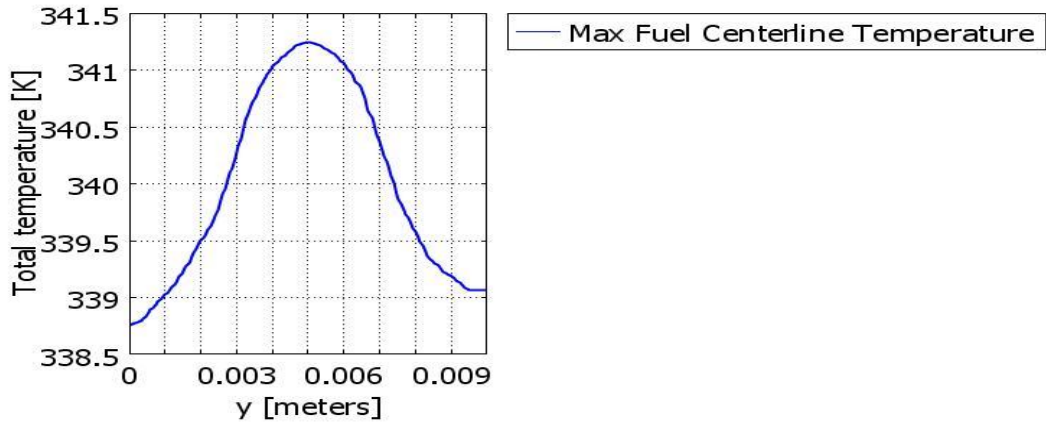
Fig. 89. Max Fuel centerline (hotspot_3D_v2a.mph).

Figure 90 displays three temperature profiles extending from the fuel centerline to the coolant channel centerline at z position 0.102 meters. Each temperature profile is positioned at the hot spot center along the z-axis shown in Fig. 88, with the profile at y=0.005 corresponding to the hot spot spanwise center, and the subsequent y positions of 0.003 and 0.0015 moving to the right on Fig. 88. The three temperature profiles show the influence of spanwise conduction on the hot spot temperature profile attributable to the additional dimension in the simulation.
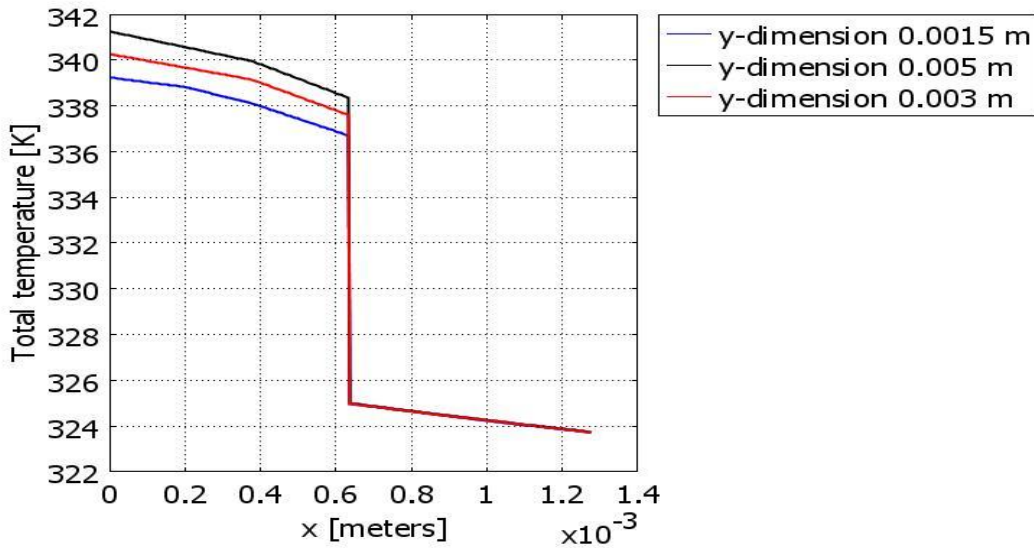
Fig. 90. Hotspot temperature profile (hotspot_3D_v2a.mph).

Figure 91 represents the same hotspot in a 2-dimensional simulation.
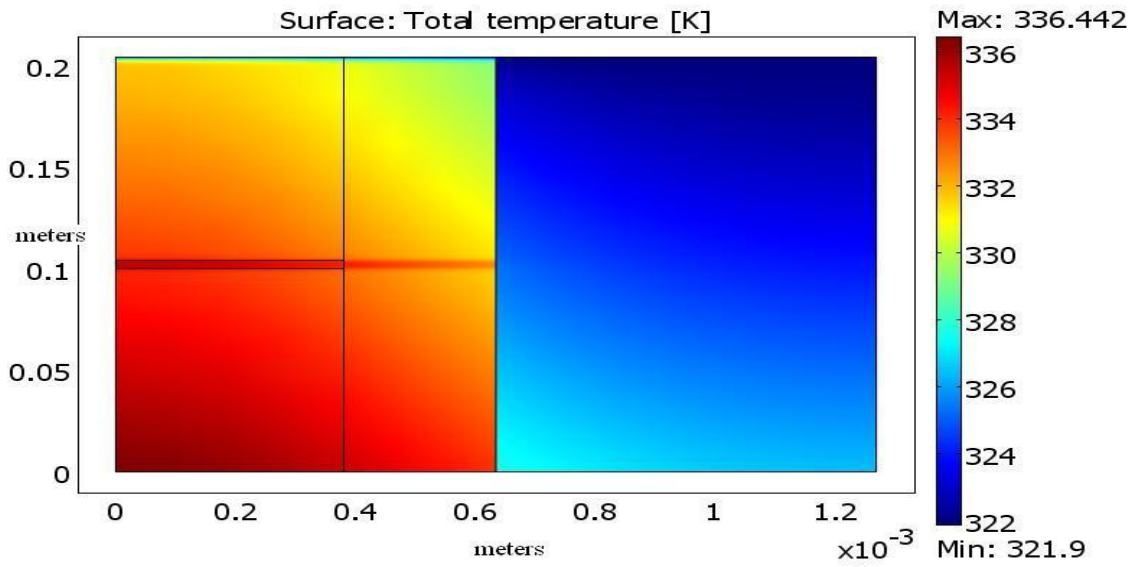
Fig. 91. Temperature distribution (004thickhotspot_2Dv1.mph).

Figure 92 displays the mesh used in the 2-dimensional simulation displayed in Fig. 91.
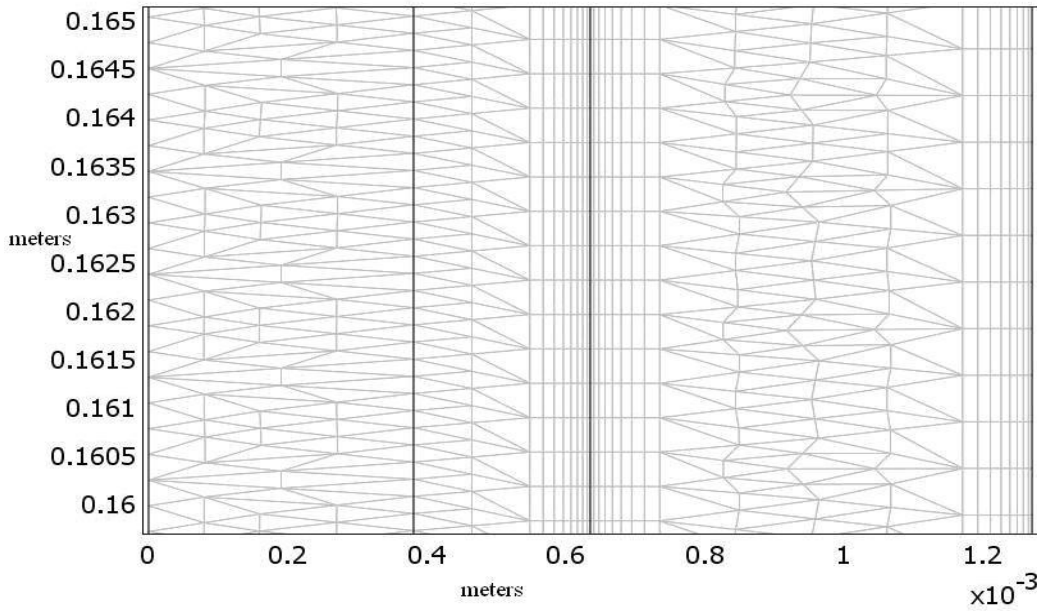
Fig. 92. Mesh for 2D hotspot simulation (004thickhotspot_2Dv1.mph).

The temperature profile at the center of the hotspot region is displayed in Fig. 93.
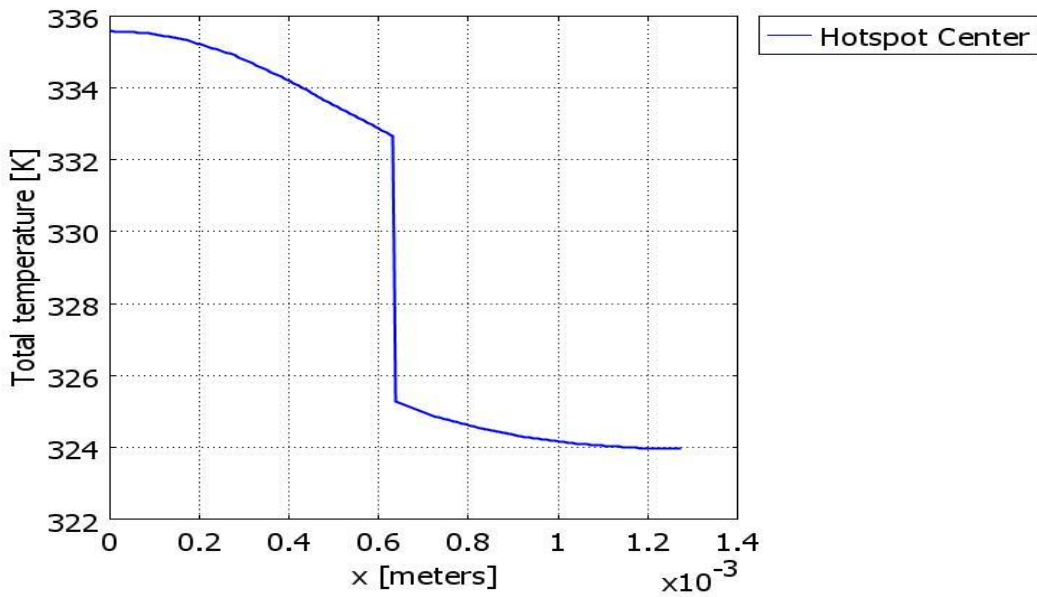
Fig. 93. Hotspot temperature profile (004thickhotspot_2Dv1.mph).

The 2-dimensional simulation outcome for peak fuel temperature is less by 5 degrees than the 3-dimensional simulation outcome. One would physically expect a lower peak temperature in the 3-dimensional simulation outcome due to availability of spanwise conduction. When the temperature profile at the cladding/coolant interface is examined, the profile first reported in Fig. 56 and reproduced for the shorter channel, as shown in Fig. 94, is distorted in the 3-dimensional simulation, as seen in Fig. 95. The coarse nodalization in the 3-dimensional model is likely contributing to low fidelity in the 3-dimensional result. Finer nodalizations are currently not practical when using the current direct-solver solution methods of COMSOL. Utilizing the more memory-efficient indirect iterative solvers available in COMSOL will allow for finer nodalization to be solved at the expense of longer solution times. The choice of using the more-complex default indirect iterative solution method provided by COMSOL for 3D flow problems was determined to be beyond the scope of this research project.

78
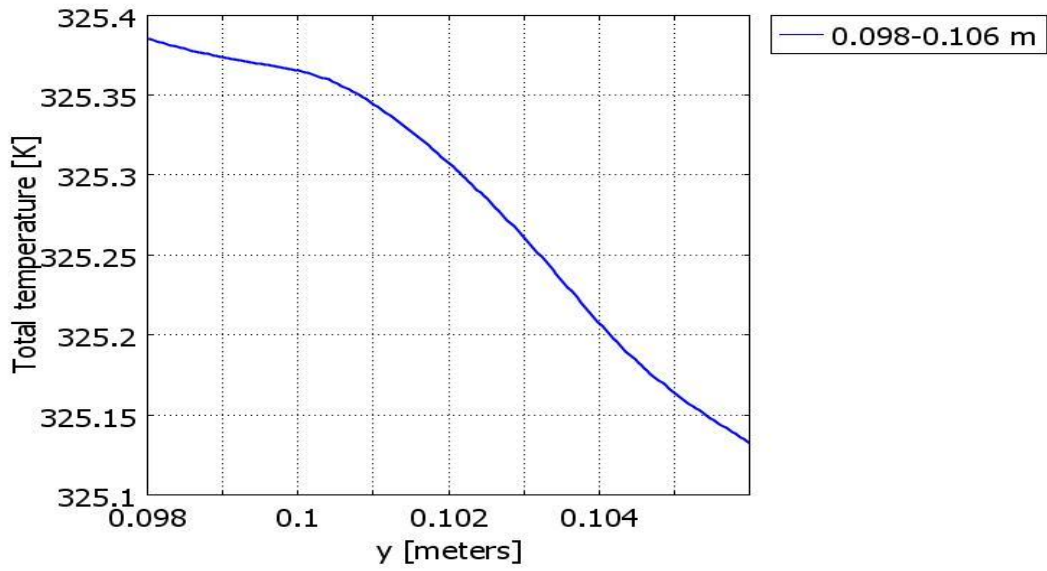
Fig. 94. Temperature Profile at cladding coolant interface (004thickhotspot_2Dv1.mph).
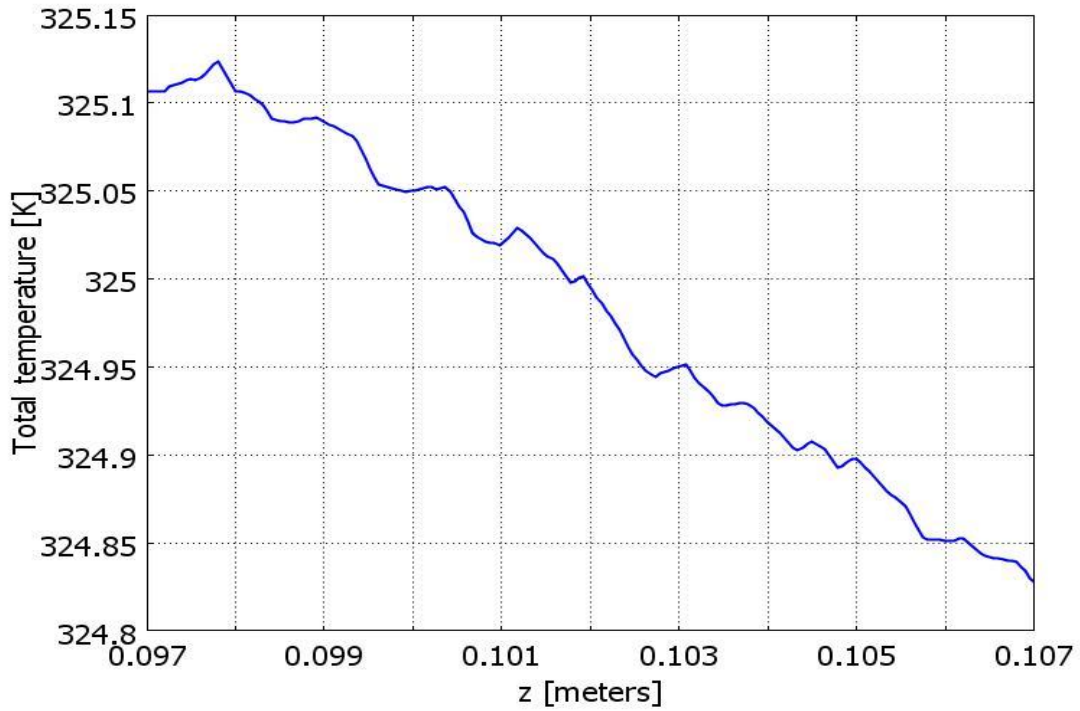
Fig. 95. Temperature profile at cladding/coolant interface (hotspot_3D_v2a.mph).

7.2 Effect of element side plate on thermal hydraulic parameters

In order to examine the effects that the side wall/plate separators have on the flow and the heat transfer to the coolant, a model was created with the coolant channel bounded on three sides by a solid wall. The material for this wall was assumed to be identical to the cladding. This simulation was performed for a 0.4572 meter long channel. Figure 96 depicts the temperature distribution for the enclosed channel. Fig. 97 shows the mesh used to generate results shown in Fig. 96.
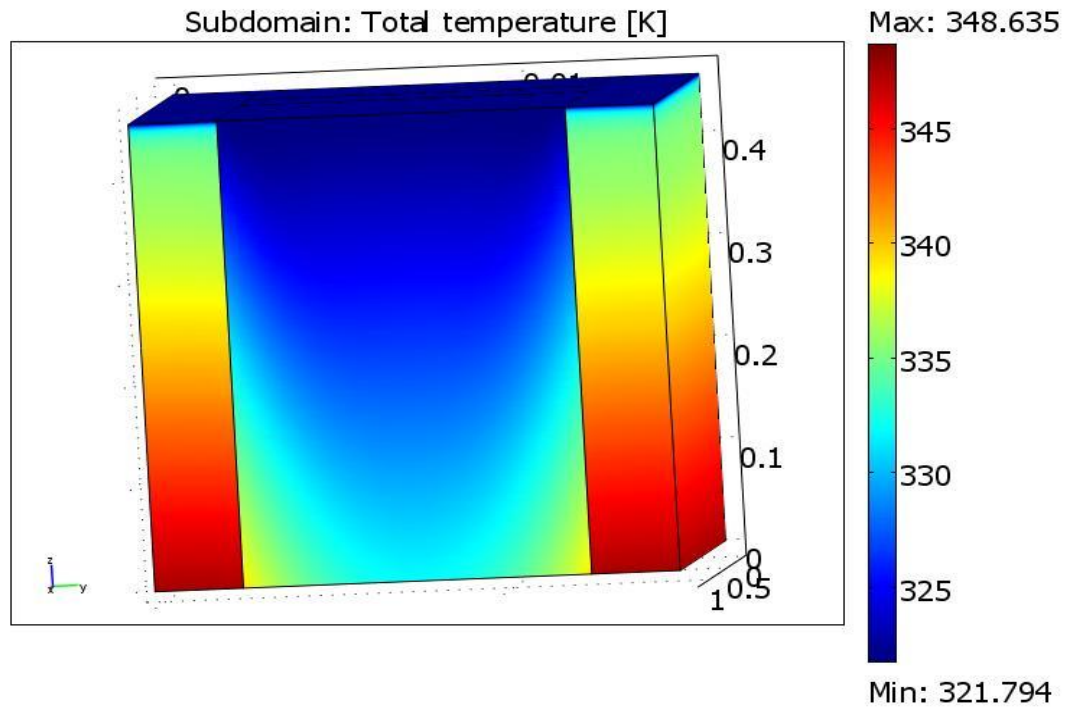
Fig. 96. Temperature profile (3sidedflowchannel_3D_3v1.mph).
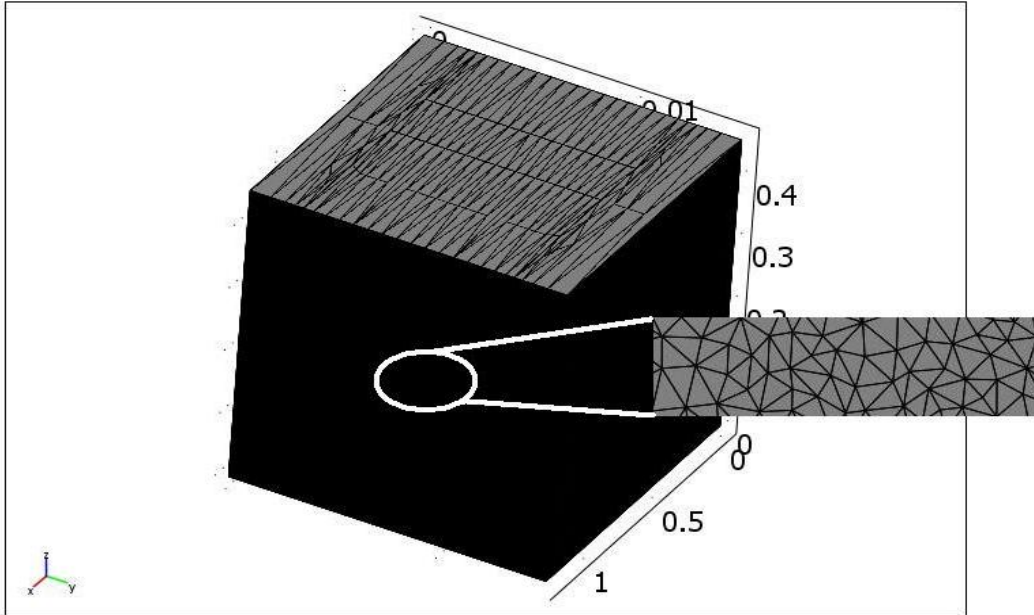
Fig. 97. Mesh for flow simulation (3sidedflowchannel_3D_3v1.mph).

The simulated vorticity is displayed in Fig. 98. A slice plot of the vorticity is displayed in Fig. 99. Figure 100 is the sliced velocity profile through the coolant channel.
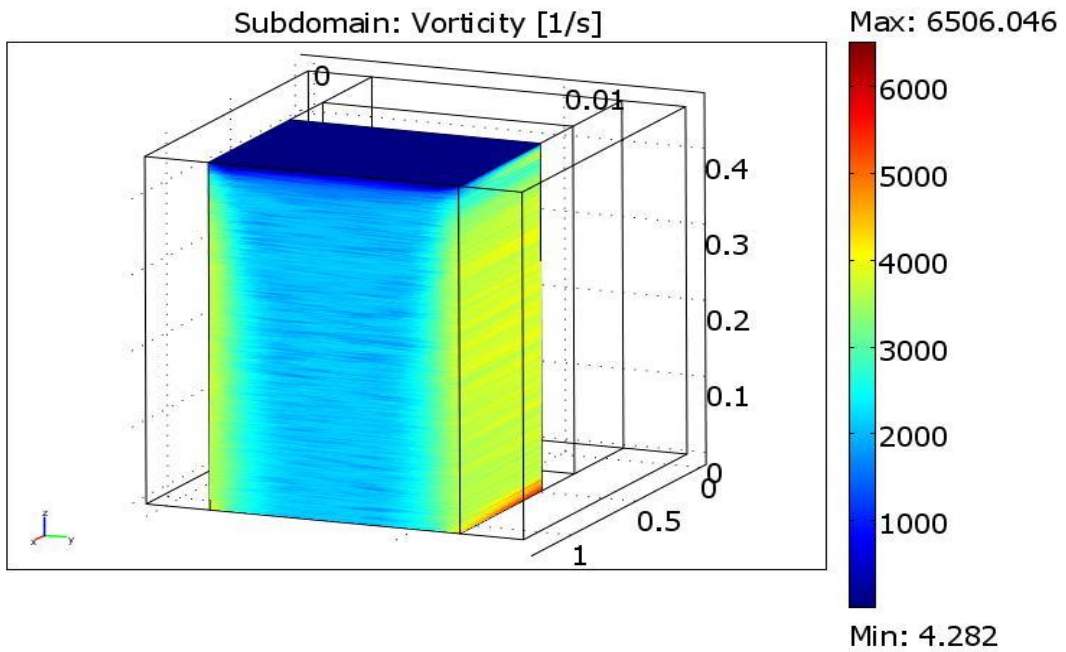
Fig. 98. Vorticity profile (3sidedflowchannel_3D_3v1.mph).
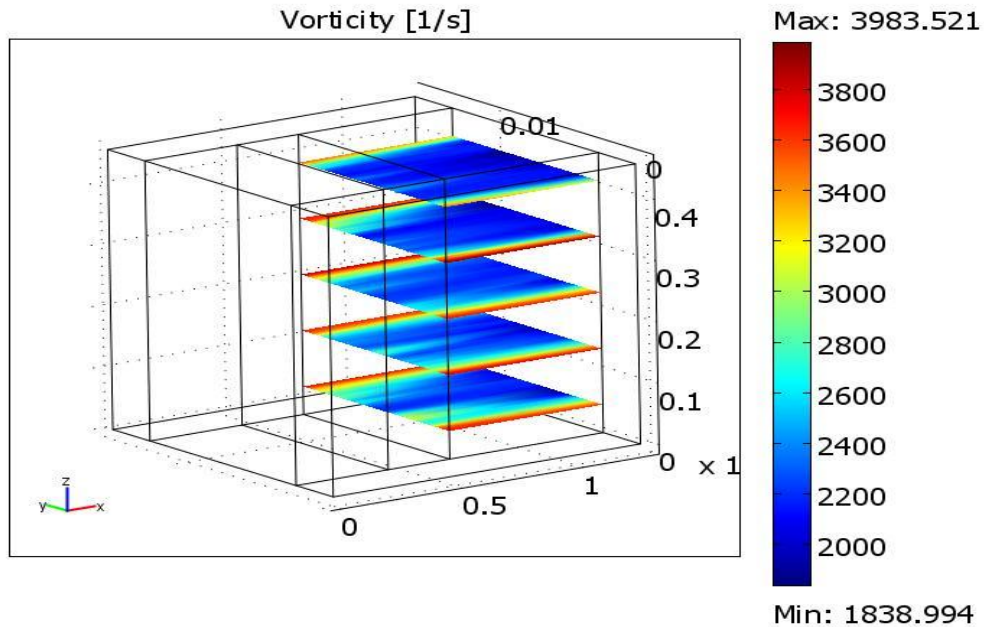
Fig. 99. Slice plot of the vorticity (3sidedflowchannel_3D_3v1.mph).
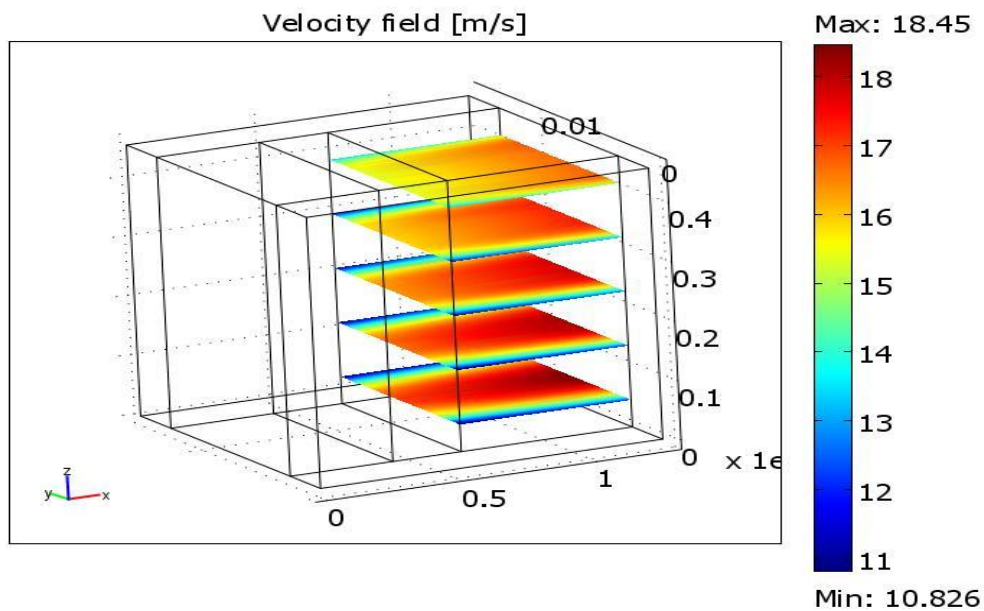
Fig. 100. Velocity profile (3sidedflowchannel_3D_3v1.mph).

The partial length channel velocity profile (Fig. 99) and vorticity profile (Fig. 98) predictions near the fuel clad to coolant interface are not physical. They are likely due to the coarse nodalization of the fluid flow channel, especially in the gapwise dimension.

7.3 Observations from review of three dimensional simulations

One observation that was found in this research was the demanding computational resources that are required for full 3D solutions to be obtained. This observation is true for any

large CFD code, but is particularly true for COMSOL, a finite-element based multiphysics code. Even so, modern computer resources are sufficient for solving 3D problems of this type provided that the user understands how to use the features available to him. One price paid for the code flexibility and power, comes the understanding of how to use the features. The understanding comes with both the knowledge of the theory behind the code, and experience with the user interface and embedded code details. The code has enough features such that even the most knowledgeable and experienced user can never obtain complete knowledge of all the capabilities of COMSOL.

COMSOL should not be thought of as a computational fluid dynamics code. This is far too limiting a comparison. The basis of COMSOL is a finite-element PDE solver, and COMSOL is best thought of as a computational language and GUI system that incorporates all the elements of solving physical problems by computer simulation. That is, create the geometry, incorporate the physics, create a mesh, and finally, obtain a solution. The system is built such that at any stage along this path (geometry to solution), the user may loop back and modify one or more steps to finally arrive at a solution he is satisfied with. The COMSOL system is so powerful and diverse in application, that it is easy for a user to become entrained in his thought process, and not realize that a few simple steps will enable a much broader range of applicability.

Perhaps the most powerful feature of COMSOL is the least utilized. That is, the ability to not only examine the entire equation system being solved in detail, but to actually change the governing equations, or boundary condition definitions, or any aspect of the problem solved including all artificial dissipation mechanisms. Most users, the authors included, tend to use the equations given in the application modes, and seldom change anything. The essence of this feature is that there is nothing hidden and the user knows exactly what is solved; a feature seldom found in most commercial CFD-type codes. The real power of this feature, however, is the ability to actually modify the equation systems to yield a more consistent result with real-world (experiment, test, or operational) data. In engineering applications, this usually means the constitutive relationships such as heat transfer coefficients, pressure-loss coefficients, turbulence model equations, etc. It is fully expected that this feature will be exercised on this project since so many items are unique about the HFIR fuel plate including high heat fluxes, thin fuel plate involute design, and high level of turbulent flow given the large mass flux down the coolant channels. Fortunately, there is ample data available for comparison and validation should it become necessary to derive new constitutive relationships as the project evolves.

The COMSOL documentation and online knowledge base contain sufficient information about how to solve the larger 3D problems when memory limitations become an issue. Even with computer systems with memory as large as 64GB, memory limitations can easily become a constraint if limited to direct-solving multiphysics 3D. As more equations are used in the system being simulated, combined with more mesh points created by the assembly of the finite elements used on the geometry, the extension to 3D from 2D brings a whole entire problem into play: how can one solve such a large system of equations efficiently ?

COMSOL comes equipped with a full set of tools for performing this task using state-of-the-art, yet fully established and well-proven solvers designed for this task. Clearly, the size of the problem can eliminate direct solutions since at least one entire Jacobian matrix must fit into memory at one time for a direct solver to be used. For example, consider a problem with 10^6 degrees of freedom. This would translate to roughly 10^5 node points since we have roughly 10 variables being solved at each node point (u,v,w,p,logk,logd,T_s,T_f). The solution matrix would then contain roughly 10^{12} elements (10^6 X 10^6). Since each floating-point word in each element is 64-bit accurate, and each byte is 8-bits, we need about $8x10^{12}$ bytes or about 10^4 GB of memory just to store the Jacobian matrix ! Certainly, there are techniques to reduce this direct memory requirement such as segregation of the solution into smaller groups [(u,v,w,p), (logk,logd), and (T_s,T_f)] that can be solved separately, then iterate to convergence, or special algorithms for taking advantage of sparsely loaded matrices. Even with these special techniques,

the net result is that direct solvers will eventually not be practical for a reasonably large 3D problem. Hence, we clearly must look at alternatives.

The recommended solver for 3D Navier-Stokes (NS) equations (base equation system investigated here) provided by COMSOL is the GMRES indirect, or iterative, solver. In addition to segregating the equations into parts as mentioned earlier, the user must also choose a preconditioner. The recommended choice of a preconditioner for this type of problem class (NS) is the Geometric Multigrid (GMG) method. In addition, pre- and post-smoothers must be chosen in order for the preconditioner to work correctly. All these options have been investigated and many discussions with COMSOL tech support to understand subtle details; some of which have changed as new versions of the code have been released.

In addition to the solver settings, a recent realization that a setting in the turbulence model boundary conditions for the quantity "wall offset" had been improperly input such that previous calculations were not producing correct results. In particular, previous calculations produced little or no boundary layer variation in either velocity or temperature. This gave the mistaken impression that the turbulent diffusivity was essentially nil, hence, over-cooling of the clad temperature was falsely indicated. The default value of the wall offset is "h/2" where "h" is roughly the longest distance across a finite element. For 2D elements of near equal sides, this default value works fine. However, for 3D problems with large aspect ratios in the elements, the default must be changed or the result will be absolutely wrong!

The 3D mesh generation created here includes a boundary-layer region and requires specification of the smallest mesh spacing near the wall. One can think of this value as being identical to the wall-offset value required for specification in the turbulence model boundary conditions for both velocity and temperature. Indeed, once the wall offset is specified in this manner, a correction in the previous results was believed to have been produced but is not reported here because insufficient resources were available to check the calculation. Future work will include documentation.

It is common knowledge in modeling turbulent flow with standard k-ε and k-ω models, that the "law-of-the-wall" must be used in order produce valid results. This usually comes down to proper specification of the near-wall mesh spacing in order to produce $30<y^+<100$, which is consistent with the recommendations in the COMSOL documentation. A good practice is to first produce $y^+ \sim 10$, and then as the problem non-linear features unfold, such as pressure and temperature dependence in the fluid properties, the y^+ value will typically increase to the valid range. Thus, the problem becomes an iterative procedure, and requires manual intervention in the mesh generation process.

A first cut in this process has been completed by generating an outer-plate model of half width in both fuel and coolant regions. The purpose of producing these results is to demonstrate that a full 3D model of the fuel plate and coolant is certainly possible with COMSOL and can be computed with the computer resources available. This is a very important finding since earlier findings might suggest otherwise. No claim of accuracy or validity is made at this point since it clear there are several inputs that are not correct. When all the inputs are correct in this model, we can then be critical of the results.

The model includes constant material properties to be consistent with earlier work in this report. The default COMSOL-provided properties for water (constant atmospheric pressure, but varies in temperature) is utilized as a time-saving measure until a more accurate representation is made. A representation for a portion of the side plates is included up to an assumed adiabatic boundary. A first-cut in mesh design yielded y+ $\sim$ 10 at the steady-state solution in the wall-normal direction. Note that y+ not only depends on the mesh spacing near the wall, but also the solution outcome and the fluid properties adjacent to the wall. A significant increase in the axial-direction meshing is incorporated in the model which is a significant improvement over an earlier model.   The present axial meshing is of sufficient resolution in the axial direction of the plates such that essentially zero oscillation exists in the solution. The solution has no added artificial

dissipation beyond the default Galerkin Least Squares (GLS) used by default for the Navier-Stokes equations in COMSOL.   The model produced ~ 5×10^6 degrees of freedom and required ~ 40 GB of memory to iteratively solve the problem in ~ 10 days on 8 cpus.

Because the results from this model are preliminary, a critical assessment will not be provided herein. However, a representative temperature profile is provided below as Figure 101 for future reference. The overlay of temperature profiles is extracted from the same radial distance from the centerline of the coolant (left-hand side) to the centerline of the fuel plate (right-hand side) at several axial locations starting from the entrance to the exit of the fuel plate channel. These results are very encouraging toward an ultimate goal of an accurate fuel-plate simulation. The temperature traces show an essentially monotone, non-oscillatory behavior in the temperature in all directions without suppression due to unnecessary artificial dissipation. The turbulence model is producing a smooth variation in the boundary layer up to the point of wall interface where the sudden jump produced by the law-of-the-wall assumption is apparent.
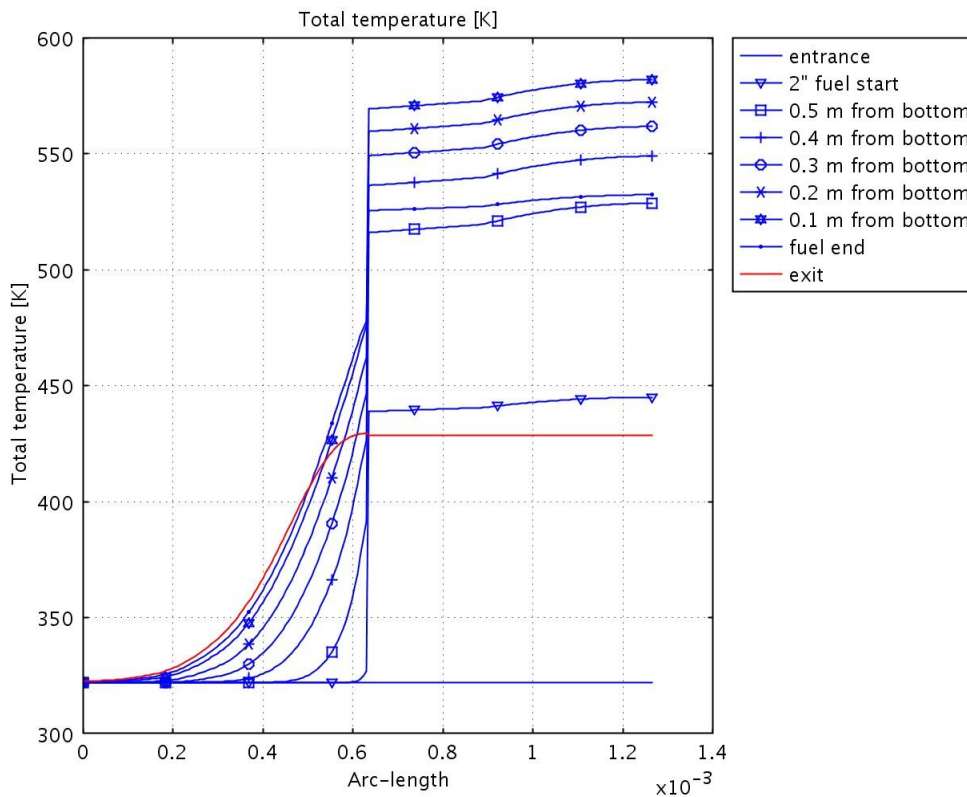
Fig. 101. Temperature profile from coolant channel centerline to fuel plate centerline

The magnitude of the wall temperature is much higher than expected which leads one to suspect that the heat transfer is not adequate to validate against known data. This is most likely caused by the choice of mesh resolution near the wall which directly affects the value of y+. COMSOL technical support advise that, "a good modeling practicing is to set the wall offset to a constant value on the order of the element size normal to the wall. This is especially important when using a stretched grid, which is most often the case in turbulent flow simulations. The logarithmic wall functions are formally valid for a range of the wall offsets in terms of viscous length scales $y^+ =$

$\Delta y \, / \, l^*$, where l^* is the viscous length scale at the wall. For accurate simulations, the range should be $30 \le y^+ \le 100$. The user should evaluate the y^+ values <u>after</u> the simulation to confirm that they are within the range. If not, remesh using a smaller (or larger if y^+ is too small as in the present analysis) wall normal element size and wall offset, and rerun the simulation. Alternatively, the user can specify y^+ in the boundary condition, but in this case the user should evaluate if the wall normal element size is the same order as y^+. If not, the user will use "too much stretching" close to the wall." We clearly have a situation which requires multiple executions in order to optimize the value of the wall offset. Therefore, any critical assessment of these results is premature until such time as all the geometry, material property, and meshing inputs are finalized. It is hoped that a future version of this or related report might include such an assessment.

7.4 Conclusions from full element simulations

In one case, the COMSOL simulated turbulent conductivity is 1-2 orders of magnitude larger in these simulations. The unnaturally large conductivity values cause the energy across the hot stripe to be artificially conducted to surrounding fluid. This error likely stems inappropriate values of the wall offset parameter in the input to the calculation. Finer nodalization is not practical when using current direct-solver solution methods. In another case, a much finer mesh was utilized to take advantage of more memory-efficient indirect iterative solvers. While the finer nodalization was solved at the expense of longer solution times, it also produced an opposite effect upon the heat transfer by not removing enough heat from the fuel-plate walls.   The choice of using the more-complex default indirect iterative solution method provided by COMSOL for 3D flow problems was determined to be beyond the scope of this research project. Future research should find an optimum range for mesh sizing such that reasonable values of both y^+ and T^+ produce acceptable heat transfer results in 3D.

8.0 SUMMARY OF CONCLUSIONS

COMSOL was able to produce accurate results for the 1-dimensional conduction and 2-dimensional conduction simulations. However, for most simulation application modes employed to model fuel plate conduction in conjunction with fluid flow, COMSOL returned cladding surface temperatures well below those expected based on legacy models. The 2-dimensional turbulent flow matched to fuel conduction simulation follows recommended nodalization refinement rules. Interestingly, while the apparent heat transfer was in excess of expected values, COMSOL was able to return credible turbulent conductivity values for the fluid.   One possible conclusion is that the legacy SSHTC of McLain is overly conservative in estimating heat transfer. The more likely conclusion however, is that the COMSOL solution is sensitive to mesh density and other model details that are in a preliminary stage at this point in the research.

The COMSOL generated solutions in its various domains are node sensitive. With the available computational resources - eight processors and 64 GB RAM - COMSOL performs well in the 2 dimensional modeling realm using the direct solver. This allowed for routine tests to compare thermal-fluid outcomes to legacy models. In order to minimize the required mesh density in the 2-dimensional models, the mesh density was highest at the near wall region and it was allowed to decrease as it moved further away from the wall. In order to achieve similar results in the 3-dimensional domain, a much larger mesh is required. A suitable mesh density for accurate 3-dimensional simulations requires significantly more resources than were chosen for this study since only direct solvers were employed by this research project.

It is important to note that COMSOL is an evolving commercial multiphysics code. As such, platform stability should be controlled following an established software quality assurance procedure when evaluating this code for use in sensitive areas such as safety analysis. A regressive testing sequence is recommended to assure that each successive version of the code is capable of either repeating old results or produces improved outcomes.

This page blank.

9.0 REFERENCE

1.   Baker, A. J., <u>The Computational Engineering Sciences</u>. The Computational Engineering Sciences. 2006.

2.   Cole, T. E., Parsley, L. F., and Thomas, W. E., "Revisions to HFIR Fuel Element Steady State Heat Transfer Analysis Code." ORNL/CF-85/68, 1986.

3.   COMSOL Digital Guide. file:///C:/COMSOL34/doc/multiphysics/wwhelp/wwhimpl/common/html/wwhelp.htm?context= multiphysics&file=ugmesh.10.8.html#605858

4.   Hatton, A. P. and Quarmby, Alan. "The Effect of Axially Varying and Unsymmetrical Boundary Conditions on Heat Transfer with Turbulent Flow Between Parallel Plates." International Journal of Heat and Mass Transfer, Vol. 6, pp. 903-914, 1963.

5.   Incropera, Frank and DeWitt, David. *Fundamentals of Heat and Mass Transfer*. John Wiley and Sons. 2002.

6.   Kármán, T. von (1939), "The Analogy between Fluid Friction and Heat Transfer," ASME Trans., vol. 61, pp. 705-710.

7.   McLain, Howard. "HFIR Fuel Element Steady State Heat Transfer Analysis Revised Version." *Oak Ridge National Laboratory.* December 1967.

8.   Morris, D. G. and Wendel, M. W. *High Flux Isotope Reactor System RELAP5 Input Model,* ORNL/TM-11647, January 1993.

9.   Ruggles, A. E., "Techniques for Consideration of Spatial Flux Perturbations due to Fuel Manufacturing Tolerances in Plate Fueled Reactors." Proceedings of NURETH 8, pp. 1823-1830, Sept. 30-October 4, 1997.

10.   Spalding, D. B. (1961), "A Single Formula for the Law of the Wall," J. Appl. Mech., vol 28, pp455-457.

11.   Thomas, W. E., Personal communication, *Bases for the Scram Setpoints, the Limiting Safety System Settings and the Safety Limits of the High Flux Isotope Reactor for Mode I 0peration at 85 MW(th)*, ORNL/RRD/INT-22, December 22, 1987.

12.   White, F., <u>Viscous Fluid Flow</u>. New York. McGraw-Hill, 2006.

13.   Wilcox, D. C., *"Turbulance Modeling for CFD,"* DCW Industries Inc., 1998.

This page blank.

APPENDIX A

MATLAB CODE FOR HEAT TRANSFER COEFFICIENT MODEL COMPARISON

```
%comparison of engineering heat transfer models in preparation for
%comparison with COMSOL outcomes based on law of the wall.
tbulk=76.7
span=0.086
gap=0.00127
kl=0.673
flux=[1.e6,2.e6,3.e6,4.e6,5.e6];
row=970.2
pr=2.16
Vel=17.
Dh=4.*span*gap/((2.*span)+(2.*gap))
mubulk=3.47e-4
rey=row*Vel*Dh/mubulk
nudb=0.023*rey^0.8*pr^0.4
hdb=(kl/Dh)*nudb
dtdb=flux./hdb
%other models have viscosity ratios, requiring twall.  BD model allows
%twall estimate to expedite comparisons
muwall=mubulk+[[(3.47e-4)-(2.67e-4)]/(76.7-104.4)].*dtdb
nust=0.027*rey^.8*pr^.4*(mubulk./muwall).^0.14
hst=(kl/Dh).*nust
dtst=flux./hst
plot(dtdb,flux,'g','LineWidth',3)
hold on
plot(dtst,flux,'LineWidth',3)
numh=0.116*[rey^.667-125]*(pr^.333)*((mubulk./muwall).^.14)
hmh=(kl/Dh).*numh
dtmh=flux./hmh
plot(dtmh,flux,'r--','LineWidth',3)
revised_numh=.0235*[rey^.8-230]*(1.8*pr^.3-.8)*((mubulk./muwall).^.14)
revised_hmh=(kl/Dh).*revised_numh
dtmh=flux./revised_hmh
xlabel('Twall-Tbulk (K)')
ylabel('Flux(W/(m^2)')
plot(dtmh,flux,'k-.','LineWidth',3)
```

This page blank.

APPENDIX B

HEAT TRANSFER COEFFICIENT COMPARISON

```
clear all

%%All material properties were found in Fundamentals of Heat and Mass
%%Transfer; by Frank Incropera and David DeWitt; Table A.6 page 924
T_in = 321.9;
T_out = 345;
T_mean = 333.45;
Q = 80700000;
v_in = 15.8;
v_out = 15.99;
v_mean = 15.895;
cp_in = 4180.76;
cp_out = 4191;
cp_mean = 4185.38;
rho_in = 988.37;
rho_out = 976.56;
rho_mean = 982.91;
mu_mean = 0.00046416;
m_dot = 836.35;
D_h = 0.0025;
k_mean = 0.65414;
A_heat = 39.84;


Re = (rho_mean*v_mean*D_h)/mu_mean;

Pr = (mu_mean*cp_mean)/k_mean;

Nu_db = 0.023*(Re^0.8)*(Pr^0.4);

Nu_revisedMH = 0.0235*(Re^0.8-230)*(1.8*Pr^0.3 - 0.8);

h_db = (k_mean*Nu_db)/D_h;

h_revisedMH = (k_mean*Nu_revisedMH)/D_h;

q = Q/A_heat;
%q=1477676;
Twall_db = q/h_db + T_mean;

Twall_revisedMH = q/h_revisedMH + T_mean;


%%%%%%%%%%%%%%%%%%%%%%%%%%%%%%%%%%%%%%%%%
%%%%%%%%%%%%%%%%%%%%%%%%%%%%%%%%%%%%%%%%%%
%%%%%%%%%%%%%%%%%%%%%%%%%%%%%%%%%%%%%%%%

f = 0.02;
g = 9.81;
```

```
L = 0.6096;
h = 0.00127;


Delta_P = rho_out*v_out^2 - rho_in*v_in^2 - rho_mean*g*L +
0.5*rho_mean*v_mean^2*f*(L/D_h);


Delta_Pform = 0.5*rho_out*v_out^2 + 0.1*rho_in*v_in^2;


Delta_Ptotal = Delta_P + Delta_Pform;


Delta_u = (rho_mean*g*v_mean*L + q*(L/h) -
0.5*rho_mean*v_mean^3*f*(L/D_h) + Delta_Ptotal*v_mean)/(rho_in*v_in) +
(v_in^2/2 - v_out^2/2);
```

HFIR SAR BEGINNING-OF-CYCLE HEU POWER DISTRIBUTION DATA AND LEU TYPICAL CHANNEL DATA

```
Inner element
DR(I,1), I = 1,7 and I = 8,M
DR is the radial increment for the node.
   0.        0.0895    0.         0.3386    0.3937    0.3937
0.3937
    0.3937    0.2362    0.         0.0794
DZ(J,1) 10 per card, except for 83 which has J = 31, N.
DZ is the axial increment for the node
 0.    2.000 0.    0.5512 0.7874 0.7874 0.7874 0.7874 0.7874
0.7874
0.7874 0.7874 0.7874 0.7874 0.7874 0.7874 0.7874 0.7874 0.7874
0.7874
0.7874 0.7874 0.7874 0.7874 0.7874 0.7874 0.7874 0.7874 0.5512 0.
Inner element relative power density.  Core power is 85MW.  You
would have to convert the numbers below to power
density in the fuel meat, which means making use of the thickness
of meat at each radial location.
0      0      0      0      0      0      0      0      0      0      0
0      0      0      0      0      0      0      0      0      0      0
0      0      0.678 1.109 1.379 1.515 1.470 1.344 1.186 0      0
0      0      0.722 0.741 0.738 0.771 0.809 0.830 0.837 0      0
0      0      0.815 0.753 0.738 0.767 0.802 0.830 0.824 0      0
0      0      0.924 0.848 0.810 0.821 0.850 0.889 0.893 0      0
0      0      1.031 0.952 0.904 0.917 0.939 0.980 0.988 0      0
0      0      1.130 1.043 0.990 1.007 1.027 1.067 1.077 0      0
0      0      1.227 1.126 1.068 1.089 1.107 1.146 1.162 0      0
0      0      1.312 1.198 1.137 1.163 1.179 1.217 1.241 0      0
0      0      1.387 1.264 1.200 1.233 1.241 1.280 1.316 0      0
0      0      1.447 1.322 1.255 1.285 1.294 1.334 1.383 0      0
0      0      1.493 1.372 1.306 1.332 1.339 1.380 1.445 0      0
0      0      1.520 1.398 1.338 1.369 1.372 1.410 1.478 0      0
0      0      1.532 1.408 1.350 1.386 1.388 1.422 1.490 0      0
0      0      1.533 1.403 1.349 1.386 1.388 1.420 1.485 0      0
0      0      1.523 1.393 1.335 1.372 1.375 1.418 1.464 0      0
0      0      1.494 1.368 1.305 1.342 1.345 1.380 1.425 0      0
0      0      1.448 1.324 1.256 1.289 1.295 1.330 1.372 0      0
0      0      1.384 1.264 1.193 1.221 1.235 1.283 1.312 0      0
0      0      1.312 1.195 1.127 1.150 1.167 1.212 1.248 0      0
0      0      1.235 1.120 1.057 1.077 1.097 1.144 1.177 0      0
0      0      1.148 1.039 .982  1.000 1.023 1.069 1.098 0      0
0      0      1.050 0.952 .903  .920  0.945 0.988 1.011 0      0
0      0      0.944 0.859 .820  .839  0.864 0.904 0.916 0      0
0      0      0.819 0.762 .735  .755  0.783 0.816 0.812 0      0
0      0      0.709 0.668 .667  .698  0.735 0.762 0.753 0      0
0      0      0.706 0.678 .680  .713  0.749 0.760 0.762 0      0
0      0      0.703 1.028 1.231 1.342 1.319 1.216 1.078 0      0
```

```
0      0      0      0      0      0      0      0      0      0      0
0      0      0      0      0      0      0      0      0      0      0
Outer element - same defintions as above.
   0.        0.0739    0.        0.3346    0.3937    0.3937
0.3937
   0.3937    0.3937    0.        0.0443
 0.    2.000 0.    0.5512 0.7874 0.7874 0.7874 0.7874 0.7874
0.7874
0.7874 0.7874 0.7874 0.7874 0.7874 0.7874 0.7874 0.7874 0.7874
0.7874
0.7874 0.7874 0.7874 0.7874 0.7874 0.7874 0.7874 0.7874 0.5512 0.
0      0      0      0      0      0      0      0      0      0      0
0      0      0      0      0      0      0      0      0      0      0
0      0      1.580 1.512 1.394 1.254 1.119 0.719 0.298 0      0
0      0      0.970 0.934 0.770 0.660 0.542 0.442 0.293 0      0
0      0      0.943 0.860 0.758 0.650 0.533 0.425 0.291 0      0
0      0      0.961 0.885 0.796 0.691 0.578 0.467 0.323 0      0
0      0      1.043 0.978 0.881 0.781 0.669 0.562 0.429 0      0
0      0      1.146 1.075 0.977 0.878 0.767 0.669 0.552 0      0
0      0      1.239 1.165 1.064 0.964 0.864 0.775 0.670 0      0
0      0      1.320 1.247 1.143 1.045 0.946 0.875 0.787 0      0
0      0      1.388 1.319 1.214 1.117 1.027 0.973 0.898 0      0
0      0      1.448 1.382 1.279 1.180 1.101 1.073 1.019 0      0
0      0      1.499 1.437 1.337 1.239 1.168 1.169 1.127 0      0
0      0      1.539 1.480 1.382 1.284 1.222 1.246 1.224 0      0
0      0      1.558 1.500 1.404 1.306 1.242 1.285 1.308 0      0
0      0      1.559 1.500 1.405 1.306 1.242 1.285 1.308 0      0
0      0      1.543 1.483 1.389 1.291 1.222 1.237 1.225 0      0
0      0      1.510 1.448 1.353 1.255 1.174 1.150 1.117 0      0
0      0      1.448 1.387 1.286 1.190 1.101 1.067 0.998 0      0
0      0      1.379 1.311 1.209 1.112 1.021 0.968 0.882 0      0
0      0      1.303 1.232 1.129 1.030 0.937 0.868 0.769 0      0
0      0      1.222 1.149 1.045 0.944 0.846 0.767 0.661 0      0
0      0      1.135 1.060 0.957 0.854 0.750 0.662 0.555 0      0
0      0      1.044 0.969 0.865 0.760 0.649 0.552 0.438 0      0
0      0      0.951 0.876 0.770 0.662 0.544 0.433 0.304 0      0
0      0      0.845 0.783 0.675 0.567 0.449 0.321 0.174 0      0
0      0      0.741 0.700 0.616 0.517 0.403 0.282 0.138 0      0
0      0      0.744 0.695 0.613 0.521 0.420 0.296 0.112 0      0
0      0      1.342 1.294 1.173 1.016 0.848 0.451 0.034 0      0
0      0      0      0      0      0      0      0      0      0      0
0      0      0      0      0      0      0      0      0      0      0
```

Following are relative power densities (local/core average) for the hot
channel in the current LEU design

```
   1.511
   1.312
   1.100
   0.946
   0.916
```

```
   0.998
   1.161
   1.355
   1.452
   1.463
   1.459
   1.349
   1.171
   1.001
   0.914
   0.966
   1.069
   1.247
   1.548


Axial layers

100     pz      25.4            $ IFE & OFE upper bound of active fuel
area - top of axial layer  1
150     pz      24.9            $ IFE & OFE upper bound of active fuel
area - top of axial layer  2
151     pz      24.4            $ IFE & OFE upper bound of active fuel
area - top of axial layer  3
153     pz      23.4            $ IFE & OFE upper bound of active fuel
area - top of axial layer  4
154     pz      22.4            $ IFE & OFE upper bound of active fuel
area - top of axial layer  5
155     pz      21.0            $ IFE & OFE upper bound of active fuel
area - top of axial layer  6
156     pz      16.8            $ IFE & OFE upper bound of active fuel
area - top of axial layer  7
157     pz      12.6            $ IFE & OFE upper bound of active fuel
area - top of axial layer  8
158     pz       4.2            $ IFE & OFE upper bound of active fuel
area - top of axial layer  9
159     pz       1.0            $ IFE & OFE upper bound of active fuel
area - top of axial layer 10
161     pz      -1.0            $ IFE & OFE upper bound of active fuel
area - top of axial layer 11
162     pz      -4.2            $ IFE & OFE upper bound of active fuel
area - top of axial layer 12
163     pz     -12.6            $ IFE & OFE upper bound of active fuel
area - top of axial layer 13
164     pz     -16.8            $ IFE & OFE upper bound of active fuel
area - top of axial layer 14
165     pz     -21.0            $ IFE & OFE upper bound of active fuel
area - top of axial layer 15
166     pz     -22.4            $ IFE & OFE upper bound of active fuel
area - top of axial layer 16
167     pz     -23.4            $ IFE & OFE upper bound of active fuel
area - top of axial layer 17
168     pz     -24.4            $ IFE & OFE upper bound of active fuel
area - top of axial layer 18
169     pz     -24.9            $ IFE & OFE upper bound of active fuel
area - top of axial layer 19

Bottom of core is at -25.4 cm
```

INTERNAL DISTRIBUTION

1.	S. E. Burnette	11.	R. W. Hobbs
2.	J. J. Carbajo	12.	C. R. Hyman
3.	D. H. Cook	13.	L. J. Ott
4.	R. A. Crone	14-16.	R. T. Primm III
5-7.	J. D. Freels	17.	K. A. Smith
8.	J. C. Gehin	18.	G. L. Yoder
9.	F. P. Griffin	19.	RRD-DCC-RC
10.	G. J. Hirtz	20	Laboratory Records – OSTI

EXTERNAL DISTRIBUTION

21. Lee Tschape, Department of Nuclear Engineering 315 Pasqua Engineering Building Knoxville, TN 37996-2300 (*ltschaepe@gmail.com*).
22. Dr. H. D. Gougar, Manager, Fission and Fusion Systems, Idaho National Laboratory, P. O. Box 1625, MS 3860, Idaho Falls, ID 83415-3860.
23. D. Kutikkad, Ph.D., Assistant Reactor Manager-Physics, University of Missouri Research Reactor Facility, Columbia, MO 65211.
24. Dr. G. I. Maldonado, Associate Professor, University of Tennessee, Department of Nuclear Engineering, 311 Pasqua Engineering Building, Knoxville, TN 37996-2300.
25. T. Newton, MIT Nuclear Reactor Laboratory, 138 Albany St., Cambridge, MA 02139.
26. R. D. Rothrock, 705 Cordova Lane, Lenoir City, TN 37771.
27. R. E. Williams, NIST Center for Neutron Research, 100 Bureau Drive, Stop 8560, Gaithersburg, MD 20899.
28. Dr. Art Ruggles, Department of Nuclear Engineering 315 Pasqua Engineering Building Knoxville, TN 37996-2300 (*aruggles@utk.edu*).
29. Dr. H. L Dodds, Department of Nuclear Engineering 315 Pasqua Engineering Building Knoxville, TN 37996-2300 (*hldodds@utk.edu*).
30. A. Adams, U.S. Nuclear Regulatory Commission, One White Flint North, 11555 Rockville Pike, Rockville, Maryland 20852-2738 (*axa@nrc.gov*).
31. G. S. Chang, Idaho National Laboratory, P.O. Box 1625, Idaho Falls, ID 83415-3885 (*gray.chang@inl.gov*).
32. D. Diamond, Brookhaven National Laboratory, P.O. Box 5000, Upton, NY 11973-5000 (*diamond@bnl.gov*).
33. J. Matos, Argonne National Laboratory, 9700 S. Cass Avenue, Argonne, IL 60439 (*jim.matos@anl.gov*).
34. A. J. Baker, PhD, PE, Professor, Engineering Science Graduate Program, Director, UT CFD Laboratory, http://cfdlab.utk.edu, 316A Perkins Hall, University of Tennessee, Knoxville TN 37996 2030 USA (*ajbaker@utk.edu*).
35. Ed Fontes, Ph.D., VP of Applications, COMSOL AB, Tegnergatan 23, SE-111 40, Stockholm, Sweden (*ed@comsol.com*).